Thesis for the Degree of Doctor

# Measurement of $\Xi_c^0$ Semileptonic Decays


by

Yeon Sei Chung

Department of Physics

Graduate School

Korea University


December, 1998

**Abstract**

We present experimental results on the measurement of semileptonic decays of the neutral charmed baryon $\Xi_c^0$. We have utilized the data collected by the photoproduction fixed target experiment E687 at Fermilab during 1990 and 1991 run period.

We measure the branching ratios of $\Xi_c^0$ semileptonic decay modes relative to the mode $\Xi_c^0 \longrightarrow \Xi^- \pi^+$. Reconstruction is made both in the electron and muon modes of the $\Xi_c^0$ semileptonic decays.

We have determined the $\Xi_c^0$ branching ratios to be:

$$\frac{\Gamma(\Xi_c^0 \longrightarrow \Xi^- \mu^+ X)}{\Gamma(\Xi_c^0 \longrightarrow \Xi^- \pi^+)} = 4.0 \pm 1.9(stat.) \pm 0.6(syst.)$$

$$\frac{\Gamma(\Xi_c^0 \longrightarrow \Xi^- e^+ X)}{\Gamma(\Xi_c^0 \longrightarrow \Xi^- \pi^+)} = 2.7 \pm 2.1(stat.) \pm 0.9(syst.)$$

$$\frac{\Gamma(\Xi_c^0 \longrightarrow \Xi^- l^+ X)}{\Gamma(\Xi_c^0 \longrightarrow \Xi^- \pi^+)} = 3.5 \pm 1.5(stat.) \pm 0.6(syst.)$$

Our results are consistent within errors with the previous measurements reported by the ARGUS collaboration and the CLEO collaboration.

# Contents

# List of Figures

# List of Tables

# Chapter 1

# Introduction

High energy physics deals with the study of the fundamental particles and the nature of interactions among them. The Standard Model is consistent with observations in high energy physics so far although we are not certain yet it is the ultimate theory of particle phenomena. In the Standard Model, the fundamental particles are organized in six types of quarks and six leptons, and particle interactions, strong, electromagnetic, and weak are explained by exchange of gauge bosons.

Although there are increasingly more results revealed on hadronic decays of charmed baryons, little is known experimentally of their semileptonic decays. If semileptonic decays proceed only via a spectator process, the semileptonic rates of the charmed baryons should be comparable to the charmed mesons. Likewise, the semileptonic rates of different charmed mesons should be comparable. It is seen experimentally that the semileptonic rates of the $D^0$ and $D^+$ are the same within errors [1]. Therefore, it is interesting to examine whether or not this is true for the charmed baryons. This would not be true if interference effects are important for one charmed baryon and not for another. The semileptonic branching ratios for the shorter lived charmed baryons should be smaller due to the enhanced hadronic decay rates by the large W-exchange processes as evidenced by their short lifetimes.

Compared to hadronic decays, the reconstruction of semileptonic decays is further complicated by the fact that the neutrino can not be observed and a fully reconstructed mass plot can not be made. This means that a thorough understanding of the background is crucial in any analysis of semileptonic decays. One can also be careful in limiting the background contribution in a semileptonic analysis. For the long lived $D^+$, one can reduce background by exploiting a relatively long lifetime. Likewise, one can reconstruct a particle resonance, such as the $K^{*0}(K^-\pi^+)$ for $D^+ \longrightarrow K^{*0}l^+\nu$, or the $D^{*+}(D^0\pi^+)$ to tag the $D^0$. For charm baryons, however, the difficulties of reconstructing a signal with a short lifetime are coupled with small statistics.

In the Fermilab E687 experiment, charmed particles are produced using the world's highest energy photon beam impinging on a beryllium target. It results in photon-nucleon collisions via the photon-gluon fusion process which can be calculated using perturbative Quantum Chromo-Dynamics (QCD) to the next-to-leading order in $\alpha_s$ [2, 3].

In this analysis we describe the analysis of the electron and muon modes of $\Xi_c^0$ semileptonic decays. This analysis was performed with data collected by the Fermilab photoproduction experiment E687 during the years 1990 to 1991.

In Chapter 2, the basic features of charmed hadrons with the emphasis on the charmed baryons will be discussed. In Chapter 3, we will explain how we have generated the photon beam, how we collect the data, and the E687 experimental apparatus. In Chapter 4, the methods of data reconstruction and reduction will be discussed. Data analysis tools and the Monte Carlo simulation will be described in Chapter 5. The branching ratio measurements of the $\Xi_c^0$ semileptonic decays will be presented in Chapter 6. In Chapter 7, we will discuss possible systematic biases in the branching ratio measurement. The results and conclusion will follow in Chapter 8.

# Chapter 2

# Charmed Hadrons

## 2.1 Overviews

It is widely accepted that the matter is built from two types of fundamental fermions, leptons and quarks. Leptons carry integral electric charges, 0 or $\pm 1$, and they are grouped into three families based on the conserved lepton quantum number. Neutral leptons are called neutrinos and have very small rest mass if it is not zero. Quarks carry the fractional electric charges of $\pm\frac{1}{3}$ or $\pm\frac{2}{3}$ of the electronic charge, and they are also grouped into three generations. Leptons exist as free particles whereas quarks as constituents of hadrons only.

The existence of three quark flavors($u$, $d$, and $s$) was first proposed in 1964 by Gell-Mann [5] and Zweig [6], independently. The existence of a fourth (charm) quark was suggested by Bjorken and Glashow [7] in 1964 to make the situation between quarks and leptons symmetrical. The absence of strangeness-changing neutral weak currents($Z^0$) incorporating the $c$(charm) quark was explained with the GIM(Glashow, Illiopoulos and Maiani) model [8] in 1970. In 1974, Gaillard, Lee and Rosner [9] predicted the SU(4) spectroscopy and decay properties of hadrons containing the charm quark.

The existence of the charm quark was strongly suggested by the discovery in November 1974 of the $J/\psi$ as a narrow resonance at 3.1 GeV/$c^2$ [10, 11]. The $J/\psi$ was interpreted as a bound state of the charm and anti-charm($c\bar{c}$) pair. Subsequently, the open charm particles, such as $D^0, D^+$, and $\Lambda_c^+$ have been experimentally found and the existence of the charm quark is well established.

The discovery in 1977 [12] of the $\Upsilon$ as a $b\bar{b}$ bound state was the first indication of the existence of a fifth quark, the $b$(beauty or bottom) quark with a mass $m_b \approx$ 5 GeV/$c^2$ . Recently the discovery of a sixth quark, the $t$(top) quark with a mass $m_t \approx$ 174 GeV/$c^2$ [18] was reported by both CDF [13] and D0 [14] collaborations at Fermilab.

All six quarks predicted by the Standard Model have been established experimentally. Only two types of quark combinations, meson and baryon have been seen by experiments. Mesons consist of quark anti-quark pair and baryons of three quarks.

The properties of leptons and quarks are summarized in Table 2.1.

Table 2.1: Quark and Lepton Properties.

| Quarks | | Leptons | |
|---|---|---|---|
| Flavor | Charge | Flavor | Charge |
| $u$ $c$ $t$ | +2/3 | $\nu_e$ $\nu_\mu$ $\nu_\tau$ | 0 |
| $d$ $s$ $b$ | -1/3 | $e^-$ $\mu^-$ $\tau^-$ | -1 |

## 2.2 Photoproduction of Charmed Hadrons

The charm quark can be produced by several types of processes, high energy $e^+e^-$ annihilation, photon-hadron scattering, lepton-hadron collision, or hadron-hadron collision. Among these processes, the photon-hadron scattering is chosen by E687 for production of very clean, high statistics sample of mesons and baryons containing one charm quark.

The $e^+e^-$ interaction have proven to be a reliable and most clean way of producing charmed particles, but the absolute production rates are a few orders of magnitude lower compared to other photoproduction processes due to much lower cross section and luminosity.

The photoproduced charm cross section is roughly 1% of the total photon-hadronic cross section, which is about 5 times higher than in charm hadroproduction. The average multiplicity of hadronic particles produced in photon-hadron interactions is smaller than the average multiplicity of hadronic particles produced in hadron-hadron interactions. Typically, a Feynman diagram of the hadron-hadron interaction has 2 sources of fragmentation rather than just one. The lower multiplicity in photon-hadron interactions makes reconstruction easier and cleaner than for hadron-hadron interactions. Thereafter we have chosen photon beam rather than hadron beam mainly to suppress background.

The main drawback of the photon beam is the large $e^+e^-$ production rate relative to the hadronic interaction rate. For a beryllium target the $e^+e^-$ rate is 500 times larger than the total hadronic cross section. This implies that the experiment must resort to low Z target material. Although there may appear to be large background, unwanted events can be rejected with a dedicated trigger. Another disadvantage of a photon beam experiment is the beam flux limitation and the difficulty in collimating the beam.

The possibility of the charm photoproduction was first suggested by Carlson [15] and further developed by Gaillard [9] based on the vector meson dominance model [16] and the naive quark model. In the late 1970's, the perturbative QCD approach to charm photoproduction was made. The charm photoproduction is well described by the Photon-Gluon Fusion(PGF) [17] process. Theoretical calculations are carried out for leading order and the next-leading-order process, along with contributions

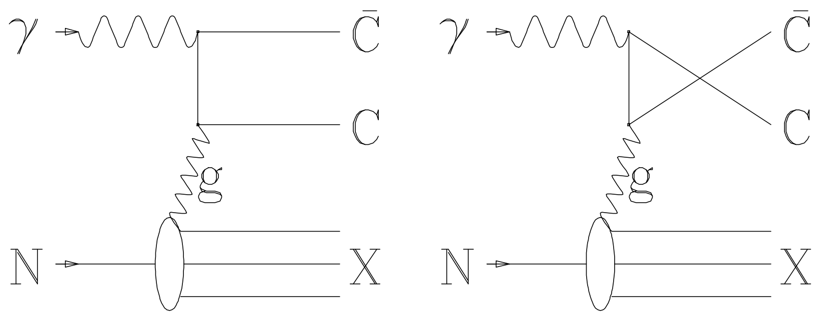


Figure 2.1: The lowest order photon-gluon fusion diagrams.

where the photon dissociates into hadronic components before interacting. The two lowest order diagrams are presented in Figure 2.1. In this model, a $c\bar{c}$ pair is produced from the interaction of a photon with a gluon from a target nucleon.

The PGF model predicts total charm cross section to rise gradually at high energies. The cross section measurements from various fixed target experiments are shown in Figure 2.2 along with the PGF predictions for different choices of the charm quark mass, $m_c$.

Virtually all of the photon energy is transferred to the $c\bar{c}$ pair and the charmed particles are boosted forward due to a large Lorentz factor, thereby reducing the aperture of the spectrometer needed to detect the decay fragments of the charmed particles. The large Lorentz factor allows the direct observation of the charmed particle lifetimes and discrimination of the charm signals from backgrounds by using the significance of separation between charm production and decay vertices.

## 2.3 Charmed Baryons

The ground-state charmed baryons are classified usually members of the SU(4) 20-plets as depicted in Figure 2.3. The $J^P = \frac{1}{2}^+$ ground state baryons comprise the SU(4) 20-plet, and $J^P = \frac{3}{2}^+$ ground state baryons the SU(4) 20-plet. All the particles

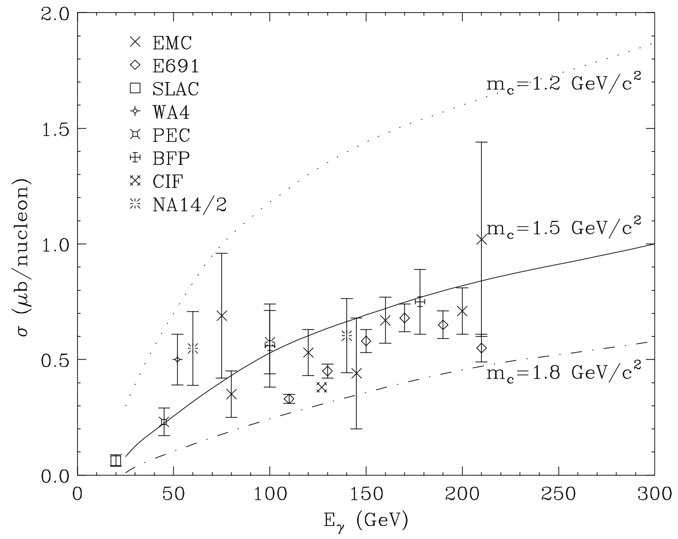


Figure 2.2: Total charm photoproduction cross-section measurements vs photon energies.

classified in a given SU(4) multiplet have the same spin and parity. Since the SU(4) flavor symmetry is badly broken by a mass difference of greater than 1 GeV/$c^2$ , the diagrams in Figure 2.3 are the simplest way to visualize what kind of charmed baryons might exist. The only charmed baryons which have been experimentally observed are those which contain one charm quark and thus belong to the second level of SU(4) multiplet. The experimental values [21] of the observed charmed baryons are listed in Table 2.2. In the table, $[ab]$ and $\{ab\}$ denote antisymmetric and symmetric flavor index combinations, respectively.

The $J^P = \frac{3}{2}^+$ charmed baryons are predicted to be massive enough to decay into $J^P = \frac{1}{2}^+$ charmed baryons by emitting one pion. Rather limited experimental information [26, 27] on the $J^P = \frac{3}{2}^+$ charmed baryons is currently available.

The remaining masses of charmed baryons in Figure 2.3 -(a) and 2.3 -(b) are theoretically calculated [22, 23] based on a central two-body potential supplemented

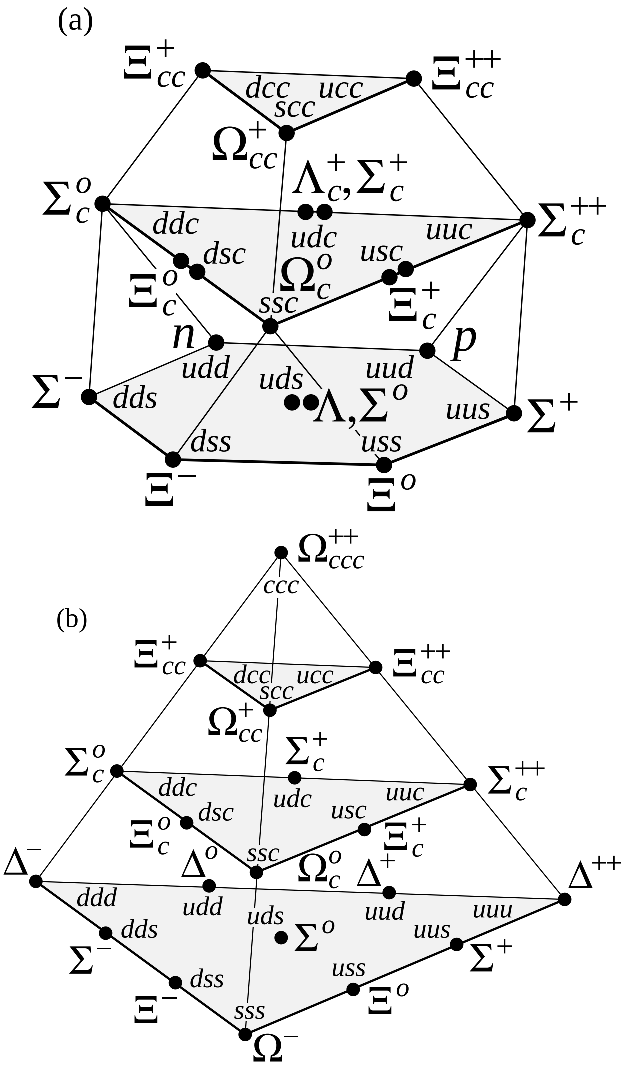


Figure 2.3: SU(4) multiplets of baryons made of $u,\ d,\ s$, and $c$ quarks: (a) $J^P = \frac{1}{2}^+$ 20-plet with an SU(3) octet on the lowest level; (b) $J^P = \frac{3}{2}^+$ 20-plet with an SU(3) decuplet on the lowest level.

Table 2.2: Properties of the experimentally observed charm baryons.

| Notation | Quark content | Mass(MeV/c$^2$) |
|---|---|---|
| $\Lambda_c^+$ | $c[ud]$ | 2284.9±0.6 |
| $\Xi_c^+$ | $c[su]$ | 2465.6±1.4 |
| $\Xi_c^0$ | $c[sd]$ | 2470.3±1.8 |
| $\Sigma_c^{++}$ | $cuu$ | 2452.9±0.6 |
| $\Sigma_c^+$ | $c\{ud\}$ | 2453.5±0.9 |
| $\Sigma_c^0$ | $cdd$ | 2452.1±0.7 |
| $\Omega_c^0$ | $css$ | 2704.0±4.0 |

by the spin-spin interaction

$$H_{ss} = \sum_{i<j} \frac{16\pi\alpha_s}{9m_i m_j} s_i s_j \delta^3(r_{ij}) \tag{2.1}$$

where one has just added two-body potentials between quarks $i(j)$ with masses $m_i(m_j)$ and spins $s_i(s_j)$ separated by the distance $r_{ij}$. It results from the Breit-Fermi reduction of the one-gluon exchange interaction. Many authors have emphasized the fact that the hyperfine splitting resulting from Equation 2.1 is crucial to the understanding of the mass-breaking pattern of both charmed and charmless hadrons [24, 25]. As long as the spin-spin interaction term is taken into account a variety of models with differing degrees of sophistication reproduce basically the similar pattern of charm baryon masses.

None of the doubly and triply charmed baryons have been observed yet. All of them are expected to decay via the weak interaction [28].

### 2.3.1 Weak Decay of Charmed Hadrons

Singly charmed particles decay via the weak interaction. The strong or electromagnetic decay of charmed particles can only proceed to ground state charmed hadrons if charm quantum number is conserved. The Feynman diagrams for the decay processes of the charmed hadrons: the spectator model (W-emission), W-exchange, and W-annihilation are shown in Figure 2.4.

The spectator diagram is believed to play a dominant role in most charmed particle decays. In this model, a charm quark decays into a lighter quark by emitting a $W^+$ boson. The remaining constituent quarks of the hadron are assumed to be spectators and do not participate the process at all.

From the spectator model and the universality of the weak interaction, we may naively estimate the charm quark lifetime from the muon lifetime:

$$\tau_c \simeq \frac{1}{5}\,\tau_\mu\,(\frac{m_\mu}{m_c})^5$$

where $\tau_\mu$ and $m_\mu$ are the lifetime and mass of the muon, $m_c$ the charm quark mass. The factor of 1/5 accounts for the two leptons (electron and muon) and three quark colors that the charm quark can decay into. This model roughly estimates charm hadron lifetimes of the order of $10^{-12}$ seconds. Since the color degree of freedom of the coupling quarks in the internal spectator diagram must match, the internal W-emission decay rate is suppressed in the decay of charmed mesons.

Although the spectator model provides a rough estimation of the charmed hadron lifetime, there are difference among measurements of various charmed hadrons. We need the W-exchange and W-annihilation processes to explain the difference. The two processes contribute about 20% to the total decay width. In the case of charmed mesons, the decay rate for both W-exchange and W-annihilation are helicity-suppressed.

In the case of charmed baryons, the W-exchange process is neither helicity nor color suppressed by the presence of the additional light quark. The W-exchange

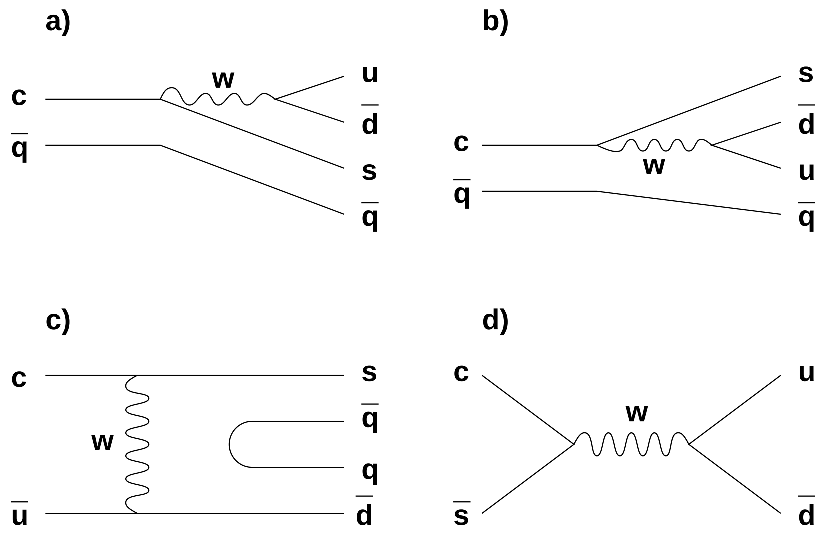


Figure 2.4: Quark level diagrams for hadronic charmed meson decays: a) external W-emission b) internal W-emission c) W-exchange d) W-annihilation.

and the internal spectator mechanisms may contribute significantly to the total charmed baryon decay rate. We can also expect the contribution of the constructive(or destructive) interference between the $s(d)$ quark from the charm decay and the spectator $s(d)$ quark in the charmed baryon. A dramatic interference contribution is predicted in the $\Xi_c^0$ and $\Omega_c^0$ decays and could be confirmed experimentally [29].

### 2.3.2 Semileptonic Decay of $\Xi_c^0$

The lepton neutrino part of the matrix element is well understood, the Cabibbo-Kobayash-Maskawa (CKM) matrix element [4] is well constrained by unitarity. Therefore we are able to measure form factors, hadronic structure, and higher order QCD effects with semileptonic decays. The leading order diagram which contributes to the semileptonic decay of the charmed baryon is the spectator diagram. The spectator diagram of $\Xi_c^0 \longrightarrow \Xi^- l^+ \nu$ decay is shown in Figure 2.5.

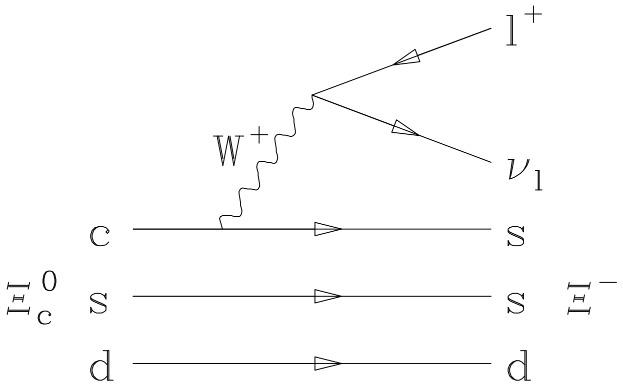


Figure 2.5: The spectator diagram for the decay of $\Xi_c^0 \longrightarrow \Xi^- l^+ \nu$.

In the spectator model, the *charm* quark decays weakly into the *strange* quark by emitting of a $W^+$ boson. Then, the virtual $W$ boson materializes into a lepton-neutrino pair and the spectator quarks($s$ and $d$) do not participate decay process.

Although the spectator model provides a reasonable description of various semileptonic decays, the discrepancies between experiment and theory as well as among experiments are known to be still large.

For the process of $\Xi_c^0 \longrightarrow \Xi^- l^+ \nu$, the decay rate is given by

$$d\Gamma(\Xi_c^0 \longrightarrow \Xi^- l^+ \nu) = \frac{1}{2M} \mid A(\Xi_c^0 \longrightarrow \Xi^- l^+ \nu) \mid^2 d\Pi_3, \tag{2.2}$$

where the Lorentz invariant phase space of the final states is given by

$$d\Pi_3 = (2\pi)^4 \delta^{(4)}(P - k - p - p^{'}) \prod_f \frac{d^3 k_f}{(2\pi)^3 2E_f}, \tag{2.3}$$

and the transition amplitude can be written as

$$A(\Xi_c^0 \longrightarrow \Xi^- l^+ \nu) = \frac{G_F}{\sqrt{2}} V_{cs} L^\mu H_\mu^{(s^{'} s)} \tag{2.4}$$

with $V_{cs}$ being the CKM matrix element appropriate for the $c \rightarrow s$ transition and the integral is over all final-state momenta. The $s^{'}$ and $s$ are spin components, the parent has four momenta $P$, the daughter $k$, the lepton $p$, and the neutrino $p^{'}$. The virtual $W^{+}$ carries four-momentum $q = p + p^{'}$. The spin-quantization axes for the parent and daughter baryons are not necessarily the same.

The lepton and hadronic currents are given by

$$L^{\mu} = \overline{u}_{l}\gamma^{\mu}(1-\gamma_5)v_{\nu},$$

$$H^{(s^{'}s)\mu} = < k, s^{'} \mid J^{\mu}_{had}(0) \mid P, s > .$$

The hadronic current can be constructed from Lorentz invariant form factors and the four-vectors of the problem. Expressing $J^{\mu}_{had} = V^{\mu} - A^{\mu}$, we define

$$\begin{aligned} < k \mid V^{\mu}(0) \mid P > &= \overline{u}_m[g(q^2)\gamma^{\mu} + g_{+}(q^2)(P+K)^{\mu} \\ &+ g_{-}(q^2)(P-k)^{\mu}]u_M, \\ < k \mid A^{\mu}(0) \mid P > &= \overline{u}_m[a(q^2)\gamma^{\mu}q\gamma_5 + a_{+}(q^2)(P+K)^{\mu}\gamma_5 \\ &+ a_{-}(q^2)(P-k)^{\mu}\gamma_5]u_M, \end{aligned} \tag{2.5}$$

where $q^2 = (P-k)^2$ and $u_M(u_m)$ is the spinor associated with the parent(daughter) baryon and spin labels have been suppressed.

## 2.4 The Experimental Status

Previous measurements on semileptonic decays of the $\Xi_c^0$ come from the ARGUS [30] and CLEO [31] experiments. ARGUS has analyzed the inclusive semileptonic decays, $\frac{\Gamma(\Xi_c^0 \longrightarrow \Xi^- l^+ X)}{\Gamma(\Xi_c^0 \longrightarrow \Xi^- \pi^+)} = 0.96 \pm 0.43 \pm 0.18$ with $18.1 \pm 5.9$ events ($12.6 \pm 4.9$

events for the electron mode, 5.5 $\pm$ 3.3 events for the muon mode). CLEO has investigated the exclusive decay, $\frac{\Gamma(\Xi_c^0 \longrightarrow \Xi^- e^+ \nu)}{\Gamma(\Xi_c^0 \longrightarrow \Xi^- \pi^+)} = 3.1 \pm 1.0^{+0.3}_{-0.5}$ with 54 $\pm$ 10 events. Although the errors are large there is still more than 1.8 $\sigma$ discrepancy between the two measurements.

# Chapter 3

# The E687 Apparatus

The E687 experiment at Fermilab was designed for investigating of the high energy photoproduction and decay of particles containing a charm quark with the high energy photons bombarded on a fixed target. The charmed particles are produced during the interactions of high energy photons with matter.

In this chapter, the apparatus described consists of: the part of the beamline in which we produce high energy photons from the high energy protons delivered by the Fermilab Tevatron, and the components of the spectrometer used to detect the particles produced in the E687 experimental target. More detailed descriptions will be given for those detector components used in the analyses presented in this thesis. A detailed description of the E687 spectrometer may be found elsewhere [36].

## 3.1 Beam Line

In the E687 experiment, high intensity and high energy photon beam is generated by complicated processes. It begins with the protons with energy 800 GeV delivered by the Fermilab Tevatron.

### 3.1.1 The Proton Beam

The proton source of Fermilab Tevatron is derived from hydrogen ions. Ionized hydrogen is accelerated to 750 keV with a Cockcroft-Walton voltage multiplier. These hydrogen ions are allowed to pass through a carbon foil where the additional electrons are stripped away from the ions, leaving the protons. Then they are sent into linear accelerator where the proton energy is raised to 400 MeV.

The protons are then sent to the booster ring, a rapid cycling synchrotron of 150 $m$ in diameter which accelerates protons up to 8 GeV. From the booster, the protons are fed into the Fermilab main ring, a larger proton synchrotron which uses conventional iron-core copper coiled magnets. At this stage, the proton beam is increased to an energy of 150 GeV. These protons are finally injected into the super-conducting synchrotron (called the Tevatron) which consists of a thousand super-conducting magnets, and accelerated to its final energy of 800 GeV. The intensity of the proton beam is about $2 \times 10^{13}$ protons per 23 second spill.

The Tevatron proton beam is extracted by a deflecting magnet and it is utilized in the production of three different secondary beams of particles; protons, mesons, and neutrinos. The E687 experiment is located at the end of proton beamline as shown in Figure 3.1. Before reaching the experiment, the proton beam is converted into a photon beam in the wideband photon beamline.

### 3.1.2 The Photon Beam

The photon beam is produced by impinging 800 GeV proton beam from the Tevatron on a 3.4 $m$ long liquid deuterium target (primary production) which corresponds to one proton interaction length. In the target, neutral pions, along with charged and neutral particles are created. The charged particles are swept away from the beam direction by sweeping magnets located immediately in the downstream of the target and the neutral particles, including the photons from the decay of the neutral pions, pass through a small hole in the dump and impact on a lead converter. It

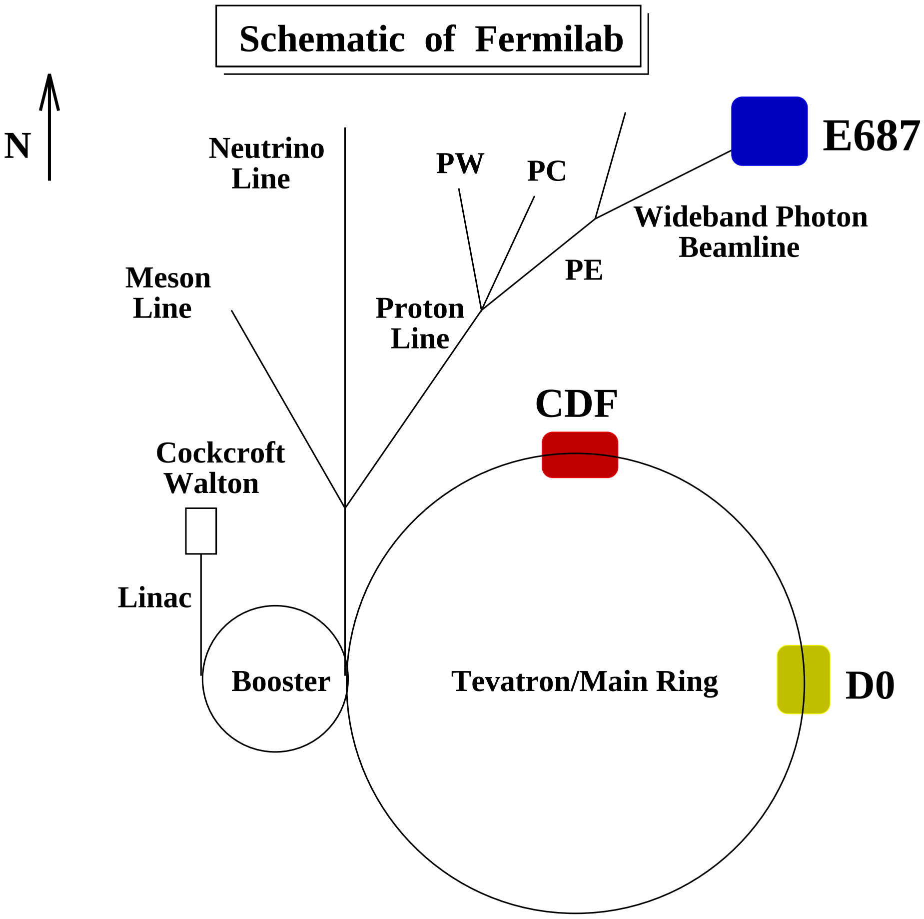


Figure 3.1: Schematic drawing of Fermilab.

has a thickness of 0.6 radiation length and produces electron-positron pairs. In 1991 another sweeping magnet was installed between the neutral hole and the lead converter.

Electrons are bent away from the beam direction and then captured by a conventional beam transport consisting of dipole magnets and quadruples. The positrons are also bent away and sent to a beam dump. The remaining neutral hadrons, neutrons and $K_L^0$'s, along with unconverted photons, travel straight ahead undeflected and are absorbed in a neutral dump.

The beam transport optics are designed for selection of electrons with nominal momentum of 350 GeV/$c$. For a high energy photon flux, electrons in a momentum range $\pm 13\%$ around the nominal setup are collected in the transport. At this point, the electron momentum is tagged with a system of magnets and silicon microstrip detector. This tagging procedure is described in the following section. At the end of the momentum tagging, the electron beam, composed of $\sim 10^8$ electrons/spill is realigned and refocused along the original zero degree direction.

The electron beam then passes through a thin lead foil, a radiator of 0.27 radiation length to produce photons by bremsstrahlung. The electron is then deflected off to the side by dipole magnets, electron sweepers, and into an electron dump while the photon passes straight ahead to the experimental target. The steps are shown in Figure 3.2.

The final photon beam has very little hadron contamination, about 1 hadron for every $10^5$ photons. Taking into account the interaction cross section, the number of events produced by hadrons interacting in the experimental target is $\sim 1\%$ of the photoproduced events. The beam properties are summarized in Table 3.1.

### 3.1.3 Photon Energy Measurement

A system of three detectors is installed in the E687 beamline not only to measure the energy of photon on an event–by–event basis, but also to require a minimum acceptable photon energy as part of the second–level trigger. The energy of the interacting photon is determined by measuring the electron momentum before and after the radiator, and measuring the energy of any non-interacting photons which are created by multiple bremsstrahlung. The tagging system consists of three independent detectors: the silicon microstrip tagging system, the Recoil Electron Shower Hodoscope detector (RESH), and the Beam Gamma Monitor (BGM) [38].

The silicon microstrip tagging system consists of five large area silicon microstrip planes installed around the final two dipole magnets of the electron beam transport

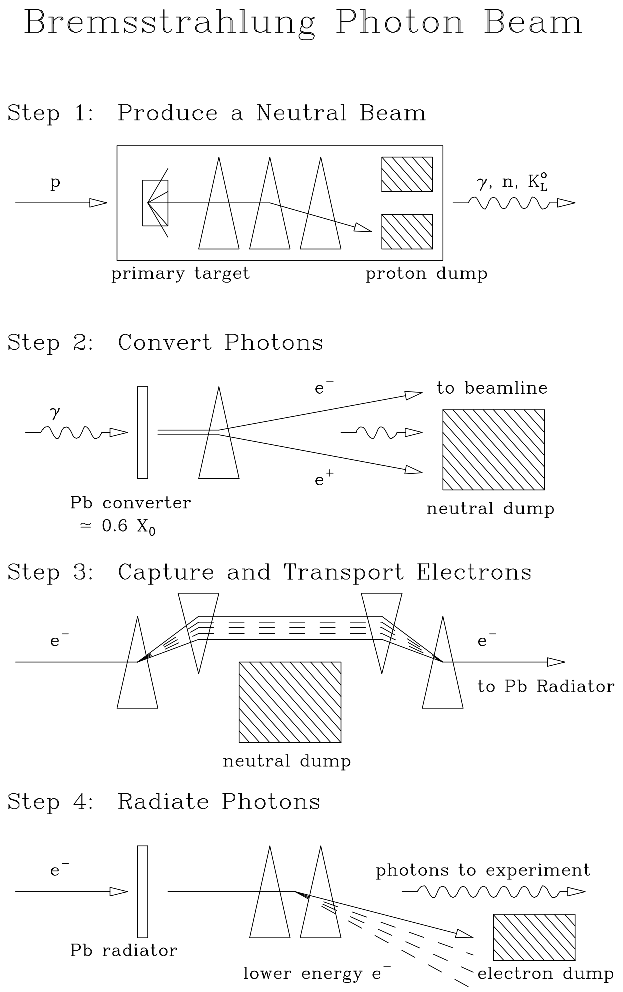


Figure 3.2: Schematic drawing of the steps used to produce the E687 photon beam from the Tevatron proton beam.

Table 3.1: Wide band beam properties

| Property | Value |
|---|---|
| Horizontal spot size at production target | $\delta x = \pm 1$ mm |
| Vertical spot size at production target | $\delta y = \pm 1$ mm |
| Geometric horizontal angle accepted | $\delta\theta_x = \pm 1.0$ mrad |
| Geometric vertical angle accepted | $\delta\theta_y = \pm 0.75$ mrad |
| Geometric solid angle accepted | $\Delta\Omega = 6.0$ $\mu$sr |
| Maximum momentum bite | $\Delta$p/p $\approx \pm 15\%$ |
| Effective acceptance | $\Delta\Omega \times \Delta$p/p $\approx 96$ $\mu$sr% |
| Horizontal spot at experimental target | $\delta x = \pm 1.25$ cm |
| Vertical spot at experimental target | $\delta y = \pm 0.75$ cm |
| Horizontal divergence at experimental target | $\delta\theta_x = \pm 0.6$ mrad |
| Vertical divergence at experimental target | $\delta\theta_y = \pm 0.5$ mrad |

system. Two planes are located in the upstream of the dipole magnets, one plane is between the magnets, and two planes are in the downstream. Each 7.7 cm $\times$ 5.7 cm silicon microstrip plane is composed of 256 silicon strips of 300 $\mu$m pitch for a total of 1,280 channels. The microstrip system accurately measures the deflection angle of the electron as it traverses the dipole magnets and provides a 2.2% momentum resolution.

The RESH was located downstream of the final lead radiator and measures the electron momentum after it has emitted bremsstrahlung photons. The RESH consists of 10 hodoscope counters, which are either lead–lucite or lead–acrylic scintillator shower counters of about 24 radiation length in depth, arranged perpendicular to the photon beam direction. A phototube is used to collect the Čerenkov light created in the lucite when an electron develops an electromagnetic shower. The struck counter determines the bent angle of the electron and thus the momentum. The BGM is a segmented lead–lucite calorimeter, located between the inner electromagnetic calorimeter and the hadron calorimeter. The BGM has 24 radiation lengths in depth and is designed to measure the electromagnetic shower energies resulting from multiple bremsstrahlung photons created in the upstream lead radiator. During the second run period in 1991, the BGM was replaced by the beam calorimeter (BCAL) which was provided by the downstream experiment E683.

With the energies recorded in each detector, the energy of interacting photon can be calculated from

$$E_\gamma = E_{e^-}^{\rm inc} - E_{e^-}^{\rm RESH} - \sum E_\gamma^{\rm BGM}$$

where

- $E_{e^-}^{\rm inc}$ is the incident electron energy measured by the silicon microstrip tagging system,
- $E_{e^-}^{\rm RESH}$ is the recoil electron energy after emitting bremsstrahlung photons in the radiator, which is determined by the RESH,

- $\sum E_{\gamma}^{\text{BGM}}$ is the total energy deposited in the BGM by non-interacting photons.

Figure 3.3 shows the energy spectra measured in each detector. The mean tagged photon energy was about 210 GeV and approximately 60% of the photon triggers had an acceptable energy tag due to the limited acceptance of the RESH counter.

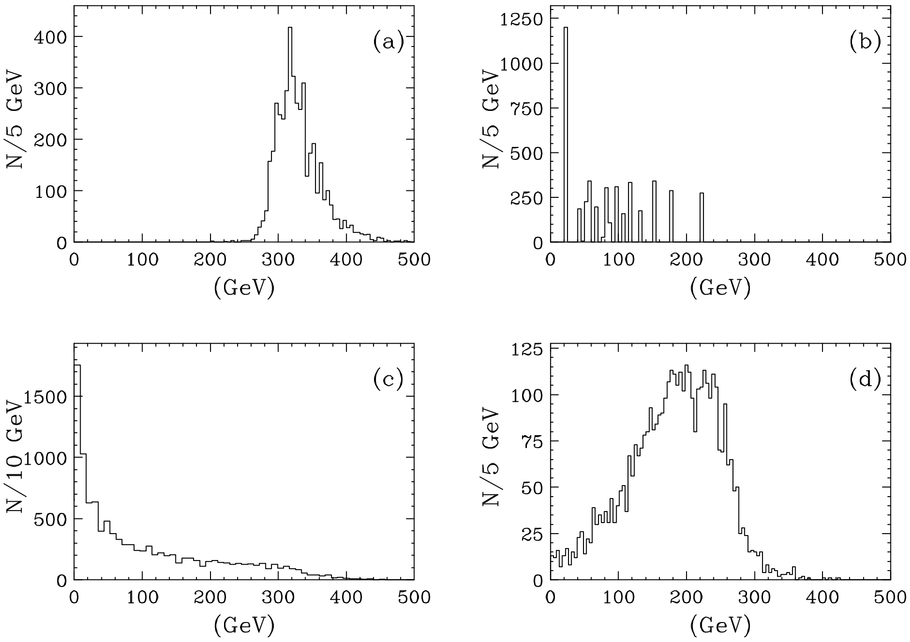


Figure 3.3: Typical energy spectra: (a) the incident electron energy distribution, (b) the energy distribution of recoil electron, (c) the energy spectrum of bremsstrahlung photons, and (d) the energy spectrum of interacting photon.

### 3.1.4 Target

The target is composed of beryllium segments, each 2.54 cm $\times$ 2.54 cm in size and 0.4 cm in thickness. Two slightly different target configurations have been used during the run. Approximately 37% of the data was taken with a nine–segment

Table 3.2: Target configurations for the 1990 and 1991 runs.

| | Configuration–I | Configuration–II |
|---|---|---|
| No. of segments | 9 | 10 |
| Total length (cm) | 3.6 | 4.4 |
| Interaction length (%) | 8.8 | 10.8 |
| Radiation length (%) | 10 | 12.5 |

target of beryllium and the remaining portion using an eleven–segment target. The square segments were aligned with the high resolution region of the silicon microstrip detector. The nine–segment target had an overall radiation length of 10% and a proton interaction length of 8.8% whereas the eleven–segment target had 12.5% radiation length and 10.8% interaction length. Details of the target configuration are summarized in Table 3.2.

Several factors were taken into considerations in the choice of beryllium as a target material. The hadronic cross section is approximately proportional to the atomic weight, $A$, whereas the $e^+e^-$ pair production rate is proportional to the square of the atomic number, $Z^2$. To maximize the hadronic/electromagnetic production ratio one chooses a material with a large $A/Z^2 \sim 2/Z$ ratio. Another consideration is to have a target of appropriate dimensions to allow for sufficient hadronic interaction (and hence the charm production rate) while being compact enough to reduce the interaction of charmed hadrons and their decay products with the target material. Beryllium was consequently chosen as the target material since it satisfies the above requirements.

Table 3.3: Microstrip detector properties.

| Property | Station I | Station II | Station III | Station IV |
|---|---|---|---|---|
| $Z$ position (cm) | 0.0 | 6.0 | 12.0 | 24.0 |
| Active area (cm$^2$) | $2.5 \times 3.5$ | $5.0 \times 5.0$ | $5.0 \times 5.0$ | $5.0 \times 5.0$ |
| High resolution area (cm$^2$) | $1.0 \times 3.5$ | $2.0 \times 5.0$ | $2.0 \times 5.0$ | $2.0 \times 5.0$ |
| Pitch (High/Low Res.) ($\mu$m) | 25/50 | 50/100 | 50/100 | 50/100 |
| No. of channels | $3 \times 688$ | $3 \times 688$ | $3 \times 688$ | $3 \times 688$ |

## 3.2 The E687 Spectrometer

The E687 spectrometer is a large aperture, multi–purpose detector system located in the Wide Band experimental hall at Fermilab [36]. A silicon microstrip detector installed in the region close to the interaction point provides excellent vertex resolution. A multiwire proportional chamber system and two analyzing magnets allow charged particle tracking and momentum information. Three multi–cell threshold Čerenkov detectors, two electromagnetic calorimeters, and two muon systems provide charged particle identification. Neutral particles are detected by two electromagnetic calorimeters and two hadron calorimeters. In Figure 3.4 we show a schematic drawing of the E687 spectrometer, characterizing the relative size and location of individual detector components.

### 3.2.1 Silicon Microstrip Detector

The Silicon Microstrip Detector (SSD) is designed to perform high resolution tracking of charged particles in the region immediately downstream of the production point. The geometrical layout of the detector is shown in Figure 3.5 and is described in Table 3.3.

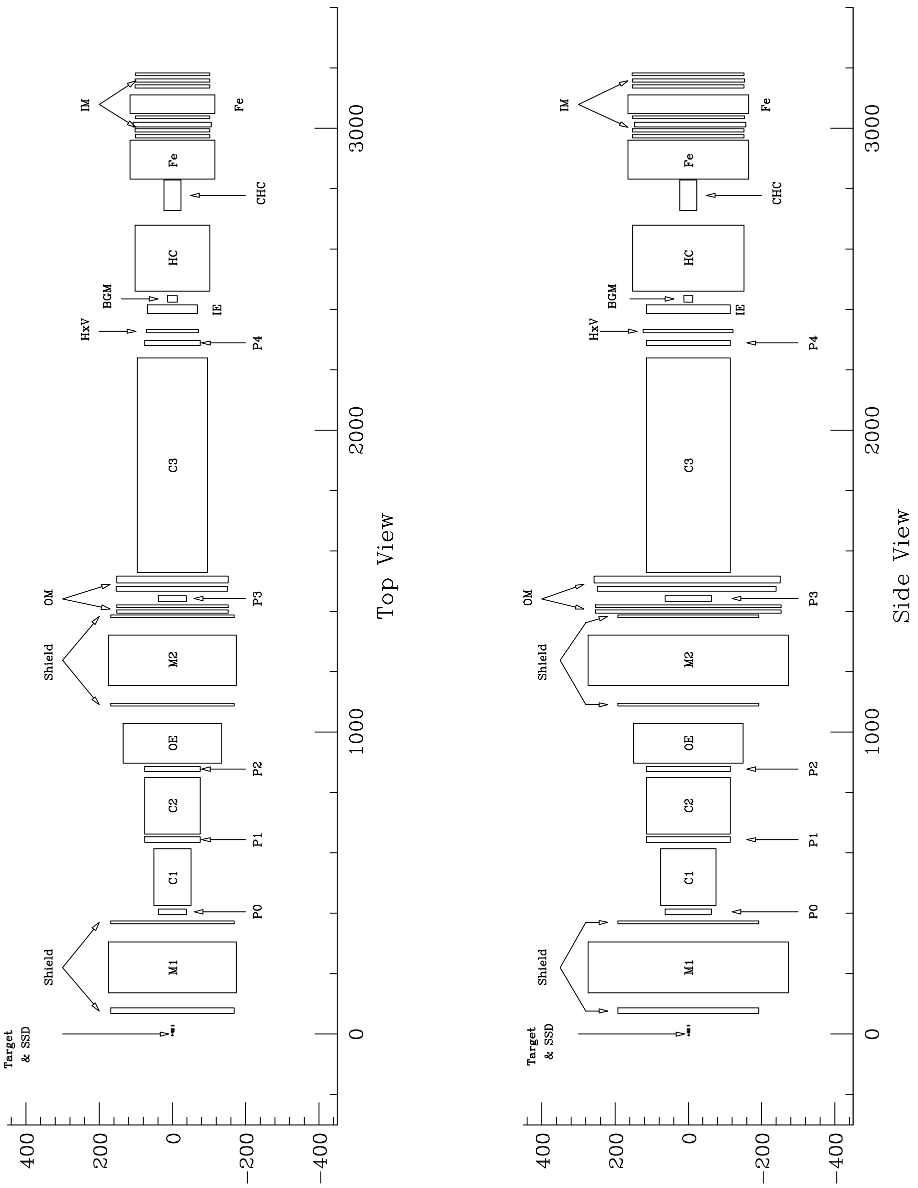


Figure 3.4: Schematic drawing of the E687 spectrometer for the 1990 configuration. Both the horizontal and vertical scales are in centimeters.

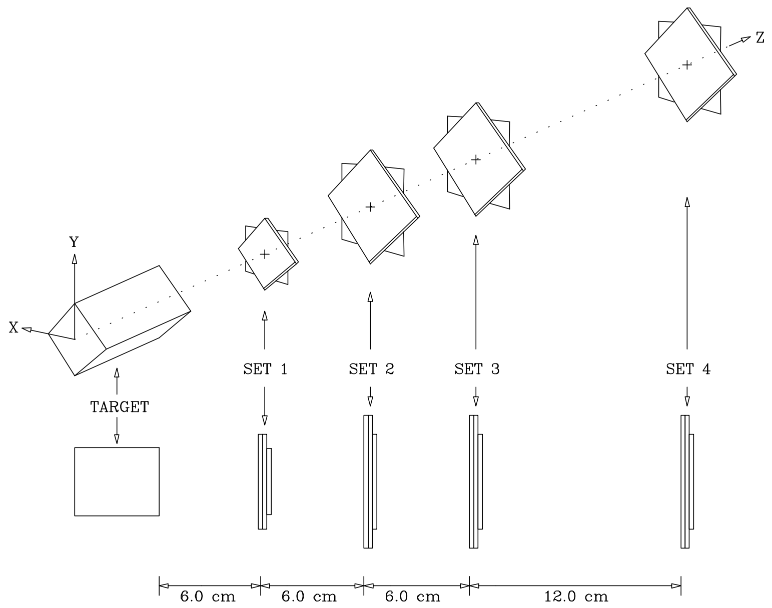


Figure 3.5: Schematic drawing of the SSD layout.

The SSD consists of twelve microstrip planes grouped in four stations of three detectors measuring $i$, $j$, and $k$ coordinates respectively. The strips of one plane in each station are oriented vertically, while the strips of the other two planes are situated at $\pm 45^0$ with respect to the horizontal axis (X-axis) of the spectrometer. In order to maximize the spatial resolution while limiting the number of electronic channels, the pitch of the silicon strips in the central region of each plane was chosen to be half size of the pitch in the outer region. This is because the central region is typically crossed by the most energetic tracks which are closer to one another and less deflected by Coulomb scattering. In addition, the pitch on the three planes of the triplet which are closest to the target was chosen to be half of the other triplets because the station nearest the target is the most important for the determination of the decay vertex.

The analog pulse height is read out for each strip. The pulse height can be used to determine if more than one track crossed a single strip, or, if two adjacent strips have a non-zero pulse height, the pulse height information from both strips can be used to find a better hit location for a single track.

The high resolution tracking upstream of the microstrip detector allows us to pinpoint a track in the target region with a precision of about $\sim$ 500 $\mu m$ in the beam direction and $\sim$ 10 $\mu m$ in the transverse direction. The overall detection efficiency of each plane is measured to be better than 99% including non-functioning strips and broken electronics channels.

### 3.2.2 Analysis Magnets

The momentum of a charged particle is determined by measuring the deflection of the particle by two large magnetic fields. The first analysis magnet (M1), located about 225 cm downstream of the target, is operated at electric current of 1,020 A to give a transverse momentum kick of 0.400 GeV/$c$. The second analysis magnet (M2), situated about 1,240 cm downstream of the target, is run at a current of 2,000 A for a transverse momentum kick of 0.850 GeV/$c$. The two analysis magnets are operated with opposite polarities, so that they bend charged particles to the opposite directions in the transverse plane (Y–view). The aperture size of each magnet is $\pm$38.1 cm in X–view and $\pm$63.5 cm in Y–view.

This particular arrangement of magnet positions and momentum kicks was made to determine its unique effect on the event topology. The ratio of the momentum kicks is designed to focus $e^+e^-$ pairs on the BGM. At a given fixed geometrical downstream detector acceptance and fixed transverse momentum kicks, the spectrometer acceptance is higher when the magnets provide opposite momentum kicks than when they bend particles in the same direction.

### 3.2.3 Multiwire Proportional Chambers

The 20 signal planes of the multiwire proportional chamber are grouped into five stations of four planes each. Each station had four different views, X, Y, U, and

Table 3.4: Properties of the multiwire proportional chamber system

| Property | P0 | P1 | P2 | P3 | P4 |
|---|---|---|---|---|---|
| active area(in$^2$) | 30×50 | 60×90 | 60×90 | 30×50 | 60×90 |
| wire spacing(mil.) | 80 | 120 | 120 | 80 | 120 |
| anode-cathode half gap(in.) | 0.235 | 0.240 | 0.240 | 0.235 | 0.240 |
| anode wire diameter(mil.) | 0.8 | 1.0 | 1.0 | 0.8 | 1.0 |
| cathode wire diameter(mil.) | 2.5 | 3.5 | 3.5 | 2.5 | 3.5 |
| equivalent tension(gram) | 65 | 90 | 90 | 65 | 90 |
| No. of X-view wires | 376 | 512 | 512 | 376 | 512 |
| No. of Y-view wires | 640 | 768 | 768 | 640 | 768 |
| No. of U/V-view wires | 640 | 842 | 842 | 640 | 842 |

V views. The U and V views are oriented to ±11.3 degrees from the Y view. The first three chambers are labeled P0, P1, and P2 and are located between the two analysis magnets. The P3 and P4 chambers are located downstream of the second analysis magnet. The P0 and P3 (Type I) chambers are located just downstream of analysis magnets and are smaller than the P1, P2 and P4(Type II). The physical properties of each chamber are summarized in Table 3.4

The gas mixture used was 65%–35% Ar-Ethane and was bubbled through ethyl alcohol at 0°C before being distributed to the system. Using this gas mixture, operating voltages of cathode planes were set to 3.30-3.50 kV for the Type I and 3.00-3.50 kV for the Type II in order to produce good efficiency.

### 3.2.4 Čerenkov Detectors

The three multicell threshold Čerenkov counters, C1, C2 and C3 are used for charged particle identification. The counters were all run at atmospheric pressure in the threshold mode. The gases were chosen such that there was a wide range of momentum values in which pions, kaons and protons could be identified. The charged particles which exceed the speed of light in the medium create Čerenkov radiation around the direction of travel if its velocity is above the certain threshold value given by:

$$\beta = \frac{pc}{E} \geq \beta_{\text{threshold}} = \frac{1}{n},$$

or, equivalently, if the momentum is above the threshold momentum:

$$p_{\text{threshold}} = \frac{mc}{\sqrt{2(n-1)+(n-1)^2}}$$

where c is the speed of light, $m$ is the mass of particle and $n$ is the refraction index of the medium. The physical characteristics of the three counters are summarized in Table 3.5

Particle identification is accomplished by noting that for certain momentum ranges and given particle masses, a counter should either be *on* (light) or *off* (no light). The identification regions for tracks are summarized in Table 3.6

Table 3.5: Characteristics of the Čerenkov counters.

| Counter | Gas | Threshold momentum (GeV/$c$) | | | No. of cells |
|---|---|---|---|---|---|
| | | pion | kaon | proton | |
| C1 | 80% He / 20% $N_2$ | 6.7 | 23.3 | 44.3 | 90 |
| C2 | $N_2O$ | 4.5 | 16.2 | 30.9 | 110 |
| C3 | He | 17.0 | 61.0 | 116.2 | 100 |

Table 3.6: Particle identification ranges.

| Particle | Momentum ranges (GeV/$c$) | |
|---|---|---|
| | 5–chamber track | 3–chamber track |
| $e$ | 0.16 – 17.0 | 0.16 – 6.7 |
| $\pi$ | 4.5 – 17.0 | 4.5 – 6.7 |
| $K$ | 17.0 – 44.3 | 17.0 – 23.3 |
| $p$ | 17.0 – 44.3 & 60.8 – 116.2 | 17.0 – 44.3 |
| $e/\pi$ | 17.0 – 61.0 | 6.7 – 23.3 |
| $K/p$ | 4.5 – 61.0 | 4.5 – 17.0 |
| $e/\pi/K$ | 61.0 – 116.2 | 30.9 – 61.0 |
| $\pi/K/p$ | 0.16 – 4.5 | 0.16 – 4.5 |

### 3.2.5 Electromagnetic Calorimeters

The Electromagnetic Calorimeters are designed to detect electrons and photons. There are two separate electromagnetic calorimeters in the E687 experiment: the Inner Electromagnetic Calorimeter (IE), covering the inner acceptances, and the Outer Electromagnetic Calorimeter (OE), ranging over wider acceptance areas.

#### Inner Electromagnetic Calorimeter

The Inner Electromagnetic Calorimeter is a lead sampling calorimeter composed primarily of one hundred alternating layers of lead and scintillating fibers sandwiched between sheets of lead.

Each lead sheet is of 0.14 cm thickness and the diameter of a scintillating fiber is 0.75 mm. The fiber orientation alternates between horizontally and vertically throughout the length of the calorimeter in order to give X and Y views. The active area is 137 cm in the non-bend (X) view and 228 cm in the bend (Y) view, with a 10 cm $\times$ 10 cm hole in the center to allow non-interacting beam photons and $e^+e^-$ pairs to pass through the calorimeter. The angular acceptance is $\pm28$ mrad in the non bend plane and $\pm47$ mrad in the bend plane. The material in the IE is the 25 cm deep, which is the equivalent of 25 radiation lengths and 1 proton interaction length. The calorimeter is segmented longitudinally into three modules, and transversely into five quadrants. The lead/scintillating fiber modules are 5, 10, and 10 radiation lengths deep respectively.

The three Pb/fiber modules are separated by two polystyrene scintillator layers. Each plastic scintillator plane is composed of 78 individual strips 0.95 cm thick and 5.08 cm wide. The strips are oriented at 45 degrees with respect to the spectrometer's Y-axis and are used to resolve ambiguities associated with multiple showers occurring in close promity to each other. These two planes are called tie-breakers and are referred to as IE1T and IE2T respectively.

A lead shield was mounted directly in front of the calorimeter for the 1991 run to absorb electromagnetic pairs. The shield is 5.08 cm wide and runs vertically along the Y axis to cover the region which experiences a high rate of the $\gamma \rightarrow e^+e^-$ events. This lead absorber is 10.16 cm deep, corresponding to 18.1 radiation lengths, and dramatically reduces the amount of energy deposited in the IE by electromagnetic pairs.

### Outer Electromagnetic Calorimeter

The OE calorimeter is located 9 m downstream of the target, just upstream of M2. The outer electromagnetic calorimeter is a lead sampling calorimeter organized into five modules. Each module is constructed of altering layers of plastic scintillator, lead and aluminum. The OE is 18.7 radiation lengths and 1.8 proton interaction lengths deep. The angular acceptance is $28 \leq | \theta_x | \leq 142$ mrad in the non-bend view and $49 \leq | \theta_y | \leq 114$ mrad in the bend view.

### 3.2.6 Hadron Calorimeters

The Hadron Calorimeter is primary designed to provide a trigger mechanism which selects hadronic events and rejects electromagnetic background events like $e^+e^-$ pairs by requiring a certain minimum hadronic energy.

Two separate devices were used to cover the inner acceptance. The main hadron calorimeter(HC), which is an iron/gas sampling calorimeter, covers the region from 5 mrad to approximately 30 mrad. The central hadron calorimeter(CHC), which is a uranium/scintillator sampling calorimeter, covers the central 5 mrad region centered directly on the photon beam. The 28 iron layers in the HC are separated by 2.86 cm and are a total of 8 interaction lengths deep. The material in the CHC is about 6.3 interaction lengths for the 1990 run and 7.3 interaction lengths for the 1991 run.

### 3.2.7 Muon Detectors

Two separate muon systems are designed in the identification of muons. The outer Muon system is designed for wide angle muon identification extending to 125 mrad and the inner muon system is used to identify muons at less than 40 mrad. In Figure 3.6, we show the layout of the muon planes and shields.

#### Outer Muon System

The outer muon system consists of two planes of proportional tubes and two planes of scintillation counters. The system uses the second analysis magnet, at 10 interaction lengths as a hadron filter.

#### Inner Muon System

The inner muon system is located at the most downstream end of the spectrometer. The electromagnetic and hadron calorimeters are used to filter out electrons and hadrons. Additional shielding is placed around the central hadron calorimeter and steel shielding is added downstream of CHC to reduce shower fragments from pions or kaons that are late to interact in the calorimeter.

The system is separated into two stations. The first station consists of a scintillator array that measures the vertical view(IM1H), a scintillator array that measures the horizontal view(IM1V), a proportional tube array that measures the horizontal view(IM1X), and a proportional tube array that measures the vertical view(IM1Y). The second station is located behind additional shielding and is identical to the first station except that no horizontal view scintillator array is used.

In 1990, a readout error has limited the utility of this system. Roughly 45% of the 1990 was affected and we do not include this data in our analysis. In 1991 the muon system was altered to allow the passage of the photon beam through the detector. A cell of 8 counters was removed from each proportional tube array and the arrays were shifted so that the resultant gap would be centered on the beam. The frame supporting scintillator counters had to be modified and holes were cut in the scintillator planes.

### 3.2.8 Triggering

The purpose of trigger in the experiment is to isolate the interesting events from undesirable ones. In E687 the number of interactions per spill produced by photon beam impinging on the target is about $10^7$ and the production of electromagnetic events ($\gamma Be \rightarrow e^+e^-$) is about 500 times to hadronic production. The data acquisition system which operated in the kHz range and was unable to tolerate at such high rate. The E687 trigger system was designed to trigger hadronic events and to reject electromagnetic events and low energy photon events. The triggering is done in two stages to achieve the above goal.

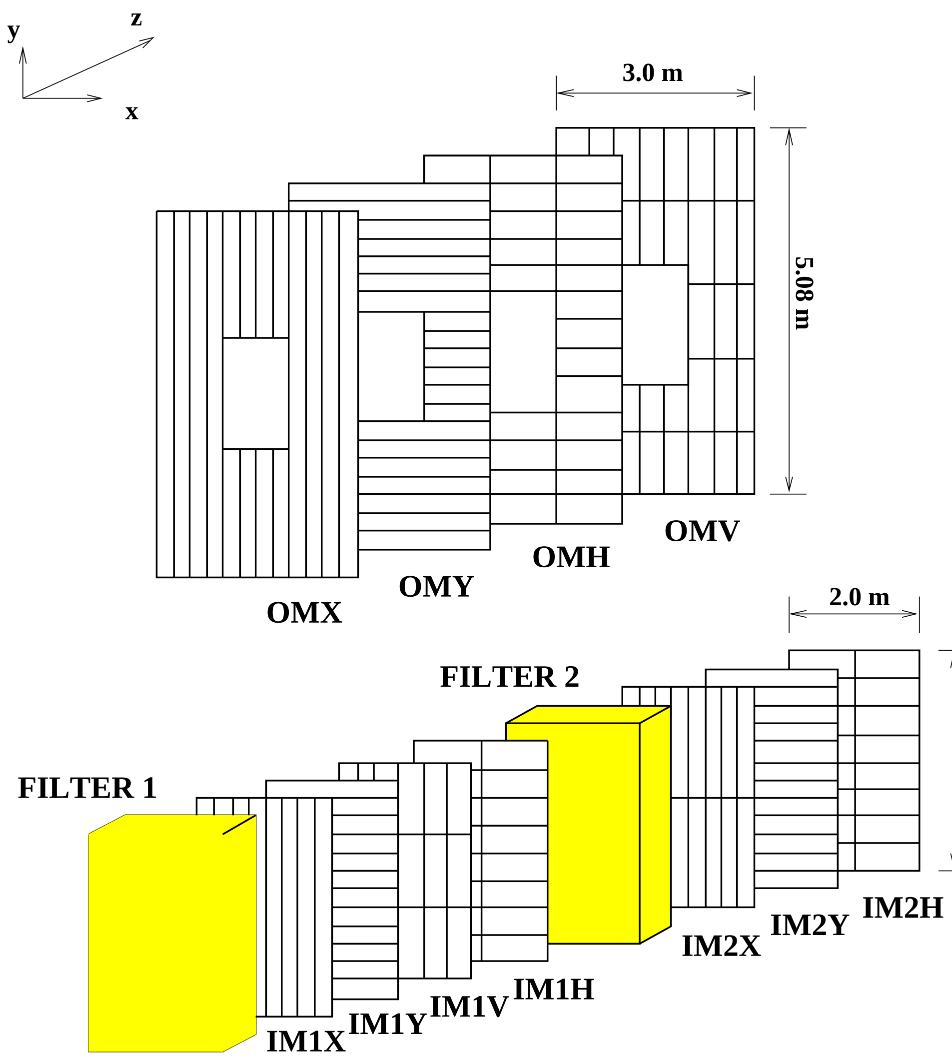


Figure 3.6: Muon detector configuration: a) for Outer Muon b) for Inner Muon

**First Level Trigger**

The first level trigger, called the master gate (MG), consists of the coincidence of signals from various fast scintillation counters.

A0 and A1 are small counters placed just upstream of target and used to veto an event if there is a charged particle in the upstream photon beam. TM1 and TM2 are large scintillation counters placed directly downstream of the A1 counter with a hole in the center. TM1 and TM2 were installed to veto events in which an off-axis muon is coincident with an interacting photon. It turns out that the bulk of the vetoing power comes from the A0 and A1 counters, and the TM1 and TM2 counters are used in only a fraction of the data.

Two scintillator counters are positioned around microstrip detectors to determine whether a charged particle has passed through the SSD. A scintillation counter(TR1) is placed between the target and the microvertex to detect the charged particles that come from interactions in the target. Another scintillation counter(TR2) is placed directly downstream of the microvertex. TR1 is 2.5 cm $\times$ 3.5 cm to match the dimensions of the microvertex planes, TR2 is 22 cm $\times$ 22 cm which is much larger than TR1 in order to accept wide angle tracks exiting the microstrip detector. A coincidence of TR1 and TR2 is required to ensure that a photon interacted in the target. The placement of the counters used in the master gate is shown in Figure 3.7

The OH array is a plane of scintillation counters located between P2 and the OE with 48.6 cm $\times$ 83.2 cm aperture in the center to allow the $e^+e^-$ pairs to pass through. OH is oriented only in the horizontal direction and is designed to cover the wide angle portion of the spectrometer. The H$\times$V hodoscope is located between P4 and the IE and comprised of 24 horizontal and 12 vertical scintillation counters. The array has a 9.7 cm vertical gap along the center to avoid triggering of $e^+e^-$ pairs which populate the region of the gap. In 1991 we added a plane of scintillation counters, $V'$ behind the IE and a lead bar in front of the IE that covers

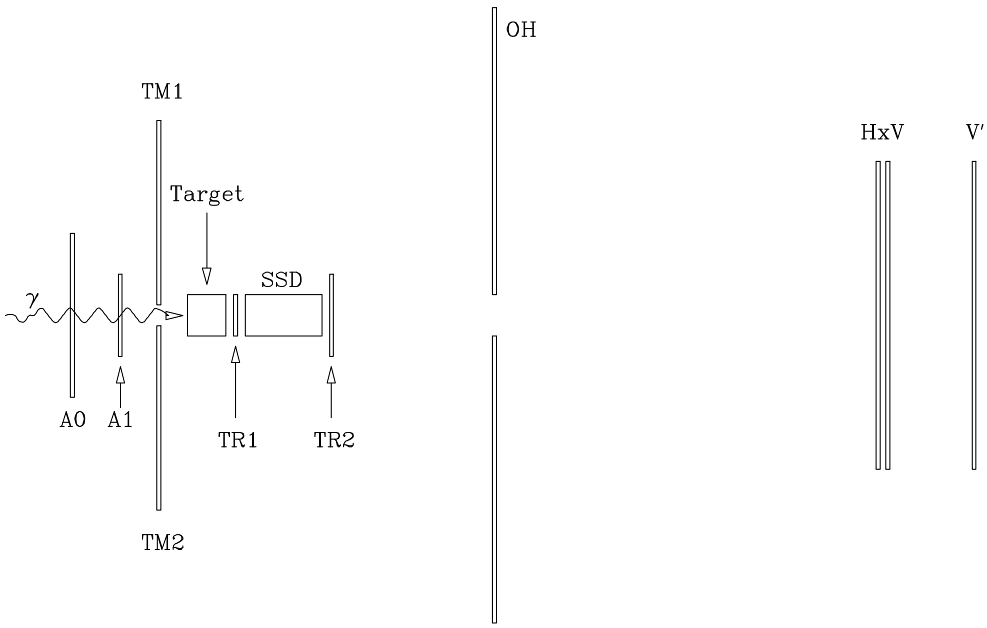


Figure 3.7: Schematic arrangement of the first level trigger counters.

the region expected $e^+e^-$ pair events. The $V'$ counters work with the H counters to further reduce the pair contamination by taking advantage of the shielding power of the IE. The OH and H×V together cover almost the entire acceptance of the spectrometer. The H×V and OH are used in trigger two ways: the inner-inner trigger, which requires at least 2 separate tracks traverse the H×V array, and the inner-outer trigger, which requires at least 1 track to traverse the H×V array and 1 track to pass through the OH array. The first level trigger configurations for various run periods are listed in Table 3.7. In the table $(\mathrm{H}\times\mathrm{V})_1$ indicates at least one particle traversed the H×V array, and $(\mathrm{H}\times\mathrm{V})_2$ indicates at least 2 separate particles traversed the H×V array.

The MG requirement rejects about 90% of the $e^+e^-$ pairs, while being 90% efficient in retaining hadronic events. The rate of events passing through the first level trigger is around 50 kHz, i.e., around $10^6$ per spill. The ratio of electromagnetic

Table 3.7: First level trigger configurations.

| First level trigger logic | Duration |
|---|---|
| TR1·TR2·$(\mathrm{H}\times\mathrm{V})_2\cdot\ \overline{(\mathrm{A0}+\mathrm{A1})}$ | 26 % of 1990 |
| TR1·TR2·$[(\mathrm{H}\times\mathrm{V})_2+\mathrm{OH}\cdot(\mathrm{H}\times\mathrm{V})_1]\cdot\ \overline{(\mathrm{A0}+\mathrm{A1})}$ | 74 % of 1990 |
| TR1·TR2·$[(\mathrm{H}\times\mathrm{V})_2+\mathrm{OH}\cdot(\mathrm{H}\times\mathrm{V})_1]\cdot\ \overline{(\mathrm{A0}+\mathrm{A1})}$ | 8 % of 1991 |
| TR1·TR2·$(\mathrm{H}\times\mathrm{V})_2\cdot\ \overline{(\mathrm{A0}+\mathrm{A1})}$ | 5 % of 1991 |
| TR1·TR2·$[(\mathrm{H}\times\mathrm{V}')_2+\mathrm{OH}\cdot(\mathrm{H}\times\mathrm{V}')_1]\cdot\ \overline{(\mathrm{A0}\cdot\mathrm{A1})}$ | 87 % of 1991 |

events to hadronic events remains still large (approximately 15:1) and the rate is still too high for the data acquisition system. We will have to include a second level trigger in order to reduce the rate furthermore.

### Second Level Trigger

The second level trigger has been designed to further reduce the event rate and select the hadronic events by combining topological and kinematic requests. In the basic configuration, an event is selected on the following basis:

- the pattern of hits detected by the first station of the MWPC is consistent with at least three charged tracks outside the $e^+e^-$ pair region
- the energy deposited in the hadron calorimeter is at least 40∼50 GeV. (during the 1990 run the energy deposited in the CHC was included).

This trigger requires about 1.2 $\mu$s to process information latched by the master gate and to decide whether to read out the event or to execute a clear cycle. The trigger operates on signals which are latched and pulse heights which are integrated and stored when a master gate occurs. The second level Buslines are given in Table 3.8.

Table 3.8: Second level trigger buslines

| Busline | Description |
|---|---|
| 0 | Muon Anti, AM>0 |
| 1 | Particle in A0 counter |
| 2 | RESH energy > ELOW |
| 3 | RESH energy > EMED |
| 4 | RESH energy > EHIGH |
| 5 | RESH Veto |
| 6 | Silicon Wafer trigger |
| 7 | Muon Anti, (AM>0)·(AMD>0) |
| 8 | Reserved for calibration |
| 9 | Reserved for calibration |
| 10 | 2 muons in IM system |
| 11 | 2 muons in OM system |
| 12 | 1 IM muon, 1 OM muon |
| 13 | 1 IM muon |
| 14 | 1 OM muon |
| 16 | Hadron energy > ETOT1 |
| 17 | Hadron energy > ETOT2 |
| 19 | Hadron energy > ETOT3 |
| 20 | Hadron energy > ETOT4 |
| 22-27 | Cuts on multiplicity |
| 28 | Prescale |
| 31 | INHIBIT |

The OR logic of all the trigger modules constitute the second level trigger. The data acquisition is disabled for an interval need by the second level electronics to make a level-two trigger decision. If the second level trigger does not fire, a clear cycle is initiated which contributes an extra 1 $\mu$s to the deadtime before the master gate is again checked. If the second level trigger is satisfied, then a full readout and automatic clear cycle is initiated.

## 3.3 Data Acquisition System

Once the master gate and second level trigger requirements are satisfied, the E687 Data Acquisition (DAQ) system, with processing capability of about 4,000 triggers per minute of 4 kB each in size, is alerted to begin the process of transferring data to tape. All signals from the detectors are digitized and sent via five data streams to LeCroy Fastbus memories(4 MB each) as schematically shown in Figure 3.8. The average readout time for each stream is listed in Table 3.9. Further master gates are inhibited for about 1.4 ms to prevent the pile-up of events while the data from an accepted event is being processed. Approximately 30 % of all the first level triggers are lost due to the dead time generated by the second level trigger and DAQ system. During the 20 second spill time about 3,000 events satisfy the second level trigger and are stored in the memories. During the 40 second inter-spill time, data from the memories are then transferred to data tape. A total of four 8 mm tape drives may be written in parallel. Each tape can contain up to 2 GB of data corresponding to about 500,000 E687 raw events.

The E687 collaboration took data in two separate periods: May 1990 – September 1990 and July 1991 – January 1992. A total of about 280 million triggers in the first run period and about 240 million in the second run period were recorded to approximately 1,000 8mm tapes.

Table 3.9: Average readout times for data streams.

| Data stream | SSD | Latches | TDC | ADC(1) | ADC(2) |
|---|---|---|---|---|---|
| Read–out time ($\mu$s) | 20 | 50 | 300–600 | 1000 | 1000 |

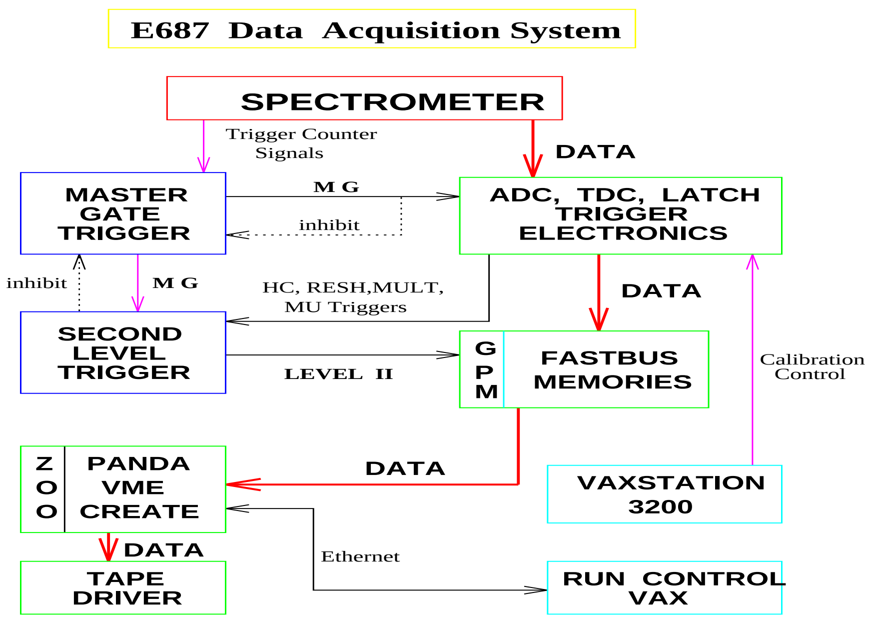


Figure 3.8: Schematic of E687 data acquisition system

# Chapter 4

# Data Reconstruction

As a first stage of data analysis, we have to reconstruct raw data which contain the basic information of pulse heights, arrival times, and hits from various detectors.

The E687 reconstruction process, called PASS1, involves determination of charged and neutral particle momentum or energy and trajectories, identifying particle types using the Čerenkov counters, calorimeters, and muon systems, and forming particles using reconstructed vertices and masses.

In this chapter we describe the algorithms employed to reconstruct the raw data based upon information from the various detectors. Detailed attention is paid to the $\Xi^-$ reconstruction which is essential in this analysis. More detailed description of overall reconstruction processes may be found elsewhere [36].

## 4.1 Charged Particle Tracking

Charged tracks are reconstructed by pattern recognition algorithms from the hits recorded in the SSD and MWPC detectors. Tracks are reconstructed separately in the two detectors, then linking algorithm combines information from these two detectors to look for their matches.

### 4.1.1 SSD Track Reconstruction

In the first stage of the reconstruction, a very conservative analysis of the valid hits is performed on the basis of the released charge. A charged particle passing through a silicon plane deposits energy in the planes.

The tracking algorithm starts by finding two dimensional projections using hits from each of three views. Sharing of hits among different tracks is permitted except for one special case. Hits in the last three stations, already assigned to a track having hits on all four stations can not be used again to form a new track with only three hits. Projections are formed into tracks if they match in space and have a global $\chi^2$ per degree of freedom (DOF) lower than 8. This process is performed in a fully symmetric way with respect to the $i$ and $j$ views, selecting only the best $j$ and $k$ association for each $i$ projection and again only the best $i$ and $k$ association for each $j$ projection. At this point, hits not associated with any tracks are used to search for wide angle tracks and for segments of highly multiple Coulomb scattered tracks. This search is performed by a direct match of hits in space. A track of this type is required to have at least six hits.

The overall track reconstruction efficiency is found to be 96% for simulated photoproduced $D\bar{D}$ events, approaches 99% at a momentum of 10 GeV/$c$ and retains a value of about 90% at 2.5 GeV/$c$ . The relative percentage of spurious tracks is estimated to be about 2.7%.

The resolution of a microstrip track is expressed as the transverse position error when the track is extrapolated to the center of target. The resolution for a track passing through the high resolution region of SSD has been calculated to be:

$$\sigma_x = 11 \sqrt{1 + (\frac{17.5 \text{ GeV/c}}{\text{p}})^2} \ \mu\text{m}$$

$$\sigma_y = 7.7 \sqrt{1 + (\frac{25.0 \text{ GeV/c}}{\text{p}})^2} \ \mu\text{m} \tag{4.1}$$

The largest contribution to the constant term is associated with microstrip granularity. Multiple Coulomb Scattering (MCS) effects due to the target, the SSD, and the TR1 trigger counter are also included. The resolution is better in the Y coordinate than in X coordinate since all the three SSD views provide Y information, while only two of them give X information.

### 4.1.2 MWPC Track Reconstruction

Tracks are reconstructed from hits in the MWPC by forming projections in each of the four chamber views. In the U, V, and Y (bend) views, projections are made using information from the MWPC alone. In the non-bend X view, hits are first formed using a seed from the SSD by searching for MWPC hits which match the SSD track extensions. Tracks are formed by matching all four projections. After all tracks originating from an SSD extension are found, unused hits in the X view are considered for reconstruction of new X projections. These projections are then matched to unused U, V, and Y projections to form additional tracks.

A least square fit is performed on all candidate tracks. The fit parameters are the intercepts and slopes of the track in the both X and Y views at the second analysis magnet (M2). A minimum $\chi^2/DOF$ is required for each track. Tracks were not permitted to have more than 4 missing hits among all the chambers, nor more than 2 missing hits in any single chamber.

After the main set of MWPC tracks is formed, the algorithm tries to recover track topologies which are previously missed. A microstrip extension routine is designed to recover these tracks. This routine extends microstrip tracks into the MWPC system by using the microstrip track parameters to predict hits in P0, P1, and P2. Only X hits deviating from the predicted X positions by less than two wire spacings are used. Once an X projection is found, unused U, V, and Y hits are used to form space points in the chambers. Tracks extending only to P0 are required to have hits in all the four views, tracks extending to P0 and P1 may have one missing hit in each station. These new tracks are then fitted and MWPC track parameters are determined.

The efficiency of the MWPC tracking algorithm has been studied using a Monte Carlo simulation which models the efficiencies of the individual chamber planes. The efficiency has been determined to be better than 98% with less than 0.5% spurious tracks for tracks with momentum exceeding 5 GeV/$c$ . Since events with extremely high multiplicity usually result from chamber oscillations, an artificial limit of 30 tracks per event has been imposed in order to reduce reconstruction time.

### 4.1.3 Linking

Once tracks are reconstructed in both SSD and MWPC, linking of the MWPC track to the SSD track is one of the most important processes in the data analysis. The primary purpose of linking is to provide the momentum for tracks passing through the microstrip detector which then pass through the first analysis magnet and into the spectrometer. Additionally, unlinked microstrip tracks are available for use in reconstructing particles that decay downstream of the microstrip detector. For example, unlinked MWPC tracks are used as candidates for the neutral vees ($K_s^0$ and $\Lambda$) and long-lived hyperons ($\Sigma$, $\Xi$, $\Omega$, and so on) decay products.

The linking is accomplished by extending both SSD and MWPC tracks in opposite directions to the center of M1. The slopes and M1 intercepts of these two extensions are required to be consistent. A first pass with loose cuts is made to remove unreasonable links. Candidate links are subject to a global least-square-fit which uses all the SSD and MWPC hits associated with track. Multiple links are arbitrated based on the $\chi^2/DOF$. A maximum of two MWPC tracks are allowed to be linked to the same microstrip track.

As shown in Figure 4.1, the linking efficiency is about 94% for high momentum 3 chamber tracks and about 98% for high momentum 5 chamber tracks. There is a signification reduction in efficiency at low momentum due to multiple Coulomb

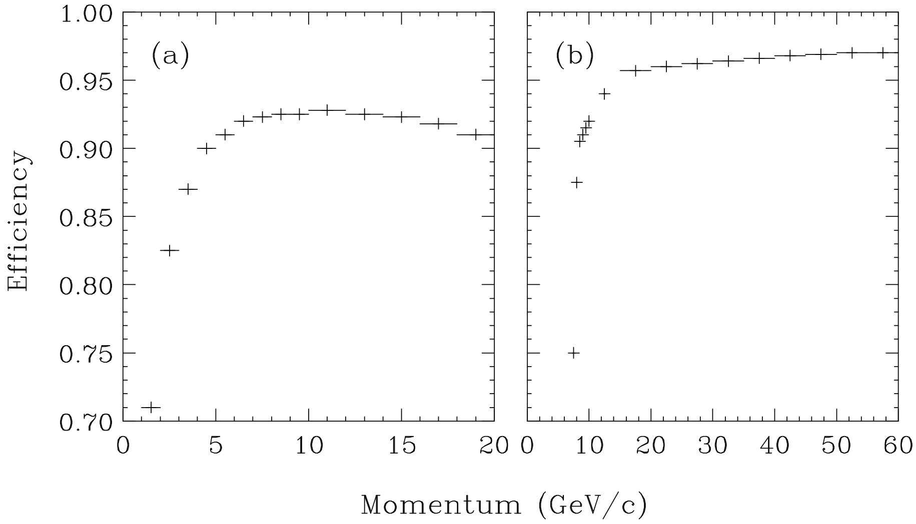


Figure 4.1: Linking efficiency between the SSD and MWPC tracks: (a) for 3–chamber tracks and (b) for 5–chamber tracks.

scattering.

## 4.2 Vertex Reconstruction

Stand alone vertex algorithm uses the microstrip tracks to determine the complete vertex topology of the event. As a first stage, the vertexing algorithm assigns all the tracks to a common vertex. A least square fit is accomplished to compute $\chi^2$:

$$\chi^2 = \sum_{i=1}^{n} \left( \frac{x - (x_i + a_i z)}{\sigma_x^i} \right)^2 + \left( \frac{y - (y_i + b_i z)}{\sigma_y^i} \right)^2$$

where $(x,\ y,\ z)$ is the vertex coordinates (which are the fit parameters), $a_i$, $b_i$, $x_i$, and $y_i$ are the slopes and intercepts of the $i$th track, and, $\sigma_x^i$ and $\sigma_y^i$ are the errors associated with the SSD track parameters. The tracks giving the largest $\chi^2$ contribution are removed from this vertex until the $\chi^2$ of the vertex is smaller than the specified value. This procedure is iterated until all possible vertices are identified.

At the end of the procedure, a complete SSD vertex topology of the event is constructed and each SSD track is either definitely assigned to a specific vertex or remains unassigned. The most upstream SSD vertex is selected as the primary vertex in the event and is referenced by some other reconstruction procedures. If no SSD vertex in a particular event is found, the center of the target is considered as the primary vertex.

## 4.3 Momentum Determination

Charged particle momentum is determined by measuring the deflection by a magnetic field. The various topologies of tracks require different techniques to measure a particle momentum. For a 5-chamber track, which passes through the second analysis magnet, the track parameters upstream and downstream of M2 are fit to determine the particle momentum. An iterative least-square-fit is performed until the track parameters are stabilized.

For a 3 or 4 chamber linked track, the particle momentum is determined from deflection through M1 using downstream MWPC track parameters and microstrip linked track parameters. For an unlinked 3 chamber track, we assume that the particle was created at one of the vertices found by the stand alone algorithm described above. The X projection of the track is traced upstream to the target and the closest vertex is chosen as the particle production point. If no vertex is matched, we assume the particle is created at the center of target.

The momentum resolution of the charged particles using M1 is:

$$\frac{\sigma_{\mathrm{p}}}{\mathrm{p}} = 3.4\ (\frac{\mathrm{p}}{100\ \mathrm{GeV/c}})\ \sqrt{1 + (\frac{17\ \mathrm{GeV/c}}{\mathrm{p}})^2}\ \% \tag{4.2}$$

For 5-chamber tracks measured by M2, the momentum resolution is given by:

$$\frac{\sigma_{\rm p}}{\rm p} = 1.4\ (\frac{\rm p}{100\ {\rm GeV/c}})\ \sqrt{1 + (\frac{23\ {\rm GeV/c}}{\rm p})^2}\ \% \tag{4.3}$$

The momentum dependent term is due to multiple Coulomb scattering which contributes to resolution dominantly at low momentum.

## 4.4 Particle Identification

The bulk of the charged particle identification is carried out with using information from the three Čerenkov counters. For electrons though, the information from the electromagnetic calorimeters is used, and for muons, we can use the hit information from the muon counters for identification as well.

### 4.4.1 Čerenkov Identification

The Čerenkov algorithm uses the light patterns observed in the three Čerenkov counters to test a given particle hypothesis for a measured particle momentum. The algorithm categorizes each charged track as either electron, pion, kaon, or proton. These 4 particles, which comprise the majority of all tracks emitting Čerenkov radiation in the experiment, have different threshold momenta at which they begin to radiate. More detailed description is already given in section 3.2.4.

The algorithm begins by first setting up an *on/off* code for each cell in each detector. This is determined by the presence or absence of a phototube pulse height above a threshold value. Using the track momentum and threshold in a given counter, an anticipated light yield based on photoelectron calibration of the counters is calculated for each particle hypothesis. The comparison of the actual and anticipated responses is made for each of three Čerenkov counters (the C3 response is only applicable for 5–chamber tracks). Each track is assigned a particular Čerenkov classification describing the possible particle hypothesis using combined information from the counters. The possible particle identification codes are listed in Table 4.1.

The expected Čerenkov radiation cones for different particles may overlap which causes confusion when assigning an *on/off* code for a given cell and track. If there are no unshared cells for a given track and the shared cells detected Čerenkov light, the Čerenkov algorithm returns a *confused* status. Counters with a *confused* status are not included in making decisions. A small amount of confusion is accepted which biases the status towards *on*. This bias creates an efficiency loss for heavy particles (kaons and protons) but also decreases the number of $\pi$'s and $\mu$'s misidentified as kaons or protons.

Table 4.1: ISTATP codes.

| ISTATP | Particle Identification |
|---|---|
| 0 | inconsistent |
| 1 | $e$ definite |
| 2 | $\pi$ definite |
| 3 | $e/\pi$ ambiguous |
| 4 | $K$ definite |
| 6 | $\pi/K$ ambiguous |
| 7 | $e/\pi/K$ ambiguous |
| 8 | $p$ definite |
| 12 | $K/p$ ambiguous |
| 14 | $\pi/K/p$ ambiguous |
| 15 | total confusions |

The Čerenkov detection efficiency has been determined to be about 75% for kaons and about 80% for protons. Monte Carlo studies indicate that the Čerenkov system performs as expected [32].

### 4.4.2 Inner Electromagnetic Calorimeter Showers

There are two primary applications of electromagnetic calorimetry, photon reconstruction and electron/hadron discrimination. The IE shower reconstruction algorithm relies heavily upon a discriminant analysis to distinguish between electromagnetic and hadronic showers. Data from both the electron calibration and the pion calibration runs are used as training samples for a discriminant analysis. A more detailed description of the discriminant analysis may be found elsewhere [32].

Showers which deposit energy only in the middle module are automatically labeled as electromagnetic showers, and those showers beginning in the farthest downstream module are identified as hadronic showers.

The reconstruction efficiency for calibration electrons is about 90%, while the identification efficiency for electron pairs ($\gamma \to e^+e^-$) in data is significantly lower, about 62%. This is due to additional showers and pattern recognition failures.

All showers which are not associated with charged tracks are identified as neutral showers and subject to another discriminant analysis to separate photons from hadrons. The training samples for the neutral discriminant analysis are electrons and pions from calibration runs. The input variables are identical to those used in the charged particle analysis except for $E/p$. After photons have been identified they are used to reconstruct the decay $\pi^0 \to \gamma\gamma$.

### 4.4.3 Muon Identification

The muon identification is accomplished with projection of MWPC tracks to the inner muon system and searching for a $3\sigma$ scattering radius for hits in the detectors of the inner muon system. If more than one match is found in a proportional tube plane for a track, the closest hit is kept for later reference.

If a track has matched 5 or more planes out of a possible 7, we consider it a muon and we assign it a code shown in Table 4.2 based on its shared hit history. In practice, if IDMU $\neq 0$, we call the track a muon.

Table 4.2: MUON identification codes

| Code (IDMU) | Meaning |
|---|---|
| 4 | 3 shared hits, 4 unshared hits |
| 3 | 2 shared hits, $>2$ unshared hits |
| 2 | 1 shared hits, $>1$ unshared hits |
| 1 | 0 shared hits, Muon definite |
| 0 | Not a Muon |
| -1 | 1 shared hits, $\leq 1$ unshared hits |
| -2 | 2 shared hits, $\leq 2$ unshared hits |
| -3 | $>2$ shared, hits $<4$ unshared hits |

For muon particles below 30 GeV/$c$ , some particles do not reach the second bank. It is possible to have muons that penetrate only to the first bank of the inner muon system or that have scattered outside the 3 $\sigma$ search zone by the time they reach the second bank. This is due to energy loss in the absorption material. The identification requirements for a particle below 30 GeV/$c$ were relaxed so that a previously lost muon could be recovered if it matched 3 or 4 planes in the first bank. There was a bug in the muon identification code that began to effect ID below 30 GeV/$c$more strongly. The original E687 code did not include all 3 $\sigma$ MCS radii when matches were searched for with the scintillation counters. Since these counters were big, the bug did not cause a large effect until we started to reach low momenta. In reality, the muon system is highly efficient (about 99 %) even below 10 GeV/$c$, but the bug prevented us from realizing that efficiency. More detailed descriptions can be found in reference [33, 34].

Sometimes, the number of hits in the inner muon system is large. If there are more than 20 hits in any single plane of the muon system, we drop all the hits from that particular plane. While this is not a problem in the original configuration, we find that a lost plane occurs for about 5% of events in the 1991 data where a muon is present. Figure 4.2 is a single track efficiency expected for the 1990 inner muon system using the simulated data.

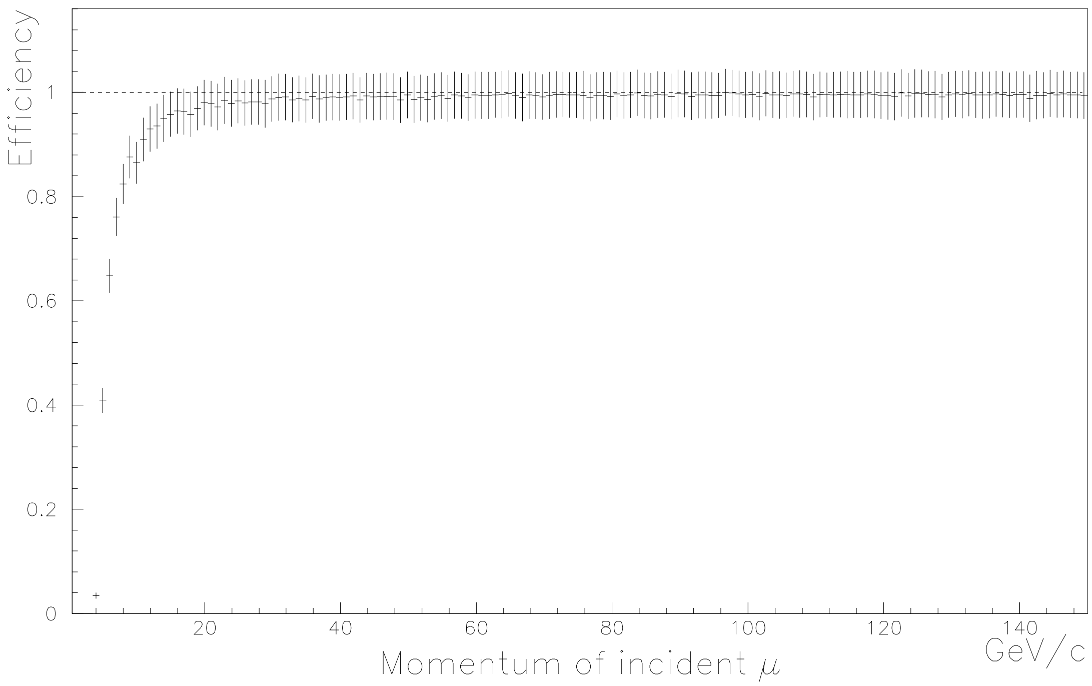


Figure 4.2: Expected efficiency vs muon momentum for the 1990 muon system.

## 4.5 Neutral Vees

The neutral vees, $K_s^0$ and $\Lambda$ are often found among the decay products of the charmed hadrons. In E687, these particles are reconstructed through the charged decay modes:

$$K_s^0 \longrightarrow \pi^+\pi^- \qquad (\text{BR} = 68.6\%)$$
$$\Lambda \longrightarrow p\pi^- \qquad (\text{BR} = 63.9\%)$$

These particles have long lifetimes relative to charm particles, and may travel several meters within the spectrometer before decaying. From the decay region, as shown in Figure 4.3, vees are categorized: 'SSD vees' which decay upstream of the microvertex detector; 'MIC vees' which decay inside microvertex detector; 'M1 vees' which decay between the last station of SSD and the first MWPC station, P0; and 'Reconstruction vees' which decay between P0 and P2. A total of about 10 m of decay length is covered. Despite the diversity of the possible topologies, the vee reconstruction algorithm essentially seeks pairs of oppositely charged tracks which form a common vertex. The invariant mass of the pair tracks is calculated by assigning both charged tracks pion masses to form a $K_s^0$ hypothesis. Similarly a $\Lambda$ invariant mass is calculated by assigning the higher momentum track a proton mass and the softer track a pion mass. Thus, each vee has an invariant mass for both the $K_s^0$ and the $\Lambda$ hypotheses. Later analysis must be done carefully, since a *true* $K_s^0$ may also be identified as a $\Lambda$ or vice versa. No Čerenkov identification is required at this stage.

Figure 4.4 shows the vee invariant mass distributions of the $K_s^0$ hypothesis for different vee categories. Note that the $K_s^0$ mass distributions shown in Figure 4.4 do not represent the whole E687 data sample but are representative of the overall data quality. The invariant mass plots of the $\Lambda$ hypothesis are shown in Figure 4.5 for different vee types. The $\Lambda$ mass distributions are obtained from the entire E687 data sample with the requirements discussed in section 4.8.

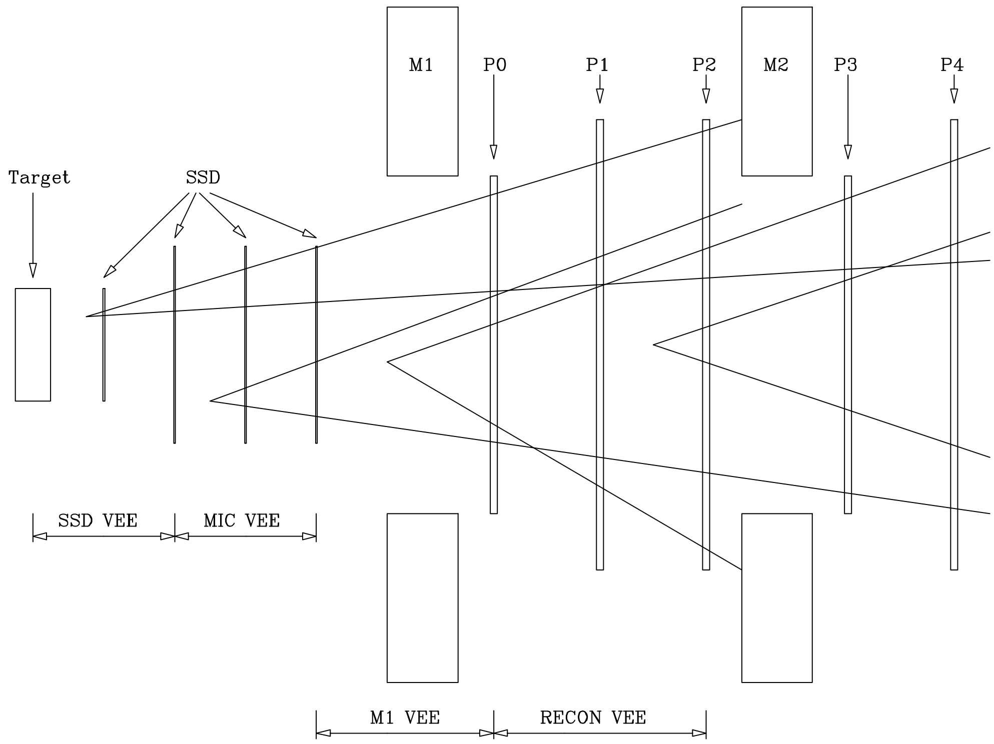


Figure 4.3: Schematic drawing of regions where vees are reconstructed with different algorithms.

### 4.5.1 SSD Vees

SSD vees are reconstructed from all pairs of oppositely charged SSD tracks which are linked to MWPC tracks and form a common vertex. The vee vertex is required to be at least $20\sigma_z$ downstream of the primary vertex ($\sigma_z$ is the error calculated for the distance between the primary and vee vertices) and the vee momentum must point back to the primary vertex within 1 mm in the transverse plane to reduce the combinatoric background. Although the decay volume for this topology is small, about 10 cm in Z, the SSD vees are important because the track vector of the SSD vee has resolution comparable to that of an SSD track.

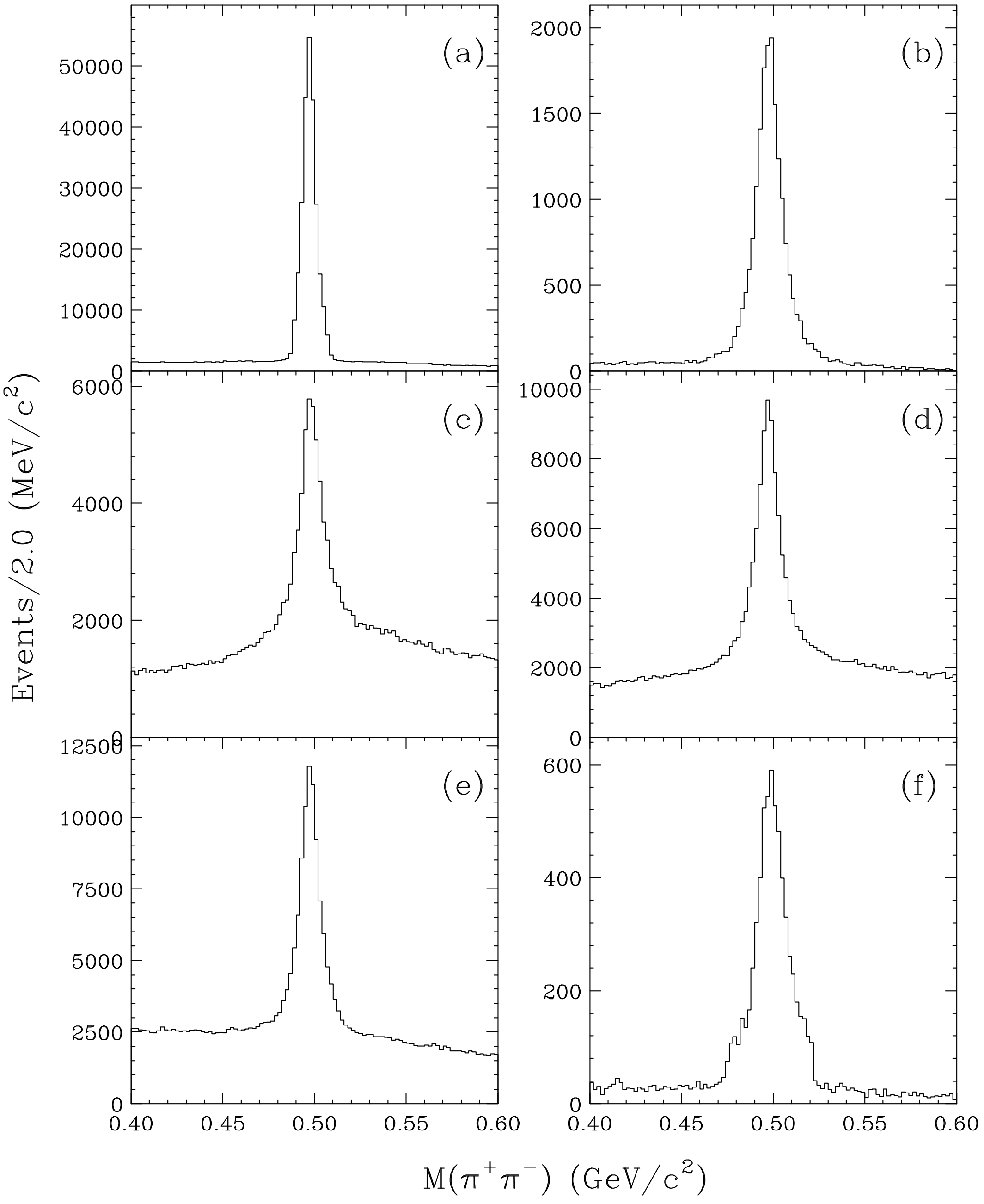


Figure 4.4: Vee invariant mass plots for the $K_s^0$ hypothesis: (a) SSD vees, (b) MIC vees, (c) Stub–Stub vees, (d) Track–Stub vees, (e) Track–Track vees, and (f) RECON vees.

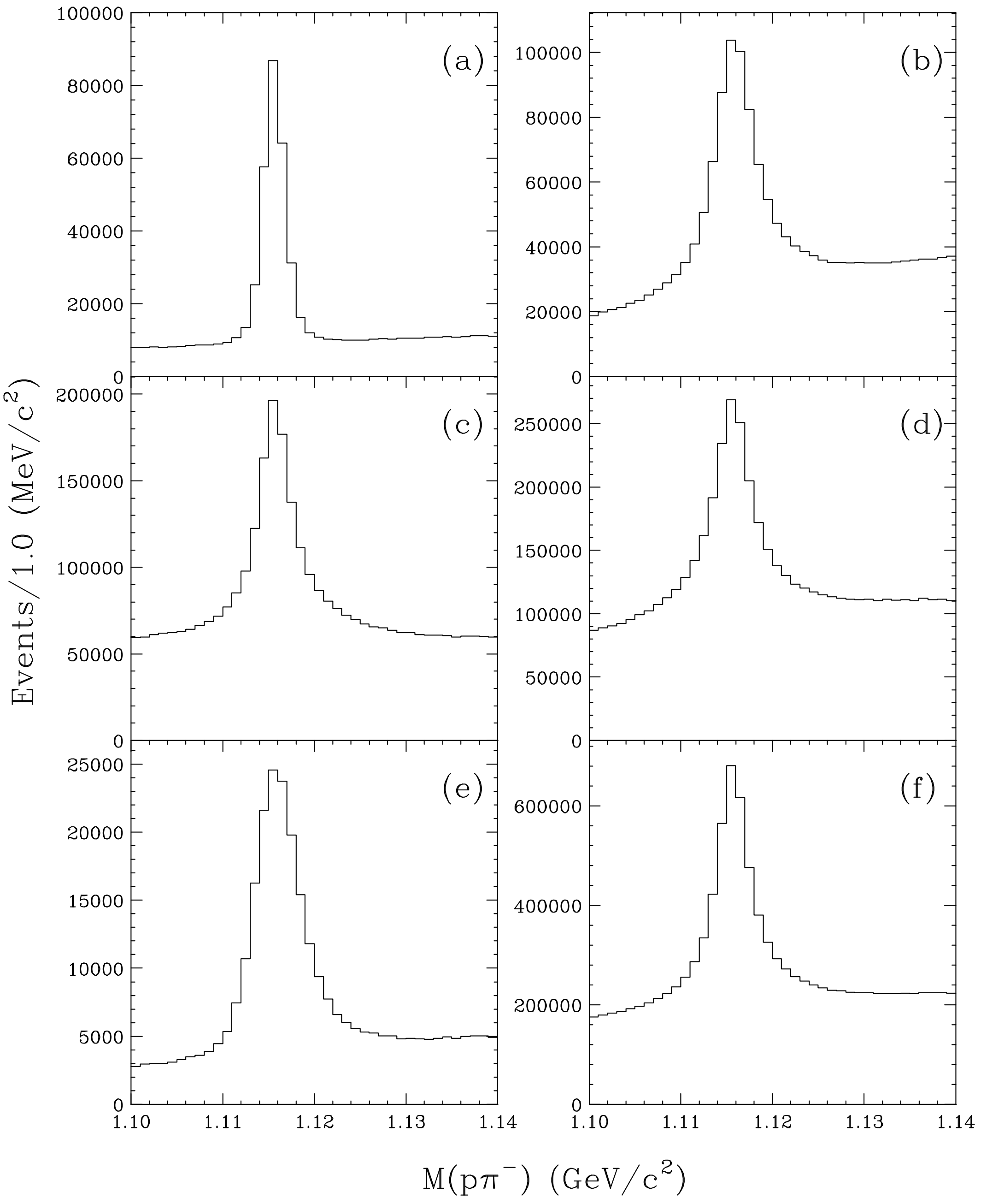


Figure 4.5: Vee invariant mass plots for the $\Lambda$ hypothesis: (a) SSD vees, (b) Stub–Stub vees, (c) Track–Track vees, (d) Track–Stub vees, (e) RECON vees, and (f) All vees.

### 4.5.2 MIC Vees

The MIC vee decays somewhere between the second and last stations of microvertex detector. This region is 18 cm in length and contains about 10% of the observed $K_s^0$ decays. The MIC vee algorithm begins by extrapolating unlinked MWPC tracks into the last SSD station and forming triplets from unused hits in the station. The transverse distance between each triplet and the extrapolated MWPC track under consideration is computed. If a triplet is found such that this distance is smaller than a certain value, the SSD hits are included in a global refit to the MWPC track parameters and the track is extrapolated back to the next station. At this stage, each MWPC track may have several triplets associated with it in the last SSD station. Now a search is made for triplets in the third SSD station, which match with the track, in the same manner with the previous search. The triplets, or pairs of triplets, associated with a single MWPC track are arbitrated on the basis of $\chi^2$ from a global fit to all hits associated with each candidate.

All combinations of oppositely charged candidate tracks are paired together and the distance of closest approach (DCA) is computed for each. Only pairs with a reasonably small DCA are kept. If more than one pair contain the same candidate track, only the one with the minimum DCA is retained.

### 4.5.3 M1 Region Vees

The majority of vees are reconstructed in the M1 region, which covers the area between the last SSD station and the first MWPC station. The M1 region vees are reconstructed using unlinked MWPC tracks. There are three topologies: *track–track* vees, consisting of two 5–chamber tracks; *track–stub* vees, consisting of one 5–chamber track and one 3–chamber track; and *stub–stub* vees, consisting of two 3–chamber tracks.

The basic idea of the algorithm is the same for all three topologies. For the candidate pair of unlinked MWPC tracks, the X and Z locations of a vee decay vertex are first estimated by intersecting the two daughter tracks in the X-view (non-bend). An iterative procedure then traces the two tracks through the M1 field to determine the Y position of the vee vertex. In the case of the track–stub vee, the procedure also determines unknown momentum of the 3–chamber track. The stub–stub vee requires the additional constraint that the vee is originated in the primary vertex.

A special reconstruction routine is implemented to recover lost vees for $\Xi^- \to \Lambda\pi^-$, $\Omega^- \to \Lambda K^-$, and $\Sigma^+ \to p\pi^0$. For these charged modes, the parent particle can leave a track in the SSD that is accidentally linked to one of the vee daughters. The *track–track 1–link* and *track–stub 1–link* vee algorithms are identical to the track–track and track–stub algorithms, respectively, except that one of vee daughter tracks is allowed to be linked (in any case the 5–chamber track is allowed to be linked). A few additional cuts are applied to remove the background of true linked tracks. For the *track–track 1–link* vees the two momenta (using M1 and M2) are required to disagree by at least $5\sigma$ and by at least $3\sigma$ for the *track–stub 1–link* vees ($\sigma$ is an error on the momentum difference). The higher momentum daughter track is required to be identified by Čerenkov detector as being a *heavy* (ISTATP $> 7$). Since a negligible amount of $K_s^0$ falls into this topology, no attempt is made to reconstruct 1–link vees for the $K_s^0$ hypothesis.

### 4.5.4 Reconstruction Vees

Reconstruction vees decay in the region of the spectrometer between P0 and P2. The highest momentum vees tend to be reconstructed in this category because they are more likely to decay downstream of P0.

Since the MWPC tracking algorithm reconstructs only those tracks with hits in P0. Recon vee algorithm first reconstructs candidate vee daughter tracks with unused hits in P1, P2, P3, and P4.

The reconstruction vee search proceeds as follows. The program first looks for vees decaying between P0 and P1, then for vees between P1 and P2. Each program employs the same flow logic. Single track projections are found in the non-bend X-view. The X hits are matched up with U, V, and Y hits to form track candidates and single track fits are performed. At least three hits are required to be found in each chamber. A loose $\chi^2$ cut is made on the single track fits. Finally the oppositely charged tracks are paired to make vee candidates and a least square fit is performed. The vertex position is included in the fit along with the track hits. Candidates with acceptable fits are sent to an arbitration algorithm which insures that no X-projection is used in more than one vee.

The vees which decay between P1 and P2 where the decay tracks exit before passing through P4 are handled separately. These tracks are subjected to an additional constraint that they originate at the primary interaction vertex and the transverse momenta of the tracks about this direction are required to balance.

## 4.6 Kinks

The term *kink* refers to a decay where a long–lived charged particle passes through the SSD and then decays into a charged particle and a neutral particle. The E687 kink algorithm is primarily used to reconstruct these three decays:

$$\begin{aligned}
&\Sigma^+ \longrightarrow p\pi^0 \quad (\mathrm{BR} = 51.6\%), \\
&\Sigma^+ \longrightarrow n\pi^+ \quad (\mathrm{BR} = 48.3\%), \\
&\Sigma^- \longrightarrow n\pi^- \quad (\mathrm{BR} = 100\%),
\end{aligned}$$

The kink algorithm begins by looping over all unlinked SSD tracks pointing into the M1 aperture and pairing each with unlinked MWPC tracks. Vee candidate tracks are not considered as possible kinks. The X–projection of unlinked MWPC tracks are extrapolated upstream to determine whether they intersect with an unlinked

SSD track. This rough estimate of the X and Z position of the intersection is required to be between the last SSD station and the first MWPC station.

If the track passes through both magnets, its momentum is measured by M2, and we can estimate a Y position by tracing the track through the M1 field to the previously determined Z location. If the Z position is upstream of M1, the Y distance between the traced 5–chamber track and the SSD track at this Z position is required to be less than 2.5 cm.

The parent momentum can only be calculated by forming a particular decay hypothesis and solving the kinematic equations. This involves assuming the parent and daughter masses and balancing the momentum transverse to the parent direction. The kinematic equations can only be solved up to a two-fold ambiguity in the parent momentum. If both momenta are physical, they are both recorded for the later analysis. However, if the kink Z position is within the M1 magnetic field, the ambiguity can be resolved.

The MWPC track is traced upstream to the Z position of the kink. This determines the X and Y position of the kink. The SSD track is then traced downstream through the M1 field to the Z position, with different trial momenta, until a momentum is found which best traces the SSD track to the kink vertex.

For 3–chamber MWPC tracks, only kink positions upstream of M1 are accepted. The X and Y positions of the microstrip track at the previously estimated kink Z positions are used for the kink vertex location. The daughter track momentum is then determined by tracing the 3–chamber track through the M1 field upstream to this vertex.

Kinks are reconstructed using all three decay topologies mentioned above. After the kink reconstruction is completed, we can improve the particle identification of the daughter particle by re–running the Čerenkov analysis routine with the momentum determined by the kink algorithm.

## 4.7 $\Xi^-/\Omega^-$ Reconstruction

The $\Xi^-$ and $\Omega^-$ hyperons, called *cascades*, are commonly found in charmed baryon decays. They are crucial in the reconstruction of many charmed baryon signals. The cascades are reconstructed in the E687 PASS1:

$$\Xi^- \longrightarrow \Lambda\pi^- \qquad (\mathrm{BR} = 100\%),$$
$$\Omega^- \longrightarrow \Lambda K^- \qquad (\mathrm{BR} = 67.8\%),$$

Note that both modes contain one $\Lambda$ that has been reconstructed by the vee algorithm. In E687, the cascade decays are classified into two categories: *type–1* (or *upstream*) $\Xi^-$'s and $\Omega^-$'s which decay upstream of the SSD and *type–2* (or *downstream*) *cascades* which decay downstream of the microvertex detector.

Two separate algorithms have been employed to reconstruct the relevant decay topologies [35]. Both algorithms use a common set of requirements to select the $\Lambda$. In all cases, the vee daughter track with a higher momentum is considered a proton and the Čerenkov algorithm is re-run using the momenta of the vee daughter tracks as determined by the vee algorithm. The requirements for each vee type are given below.

- SSD vees:

  1. Mass of the $\Lambda$ must be within 8 MeV/$c^2$ of the nominal $\Lambda$ mass.
  2. Čerenkov requirements for the proton track:
     - ISTATP = 8, 12, or 14 if the momentum ($p$) is less than 20 GeV/$c$;
     - ISTATP = 8 or 12 if 20 GeV/$c < p <$ 110 GeV/$c$;
     - ISTATP = 8, 12, 14, or 15 if 20 GeV/$c < p <$ 110 GeV/$c$.
  3. Neither vee SSD track is allowed to be linked to two MWPC tracks and the pulse height from the silicon strip for each SSD track must be consistent with a single ionizing particle. Both requirements are used to reject $e^+e^-$ tracks.

- MIC vees:

  1. Mass of the $\Lambda$ must be within 8 MeV/$c^2$ of the nominal $\Lambda$ mass.

- Track–Stub and Stub–Stub vees:

  1. Mass of the $\Lambda$ must be within 15 MeV/$c^2$ of the nominal $\Lambda$ mass.
  2. Same Čerenkov requirements for the proton track as in item 2 of SSD vees.
  3. Čerenkov requirements for the pion track:
     - ISTATP $> 1$

- Track–Track vees:

  1. Same requirements as for items 1–3 of Track–Stub and Stub–Stub vees.
  2. Distance of closest approach between vee daughter tracks must be less than 5 mm.

- 1–link and Recon vees:

  1. Mass of the $\Lambda$ must be within 15 MeV/$c^2$ of the nominal $\Lambda$ mass.

The reconstruction efficiency for $\Lambda$'s which originate from $\Xi^-$'s is calculated from a Monte Carlo study. We find that the overall $\Lambda$ reconstruction efficiency is 41 % using the requirements described above.

### 4.7.1 Upstream $\Xi^-/\Omega^-$

Upstream $\Xi^-/\Omega^-$'s are those which decay in the upstream of the first microstrip station. The reconstruction algorithm is rather simple at least, in principle. Linked MWPC tracks are paired with each $\Lambda$ candidate which satisfies the requirements outlined above. The decay vertex of the $\Xi^-/\Omega^-$ candidate is reconstructed by intersecting the $\Lambda$ momentum vector and the MWPC track, demanding the confidence level of the vertex to be greater than 1%, and that the candidate be consistent with coming from a vertex further upstream such as the primary vertex. The MWPC track is assigned a pion mass to obtain the invariant mass for the $\Xi^-$ hypothesis and is assigned a kaon mass for the $\Omega^-$ hypothesis. The candidate is accepted if the $\Lambda\pi^-$ invariant mass is less than 1.4 GeV/$c^2$ or the $\Lambda K^-$ invariant mass is less than 1.725 GeV/$c^2$. Two additional requirements are applied for each candidate in order to improve the signal–to–noise (S/N) ratio.

The *significance of separation* between the $\Xi^-/\Omega^-$ decay vertex and its production vertex is calculated as the quantity $L/\sigma_L$, where $L$ is the distance between two vertices and $\sigma_L$ is the error on $L$. The algorithm requires $L/\sigma_L > 0$.

The *isolation* of the $\Xi^-/\Omega^-$ decay vertex can be tested by attempting to place other tracks in the vertex and re–fitting it. A cleaner sample is obtained by requiring that the highest confidence level (CL2) found during the re–fitting is less than 0.1.

The invariant mass plots for the $\Xi^-$ and $\Omega^-$ hypotheses are shown in Figure 4.6. A cut of $L/\sigma_L > 0$ and CL2 $< 0.1$ is required, along with the requirement that for the $\Omega^-$ hypothesis the daughter track is identified by the Čerenkov counters as being kaon consistent. These plots are from the full E687 data sample.

The reconstruction efficiency of this algorithm has been studied using Monte Carlo simulation and found to be about 20% for both decays without including geometrical acceptance and the branching fractions introduced in the decay modes.

### 4.7.2 Downstream $\Xi^-/\Omega^-$

Downstream $\Xi^-/\Omega^-$'s are reconstructed between the last SSD station and the first MWPC plane of P0. This decay volume consists of more than three meters in the beam direction. A very important advantage to these decays is that the $\Xi^-/\Omega^-$ leaves a track in the SSD before decaying, which will become more apparent in the

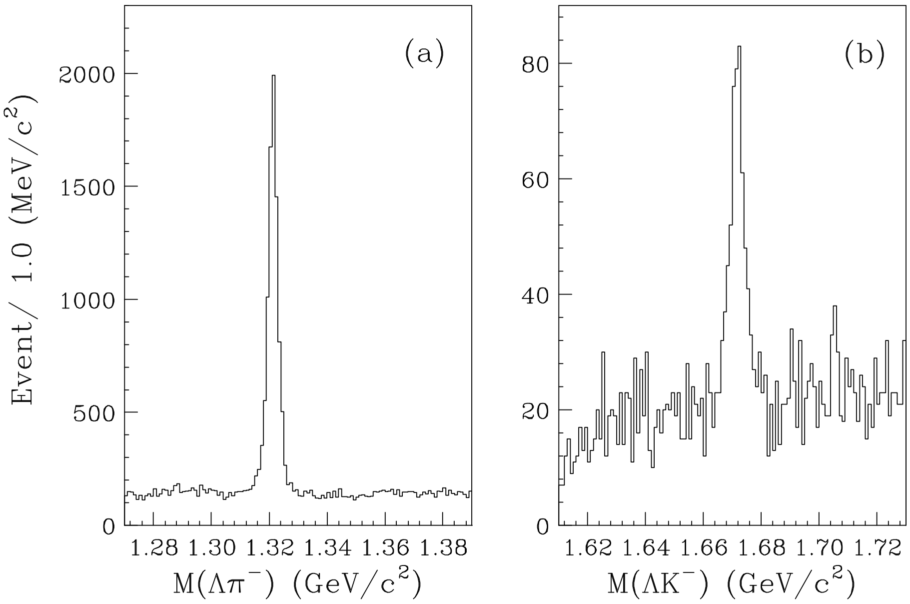


Figure 4.6: $\Lambda\pi^-$ and $\Lambda K^-$ invariant mass distributions for the $\Xi^-$ and $\Omega^-$ candidates decaying upstream of the SSD a) for the $\Xi^-$ candidates and b) $\Omega^-$ candidates.

charmed baryon analysis.

The algorithm begins by pairing each $\Lambda$ with every unlinked MWPC track in a given event. A putative cascade decay vertex is determined by intersecting a $\Lambda$ momentum vector and a charged daughter track. If the vertex is found to be downstream of P0 or more than 50 cm upstream of the target, the combination is rejected. At this point the charged daughter track is traced through M1 to the putative vertex. For a 3–chamber track, 5 times iterative procedure is used to determine its new track parameters until the Z of the vertex changes by less than 3 mm from one iteration of the next. A new vertex Z location is determined as the point where the distance of closest approach of the $\Lambda$ vector and the track occurs. The track is traced to the new vertex and the track parameters are updated.

Unlinked SSD tracks are looped over and an attempt is made to match each one with the vector sum of the $\Lambda$ momentum and the charged MWPC track. If the $\Lambda$ under consideration is of the 1–link category then the SSD track which is linked to one of the $\Lambda$ daughters is also considered in this step. Each SSD track is traced downstream to the putative cascade vertex determined in the previous step; if the vertex is within M1 field the magnetic tracing procedure is employed, else the SSD track is simply extrapolated to the vertex. A better Z position of the vertex is now determined as the Z position where the SSD track and MWPC track make their closest approach because the SSD track has much better position resolution than does the $\Lambda$. If the Z position is located downstream of P0 or upstream of the target, the SSD track is rejected as a candidate. In addition, the $\Xi^-/\Omega^-$ vertex is required to be upstream of $\Lambda$ vertex.

To remove spurious matches a cut is imposed on two quantities. The candidate vertex has been defined in two ways: the space point where a $\Lambda$ and a MWPC track make their closest approach, and the point where an SSD track and the MWPC track make their closest approach. The transverse distance (*i.e.* in the X–Y plane) between these putative vertices is defined as CASIMP and is required to be less than certain value. The second quantity on which a cut is made is the difference between the X and Y slopes of the SSD track and the slopes given by the sum of the $\Lambda$ and MWPC track momentum vectors. The ANGLX and ANGLY, defined as the X slope difference and Y slope difference, respectively, are required to be less than a certain values. Candidates sharing the same $\Lambda$ and MWPC track but using different SSD tracks are arbitrated on the basis of the CASIMP quantity. Monte Carlo studies show that this arbitration is almost 99% efficient. Finally, the MWPC track is assigned a pion mass for the $\Xi^-$ hypothesis and is assigned a kaon mass for the $\Omega^-$ hypothesis. The candidate is accepted if the $\Lambda\pi^-$ invariant mass is less than 1.4 GeV/$c^2$ or the $\Lambda K^-$ invariant mass is less than 1.725 GeV/$c^2$ . The invariant mass plots for the $\Xi^-$ and $\Omega^-$ are shown in Figure 4.7.

The overall reconstruction efficiency has been estimated by Monte Carlo study

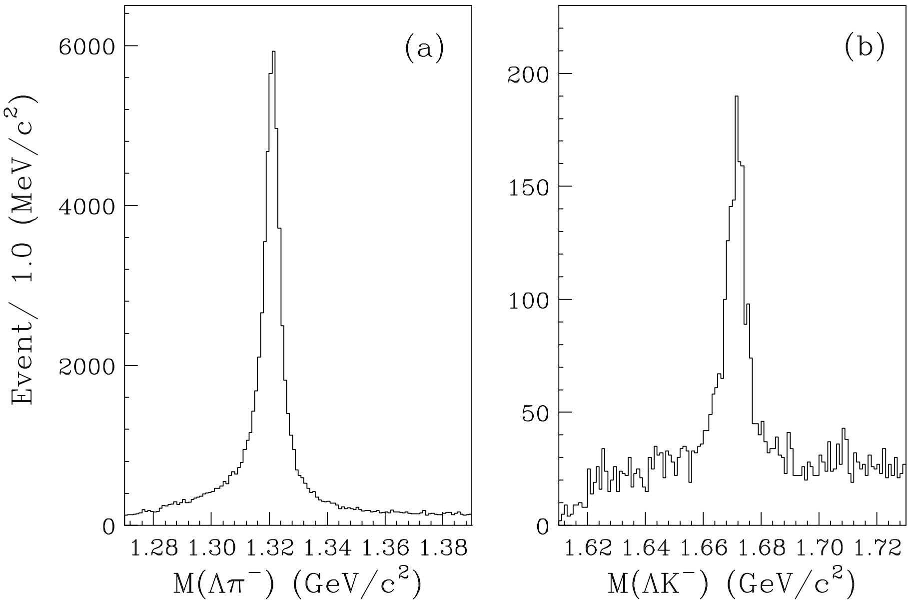


Figure 4.7: $\Lambda\pi^-$ and $\Lambda K^-$ invariant mass distributions for the $\Xi^-$ and $\Omega^-$ candidates decaying downstream of the SSD a) for the $\Xi^-$ candidates and b) $\Omega^-$ candidates.

to be about 20% reflecting the 12% of the $\Xi^-$ and 4.5% of the $\Omega^-$ which are not in the geometrical acceptance of the algorithm (decay downstream of P0).

## 4.8 Data Reduction

The reconstruction algorithms are combined into a single package and the raw data information is processed to produce the reconstructed information described in the preceding sections of this chapter. The data reconstruction process (PASS1) is rather CPU intensive and has been performed during the period from November 1991 to August 1992 using IBM and SGI computer farms at Fermilab. About 1,000 raw 8 mm data tapes have been processed, and approximately 2,000 reconstructed 8 mm tapes were recorded during the processing.

The reconstructed data are further reduced by *skimming*. Tapes were skimmed for interesting events from May 1992 to September 1992. The skimmed data is about 40 % of the full data set. A total of 30 skim sets, as shown in Table 4.3 were used for physics analyses.

In this analysis we have used the cascade skim. It has been carried out at the University of Colorado at Boulder. Events containing at least one successfully reconstructed $\Xi^-$ or $\Omega^-$ were skimmed from the full data set and recorded on 8 mm tape. This data sample consists of about 500,000 events, around 0.1% of the original sample of 520 million raw events.

Table 4.3: List of skimbit sets

| Skim bit | Skim category |
|---|---|
| 1 | Semileptonic skim |
| 2 | 1% of all events |
| 3 | Prescale Unbiased Data |
| 4 | $e^+e^-$ pair trigger |
| 5 | Two Vertex Skim |
| 7 | $\Xi^-/\Omega^-$ skim |
| 8 | $K_S^0$ skim |
| 9 | $D$ meson skim |
| 10 | $D$ skim ($D^*$ flag set) |
| 11 | $D$ skim (Golden Mode flag) |
| 13 | $\Lambda$ skim |
| 14 | Kink ($\Sigma^{\pm}$) skim |
| 15 | Charm baryon skim ($pK+X$) |
| 16 | $\Lambda_C^+ \to pK^-\pi^+$ skim |
| 17 | Leptonic skim |
| 18 | $\mu$ skim for $J/\psi$ |
| 19 | Diffractive skim |
| 20 & 21 | Topological skims |
| 25 | Kaon lepton skim |
| 26 | Kaon ID skim |
| 27 | Kaon linking skim |
| 28 | $\phi$ meson skim |

# Chapter 5

# Analysis Tools

In this chapter, we will describe the analysis tools on which most of E687 physics analyses are based. The vertex finding algorithm used in the reconstruction of charm production and decay vertices is also described. We summarize the salient features of the E687 Monte Carlo, an essential tool for understanding the overall performance of the detector, the reconstruction algorithm and the analysis routines. A detailed study of the lepton (electron or muon) misidentification is discussed as well.

## 5.1 Candidate Driven Vertex Algorithm

A common characteristic of the events containing charm quarks is the presence of separated production and decay vertices. Non-charm hadronic events in E687 contain only one vertex. So, the ability to reconstruct the production and decay vertices and to separate them are essential to isolate the charm signal from the background. The high resolving power of the microstrip detector in E687 makes this separation possible.

In E687 experiment, there are two separate primary, or interaction, vertex finding algorithms. They are the Stand Alone vertexing algorithm and the Candidate Driven vertexing algorithm.

The stand alone algorithm is described in section 4.2. This technique is used to find primary vertices when the charm candidate lacks complete information, i.e. when the charm decay has missing decay daughters such as a $\nu$ or a $\pi^0$, and can not be used as a seed for primary vertex determination. No biases are introduced into initial selection of candidates. The vertexing algorithm commonly used in E687 data analysis is the candidate driven vertex algorithm. The basic idea of the candidate driven vertex algorithm is to use a charm candidate as a seed to find the primary vertex.

### 5.1.1 Vertex Reconstruction

A combination of tracks consistent with a given charm decay mode is selected. The candidate tracks which form the charm particle are then fitted to the hypothesis of a common vertex. If they conform to this hypothesis with a confidence level greater than a specified minimum value, typically 0.01, then the cluster is accepted as a charm candidate. The full covariance matrices of each track comprising the candidate are utilized to generate a charm track.

Once a charm vertex is searched, then the primary vertex is constructed by using the charm track and all other SSD tracks in the event. First, the searched charm track is fitted to a common vertex with all other SSD tracks one at a time. All tracks which form a vertex with the confidence level greater than a cut value (typically 1%) are selected and put into an object list.

The tracks of the list are combined pairwise with the candidate charm track and then are fit to a common vertex hypothesis. The pair with the best confidence level is accepted as a candidate primary vertex. The search terminates when no track is left with the confidence level is greater than a cut value for coming from this vertex.

In addition to fits of the primary and secondary vertices, a global fit is applied to the decay tracks to find the decay length, $L$. The quantity $L/\sigma$, where $\sigma$ is the calculated uncertainty in $L$, is then an unbiased measure of the significance of detachment of the secondary vertex from the primary vertex.

### 5.1.2 Vertex Isolation

Once the primary and decay vertices are reconstructed, an effective way of improving signal to noise is to require the vertices be isolated.

We check whether the charm daughter tracks are compatible with those coming from the primary vertex. The daughter tracks are added one at a time to the primary vertex, then the global fit for the primary vertex is carried out. The highest confidence level (ISO1) of the new object is required to be less than a cut value. This cut is designed to reject an event where one or more tracks from the primary vertex are accidentally assigned to a lower multiplicity charm decay vertex or combined with other tracks to form a fake vertex.

If there are any leftover tracks not assigned to the charm and primary vertices, we check whether any of these leftover tracks are compatible with originating from the secondary vertex. These tracks are added to the charm vertex and the highest confidence level (ISO2) of the new object is required to be less than a cut value. This cut is applied to reduce the backgrounds where we have additional charged tracks in the vertex.

## 5.2 Monte Carlo Simulation

The E687 Monte Carlo simulation is divided into two packages, the event generation package and detector simulation algorithm.

The event is generated by an E687 software package called GENERIC. This set of routines can provide an interface to the LUND package, or the user can choose a simpler mode of event generation for quick studies. The user also choose some of the initial condition as well as the production and decay modes of a particle. The first process simulated in GENERIC is the electron bremsstrahlung in the radiator. Once a photon energy is chosen, the LUND package (Jetset 7.4/Pythia 5.7) [45] is activated to generate $c\overline{c}$ events. The user specified charm particle may be forced to decay according to a fully specified matrix element by the user. The other charmed hadron is allowed to decay according to an approximate matrix element and branching ratio given by GENERIC. Other non-charm particles in the event also decay according to an approximate matrix element and branching ratio given by LUND package.

The ROGUE Monte Carlo package traces an individual particle through the spectrometer. The primary advantage of the ROGUE is that it is extremely fast. The basic philosophy of the ROGUE is to simulate the response of individual detectors using distributions deduced directly from data. In this section, only the IE and the IM simulations are described.

### 5.2.1 IE Simulation

An energy deposition algorithm is used rather than a electromagnetic cascade simulation. In the algorithm energy is deposited longitudinally and transversely based on information from both the calibration runs and showers sampled from the data used in PASS1. The electromagnetic cascades are based on electron calibration data and electrons from $\gamma \longrightarrow e^+e^-$, while the hadronic showers are drawn primarily from pion calibration runs. More detailed description can be found elsewhere [32].

The electron identification efficiency for the MC simulation is higher than for data which suggests a post-hoc efficiency correction is required when comparing modes which have different numbers of electrons in the final state. It is believed that this efficiency discrepancy exceeds 3% [32].

### 5.2.2 Muon Simulation

Simulated muon tracks are scattered through the material in the downstream part of the inner E687 spectrometer. If a track reaches the inner muon system after energy losses and multiple Coulomb scattering, hits are assigned in a detector plane based on the scattered position of the simulated muon track at the detector plane and the efficiency of the counter hit in that plane. The detailed description can be found in reference [33]. The hits from hadrons decaying into muons are added.

The agreement between the actual performance of the muon system and the simulation is good.

## 5.3 Lepton Misidentification

One of the difficulties in the analysis of semileptonic decay is to estimate the amount of background from other decays. In the decay $\Xi_c^0 \longrightarrow \Xi^- l^+ X$, the background contribution from the random correlation of a real $\Xi^-$ with a fake lepton is expected to be large. For instance, in the decay $\Xi_c^0 \longrightarrow \Xi^- \pi^+ \pi^0$, a missing $\pi^0$ can mimic the $\nu$ and the $\pi^+$ can be misidentified as a $\mu^+$. This background is difficult to separate from the signal we want, so we must estimate background contributions accurately.

The lepton misidentification of the pion is studied using a high statistics SSD $K_s^0 \longrightarrow \pi^+\pi^-$ sample. In Figure 5.1 we have fit the invariant and normalized mass distributions of the $K_s^0 \longrightarrow \pi^+\pi^-$ events with a Gaussian and the second order polynomial background. The signal widths of 3.24 MeV/$c^2$ and 0.64 are obtained for Figure 5.1-a) and Figure 5.1-b), respectively.

The selection criteria for the $K_s^0$ sample are:

- The pion candidates must pass through all five chamber stations of the PWC system.
- The pion PWC track must be singly linked to an SSD track.
- No Čerenkov particle identification is required.
- The $L/\sigma$ of $K_s^0$ is required to be greater than 5.

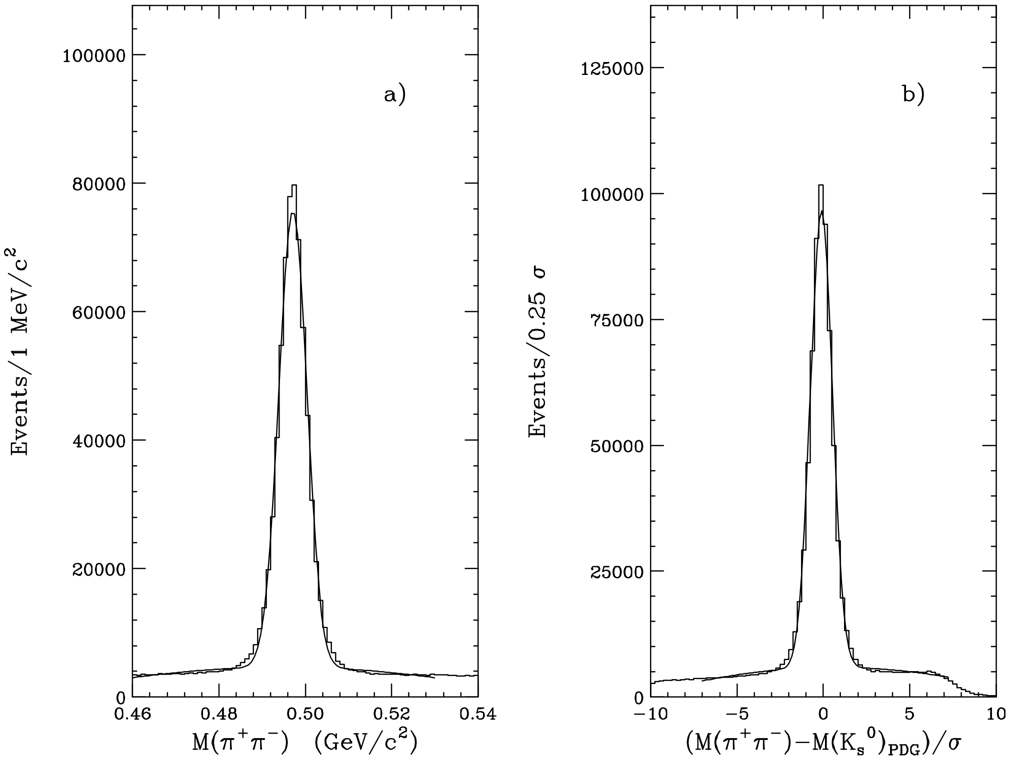


Figure 5.1: The $K_s^0$ mass distributions: a) the $\pi^+\pi^-$ invariant mass distribution of $K_s^0$, and b) the normalized $K_s^0$ mass distribution of $(M(\pi^+\pi^-) - M(K_s^0)_{PDG})/\sigma$.

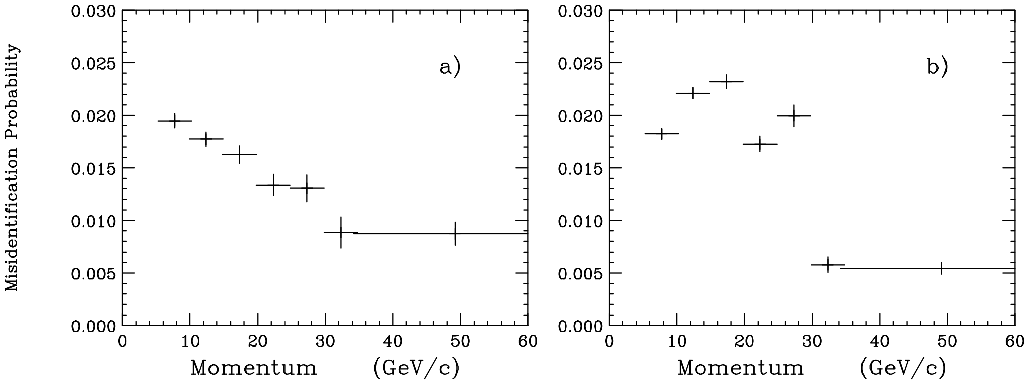


Figure 5.2: The muon misidentification probability of the pions from $K_s^0$ at different momenta a) for 1990 data, b) for 1991 data

- The fit confidence level of the $\pi^+\pi^-$ vertex from the $K_s^0$ is required to be greater than 1%.

Once the candidate $K_s^0$ is selected, we fit $(M(\pi^+\pi^-)-M(K_s^0)_{PDG})/\sigma$, where $\sigma$ is the calculated $K_s^0$ mass error. The momentum dependent misidentification is obtained by using yields from the fit and the following formulae,

$$P = \frac{Events\ with\ idmuon}{total\ events}\ for\ the\ muon\ , and$$

$$P = \frac{Events\ with\ (idelectron\ and\ 0.8\ <\ E/p\ <\ 1.5)}{total\ events}\ for\ the\ electron.$$

The lepton misidentification probabilities are shown in Figure 5.2 for the muon and in Figure 5.3 for the electron. The misidentification probabilities of the muon and electron are comparable to the previous studies [32, 33].

In the uniform 1990 muon system, the misidentification is dominated by random noise and we need only a momentum dependent misidentification probability. But in the 1991 muon configuration the hole in the muon system requires a position dependence as well as a momentum dependence. The $\pi$ tracks of the $K_s^0$ are projected

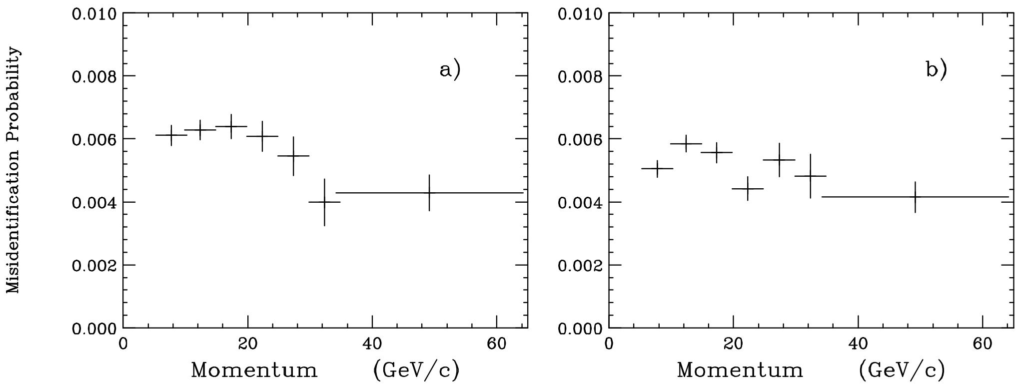


Figure 5.3: The electron misidentification of the pions from $K_s^0$ at different momentum a) for 1990 data, b) for 1991 data

in X and Y at IM1X. There is a significant position dependence in the 1991 system, but not in the 1990 system as shown in Figure 5.4.

The major source of misidentification in the muon system is due to the hadron showers penetrating the absorption material (muon filter). The misidentification from particles that decay into a muon accounts for about 15% of the total pion misidentification.

The proton and kaon misidentification probabilities in the muon system are comparable to the pion misidentification. The detailed studies are described in the reference [33].

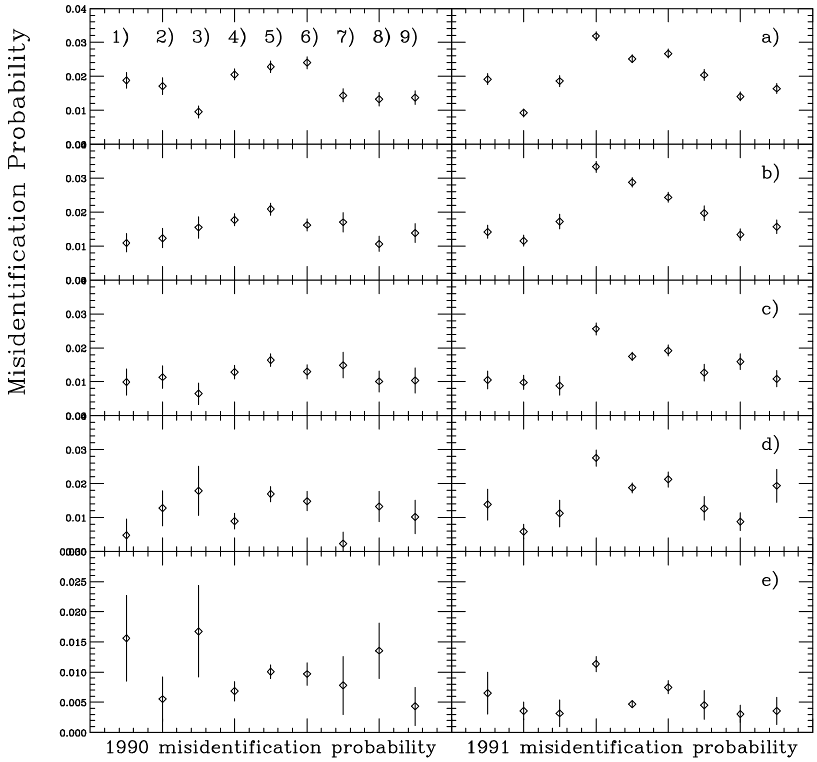


Figure 5.4: The muon misidentification of pions from $K_s^0$, the momentum ranges of a)$10 \sim 15$ GeV/$c$ , b)$15 \sim 20$ GeV/$c$ , c)$20 \sim 25$ GeV/$c$ , d)$25 \sim 30$ GeV/$c$ , e)$> 30$ GeV/$c$ , the position ranges of 1)$X < -20,\ Y < -40$ cm, 2)$-20 < X < 20,\ Y < -40$ cm, 3)$20 < X,\ Y < -40$ cm, 4)$X < -20,\ -40 < Y < 40$ cm, 5)$-20 < X < 20,\ -40 < Y < 40$ cm, 6)$20 < X,\ -40 < Y < 40$ cm, 7)$X < -20,\ Y > 40$ cm, 8)$-20 < X < 20,\ Y > 40$ cm, 9)$20 < X,\ Y > 40$ cm.

# Chapter 6

# $\Xi_c^0$ Semileptonic Decays

The semileptonic decays of the charmed baryon $\Xi_c^0$ to $\Xi^-\mu^+X$ and $\Xi^-e^+X$ are discussed in this chapter. It is difficult to reconstruct the $\Xi_c^0$ baryon partly because of its shorter lifetime and partly because of its lower production rate relative to charmed mesons. We infer the existence of the $\Xi_c^0$ via its point of production and decay products.

As a normalization mode, we analyze $\Xi_c^0 \longrightarrow \Xi^-\pi^+$ decay, and measure the branching ratios of $\Xi_c^0$ semileptonic decays relative to $\Xi_c^0 \longrightarrow \Xi^-\pi^+$.

## 6.1 Event Selection

The analysis is based on the $\Xi^-/\Omega^-$ skim sample of about 500,000 events from the entire 1990-1991 data set. This skim came from the *tiny skim* tapes where any duplicate events have been removed. In this analysis, we have used only the type 2 $\Xi^-$ cascades which have decayed downstream of the silicon microstrip detector (SSD) where the $\Xi^-$ track is reconstructed in the SSD. We have selected a candidate $\Xi_c^0 \longrightarrow \Xi^-l^+X$ decay if the following requirements are met:

- $\Xi^-$ selection

- The daughter $\Lambda$ baryon invariant mass is required to be within $\pm$ 15 MeV/$c^2$ of its world average of 1115.684 MeV/$c^2$ .
- The daughter $\Lambda$ is reconstructed through its decay to $p\pi^-$ and the decay vertex of the $\Lambda$ must be downstream of the $\Xi^-$ decay vertex.
- A cut is made on the difference between the X and Y slopes of the $\Xi^-$ SSD track and the slopes given by the sum of the $\Lambda$ and the Multiwire Proportional Chamber (MPWC) $\pi^-$ track momentum vectors; The ANGLX and ANGLY, defined as the X slope difference and the Y slope difference, respectively, are required to be less than a certain value. For 1-link $\Lambda$'s, tighter cuts of ANGLX, less than 0.001, and ANGLY, less than 0.002, are used. For un-linked $\Lambda$'s, ANGLX, less than 0.004, and ANGLY, less than 0.004, are required.
- The transverse distance between the space point where a $\Lambda$ and a MPWC track make their closest approach and the point where a $\Xi^-$ SSD track and the MPWC track make their closest approach is defined as CASIMP. The CASIMP is required to be less than 1.2 cm.
- The combination with the smallest $\sqrt{ANGLX^2 + ANGLY^2}$ is chosen if there is more than one combination of $\Lambda\pi^-$ matched to the single SSD $\Xi^-$ track.
- Microstrip(*type8*) and SSD(*type9*) $\Lambda$ baryons are explicitly removed from the type 2 $\Xi^-$ sample.

  This set of $\Xi^-$ cuts will be referred to as the *standard* $\Xi^-$ cuts.
- $L/\sigma_L$ is required to be greater than 2.0, where $L$ is the distance between $\Xi^-$ decay vertex and $\Lambda$ decay vertex, and $\sigma_L$ is the error on $L$.

The $\Lambda\pi^-$ invariant mass plot for the $\Xi^-$ candidates decaying downstream of the SSD is shown in Figure 6.1. The distributions are fitted to the Gaussian

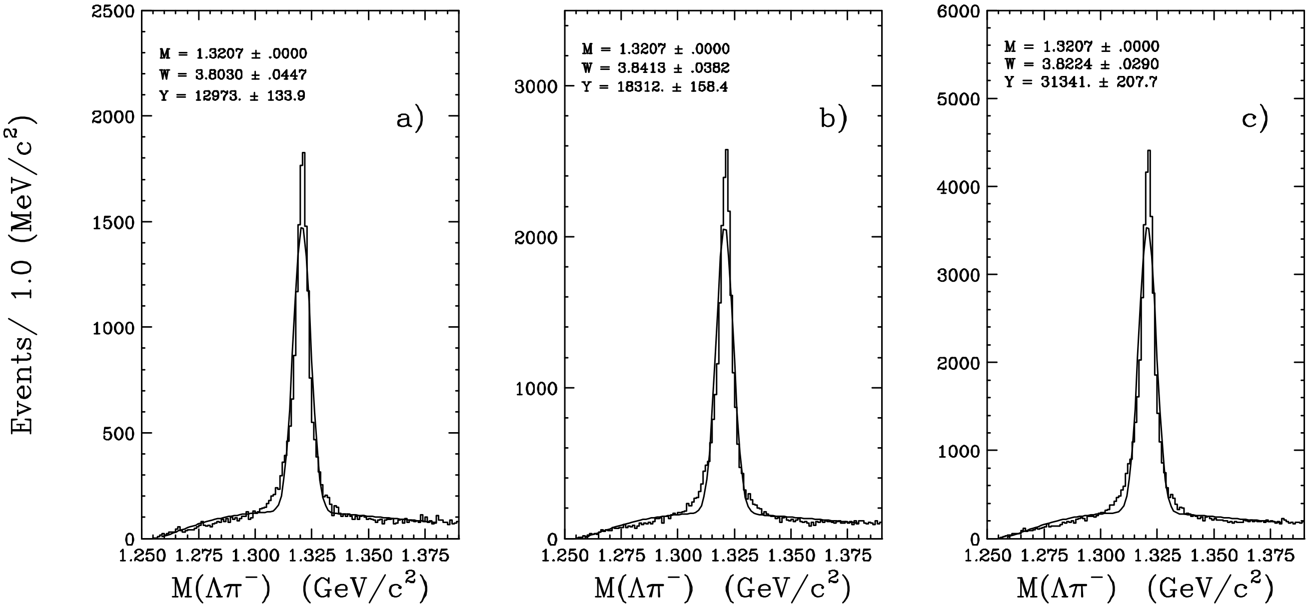


Figure 6.1: The $\Lambda\pi^-$ invariant mass distributions for the $\Xi^-$ candidates decaying downstream of the SSD: a) for the 1990 data, b) for the 1991 data, c) for the combined 1990 and 1991 data.

signal with the background function

$$A(M - m_{thresh})^B exp[-C(M - m_{thresh})] \tag{6.1}$$

where $m_{thresh}$ is the mass sum of $\Lambda$ and $\pi$, and A, B, and C are free parameters in a maximum binned likelihood fit to the data.

- The muon candidate must pass through all five MWPC stations and must be identified by the inner muon system as a muon. For the muon analysis, only good muon runs [33] were used.

- The electron candidate must pass through all five chamber stations of the MWPC system and must be identified by the inner electromagnetic calorimeter (IE) as an electron. The E/p ratio of the candidate electron is required to be between 0.8 and 1.5, where E denotes the energy deposited in the IE and p is the momentum of the track.

- A lepton(muon or electron) MPWC track must be singly linked to an SSD track. The doubly linked tracks have larger background contributions and a potential to be from $e^+e^-$ production in the electron mode.

- A 10 GeV/$c$ momentum cut is applied to lepton candidates in both 1990 and 1991 runs. This cut is used to reduce contamination from misidentification (mostly from pion decays and noise) and to avoid the region of uncertainty in the identification probability.

Once the candidate tracks are selected, the $\Xi^-$ and lepton microstrip tracks are fitted to determine whether these two particles belong to a common vertex, the charm decay vertex. We have required the confidence level (CLD) for this hypothesis to be greater than 1%. The charm decay vertex is required to be upstream of the trigger counter, TR1.

We form a mass using four momenta of the candidate tracks and require the mass to be less than 2.45 GeV/$c^2$. This mass cut removes most of the $\Xi_c^0 \longrightarrow \Xi^-\pi^+$ contamination.

Once the charm decay vertex is constructed, we have to reconstruct the production vertex of the charm in order to measure the significance of separation between the production and decay vertices.

The stand alone vertex algorithm (DVFREE) found in the target volume with the highest multiplicity is chosen as the production vertex, and the largest $L/\sigma$ vertex is selected if there is more than one vertex found with the same highest multiplicity. The production vertex confidence level (CLP) is required to be greater than 1%.

If there are any leftover tracks not assigned to the charm and primary vertices, we check whether any of these leftover tracks are compatible with originating from the charm vertex. These tracks are added to the charm vertex and the highest confidence level (ISO2) is required to be less than 0.0001.

## 6.2 Invariant Mass of $\Lambda\pi^-$

The $\Lambda\pi^-$ invariant mass for both the right sign(e.g.$\Xi^- l^+$) and wrong sign(e.g. $\Xi^- l^-$) $\Xi\mu$ pairs are shown in Figure 6.2, and $\Xi e$ pairs in Figure 6.3.

There appears to be an excess of the right sign $\Xi^-$ baryon compared to the wrong sign $\Xi^-$ for both the muon and electron modes. The distributions are fitted to a Gaussian signal with the background function in the Eq (6.1) using a maximum binned likelihood method. The signal width is fixed at 4.0 MeV/$c^2$ as determined by the Monte Carlo simulation. The fit results for each mode are listed in Table 6.1.

From the fit to the $\Lambda\pi^-$ distributions at $L/\sigma\ > 0.5$, we have obtained $38.5 \pm 11.0$ and $14.7 \pm 7.7$ excess events of the right sign $\Xi^-$ baryon compared to the wrong sign $\Xi^-$ for the muon and the electron mode, respectively.

In order to check any bias in the fixing of the signal width in the fit, the distributions are re-fit without fixing the signal width. The fit results with free signal width for each mode are listed in Table 6.2. The signal widths of $4.30 \pm 0.50$ MeV/$c^2$ and $4.69 \pm 0.93$ MeV/$c^2$ are obtained for the right sign and the wrong sign muon mode, respectively. For the electron mode, the signal widths of $3.92 \pm 0.66$ MeV/$c^2$ and $3.38 \pm 1.13$ MeV/$c^2$ are obtained for the right sign and the wrong sign, respectively. The distributions of $\Lambda\pi^-$ for each mode are again fitted with fixing the signal width at 3.82 MeV/$c^2$ as obtained from Figure 6.1. The fit results for each mode are listed in Table 6.3.

From the fit results, we do not notice any fitting bias by fixing the signal width of 4.0 MeV/$c^2$ .

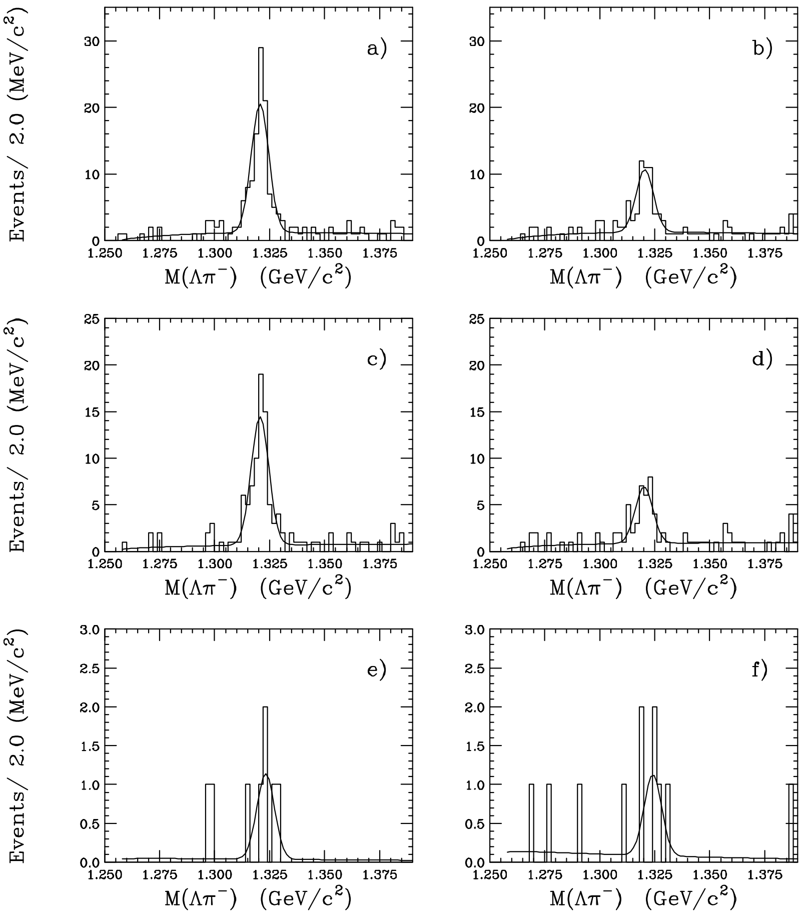


Figure 6.2: The $\Lambda\pi^-$ invariant mass distributions for $\Xi_c^0 \longrightarrow \Xi^-\mu^+X$ decay at different $L/\sigma$ requirements: (a) Right Sign and (b) Wrong Sign for $L/\sigma > 0.0$, (c) Right Sign and (d) Wrong Sign for $L/\sigma > 0.5$, and (e) Right Sign and (f) Wrong Sign for $L/\sigma > 4.0$.

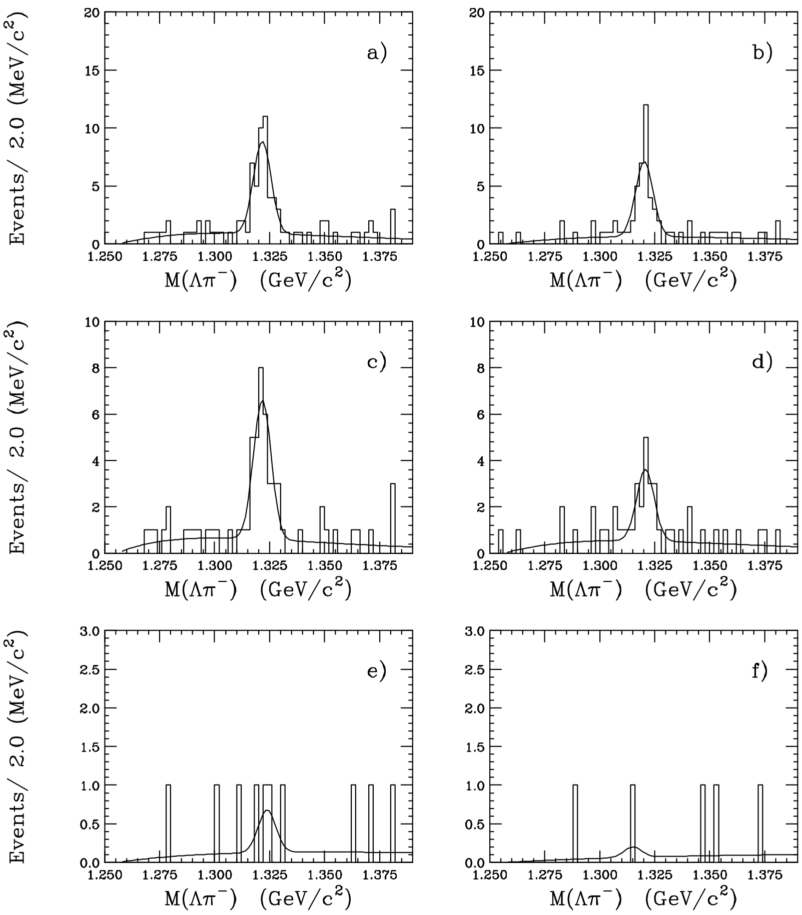


Figure 6.3: The $\Lambda\pi^-$ invariant mass distributions for $\Xi_c^0 \longrightarrow \Xi^- e^+ X$ decay at different $L/\sigma$ requirements: (a) Right Sign and (b) Wrong Sign for $L/\sigma > 0.0$, (c) Right Sign and (d) Wrong Sign for $L/\sigma > 0.5$, and (e) Right Sign and (f) Wrong Sign for $L/\sigma > 4.0$.

Table 6.1: Results from $\Lambda\pi^-$ distributions for the $\Xi^- l^+ X$ decay modes in Figure 6.2 and in Figure 6.3, where errors are only statistical errors.

| Decay modes | $L/\sigma$ | Right Sign(RS) | Wrong Sign(WS) | $RS - WS$ |
|---|---|---|---|---|
| $\Xi_c^0 \longrightarrow \Xi^- \mu^+ X$ | $> 0.0$ | 96.8 $\pm$ 10.7 | 47.1 $\pm$ 8.0 | 49.7 $\pm$ 13.3 |
| | $> 0.5$ | 69.0 $\pm$ 8.9 | 30.4 $\pm$ 6.5 | 38.5 $\pm$ 11.0 |
| | $> 4.0$ | 5.5 $\pm$ 2.5 | 5.2 $\pm$ 2.5 | 0.3 $\pm$ 3.5 |
| $\Xi_c^0 \longrightarrow \Xi^- e^+ X$ | $> 0.0$ | 40.0 $\pm$ 7.1 | 32.5 $\pm$ 6.2 | 7.5 $\pm$ 9.4 |
| | $> 0.5$ | 30.2 $\pm$ 6.1 | 15.5 $\pm$ 4.6 | 14.7 $\pm$ 7.7 |
| | $> 4.0$ | 2.8 $\pm$ 2.0 | 0.7 $\pm$ 1.0 | 2.1 $\pm$ 2.3 |

Table 6.2: Fit results from $\Lambda\pi^-$ distributions with a free signal width for the $\Xi^- l^+ X$ decay modes, where errors are only statistical errors.

| Decay modes | $L/\sigma$ | Right Sign(RS) | Wrong Sign(WS) | $RS - WS$ |
|---|---|---|---|---|
| $\Xi_c^0 \longrightarrow \Xi^- \mu^+ X$ | $> 0.0$ | 95.4 $\pm$ 11.1 | 49.0 $\pm$ 8.9 | 46.4 $\pm$ 14.2 |
| | $> 0.5$ | 70.3 $\pm$ 9.0 | 32.5 $\pm$ 7.1 | 37.8 $\pm$ 11.5 |
| | $> 4.0$ | 5.6 $\pm$ 2.5 | 5.7 $\pm$ 2.8 | -0.1 $\pm$ 3.7 |
| $\Xi_c^0 \longrightarrow \Xi^- e^+ X$ | $> 0.0$ | 39.4 $\pm$ 7.2 | 30.4 $\pm$ 6.3 | 9.0 $\pm$ 9.6 |
| | $> 0.5$ | 30.1 $\pm$ 6.2 | 14.7 $\pm$ 4.7 | 15.3 $\pm$ 7.8 |
| | $> 4.0$ | 2.8 $\pm$ 2.1 | 0.8 $\pm$ 1.0 | 2.0 $\pm$ 2.3 |

Table 6.3: The fit results from $\Lambda\pi^-$ distributions with fixing the signal width at 3.82 MeV/$c^2$ as obtained from Figure 6.1 for the $\Xi^- l^+ X$ decay mode, where errors are only statistical errors.

| Decay modes | $L/\sigma$ | Right Sign(RS) | Wrong Sign(WS) | $RS - WS$ |
|---|---|---|---|---|
| $\Xi_c^0 \longrightarrow \Xi^- \mu^+ X$ | $> 0.0$ | $95.7 \pm 10.6$ | $49.2 \pm 7.9$ | $49.5 \pm 13.3$ |
| | $> 0.5$ | $68.1 \pm 8.9$ | $29.8 \pm 6.4$ | $38.4 \pm 11.0$ |
| | $> 4.0$ | $5.5 \pm 2.5$ | $5.2 \pm 2.5$ | $0.3 \pm 3.5$ |
| $\Xi_c^0 \longrightarrow \Xi^- e^+ X$ | $> 0.0$ | $39.5 \pm 7.0$ | $32.2 \pm 6.2$ | $7.4 \pm 9.4$ |
| | $> 0.5$ | $29.9 \pm 6.1$ | $15.3 \pm 4.5$ | $14.6 \pm 7.6$ |
| | $> 4.0$ | $2.7 \pm 2.0$ | $0.7 \pm 1.0$ | $2.0 \pm 2.3$ |

## 6.3 Background Issues

Detailed sources of backgrounds are now to be considered. The first source of background considered is a real lepton with a fake $\Xi^-$, which may come from a real/fake $\Lambda$ with a fake/real pion. This background is essentially eliminated by fitting for the $\Xi^-$ in the $\Lambda\pi^-$ mass plot. This background can still adversely affect the results if an incorrect fitting function is used.

The second background source is due to the random correlation of a real $\Xi^-$ with a real lepton, each from a separate source. This background contributes approximately equal numbers to the right and wrong sign combinations.

The source of third background is the random combination of a real $\Xi^-$ with a fake lepton. We analyze both the right sign and wrong sign $\Xi^- h^+$ pairs as in the $\Xi_c^0 \longrightarrow \Xi^- l^+ X$ analysis without the lepton identification. The study of the lepton misidentification of the hadron is described in section 5.3.

We assume that the $h^+$ charged particle is a pion because most charged particles are pions in this experiment. The $\Xi^- h^+$ events are weighted according to

Table 6.4: The fit results from $\Lambda\pi^-$ distributions for the $\Xi^- l^+ X$(fake lepton) decay modes at different $L/\sigma$ requirements, where errors are only statistical errors.

| Decay modes | $L/\sigma$ | Right Sign | Wrong Sign |
|---|---|---|---|
| | $> 0.0$ | $66.6 \pm 8.9$ | $49.1 \pm 7.7$ |
| $\Xi_c^0 \longrightarrow \Xi^- \mu^+ X$(fake muon) | $> 0.5$ | $46.4 \pm 7.4$ | $33.5 \pm 6.3$ |
| | $> 4.0$ | $2.6 \pm 1.8$ | $2.0 \pm 1.6$ |
| | $> 0.0$ | $27.7 \pm 5.7$ | $19.5 \pm 4.9$ |
| $\Xi_c^0 \longrightarrow \Xi^- e^+ X$(fake electron) | $> 0.5$ | $19.3 \pm 4.8$ | $13.5 \pm 4.0$ |
| | $> 4.0$ | $1.2 \pm 1.2$ | $0.8 \pm 1.0$ |

the momentum dependent misidentification probabilities except for the 1991 muon analysis. For the 1991 muon analysis, the $\Xi^- h^+$ events are weighted according to the position and momentum dependent misidentification probabilities. The $\Lambda\pi^-$ invariant mass for both the right sign and wrong sign random combinations of a real $\Xi^-$ with a fake lepton are shown in Figure 6.4 for the muon decay mode and in Figure 6.5 for the electron decay mode.

The distributions are fitted to a Gaussian signal with a background function in the Eq (6.1) using a maximum binned likelihood method. The signal width is fixed at 4.0 MeV/$c^2$ . The fit results for each mode are listed in Table 6.4.

The study indicates that the estimated wrong sign pairs from a real $\Xi^-$ and a fake lepton, a misidentified one, is equal to the number of wrong sign $\Xi l$ pairs within statistical error. We can conclude that the background from the random combination of a real $\Xi^-$ and a fake lepton is the largest source of contamination in this analysis, and the background from the random correlation of a real $\Xi^-$ with a real lepton, each from a separate source, is negligible.

There are $12.9 \pm 9.6$ and $6.8 \pm 6.2$ right sign excess events to wrong sign events

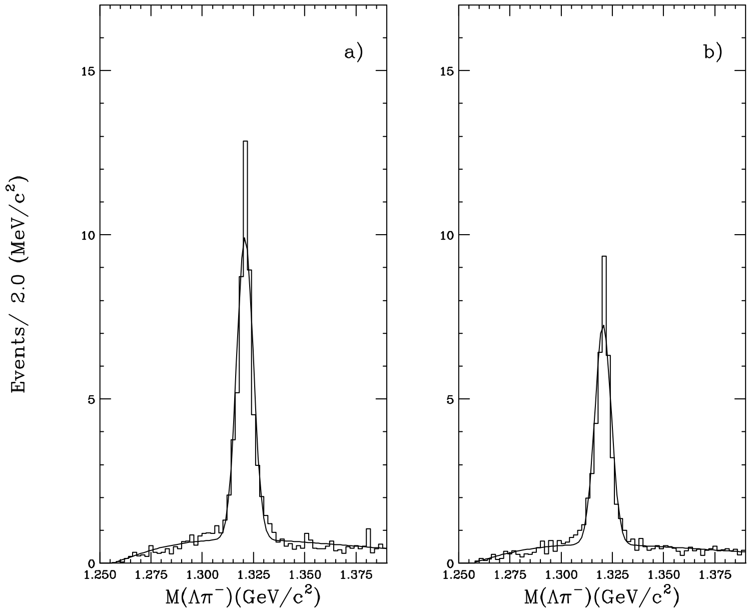


Figure 6.4: The $\Lambda\pi^-$ invariant mass distributions for a real $\Xi$ with a fake muon at $L/\sigma > 0.5$: (a) for the right sign, (b) for the wrong sign.

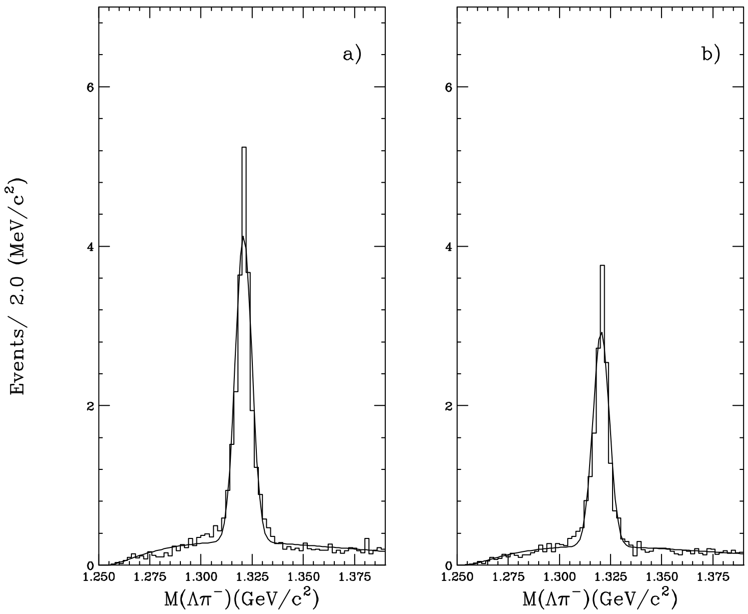


Figure 6.5: The $\Lambda\pi^-$ invariant mass distributions for a real $\Xi$ with a fake electron at $L/\sigma > 0.5$: (a) for the right sign, (b) for the wrong sign.

for the muon and the electron mode, respectively in the background estimation at $L/\sigma > 0.5$. This excess of right sign events over wrong sign events can be explained by the difference in the production rate of the right sign and the wrong sign in the experiment. The production difference comes partly from the presence of $\Xi(1530)^0 \longrightarrow \Xi^-\pi^+$ and partly from other charm baryon hadronic decays.

The $\Xi(1530)^0 \longrightarrow \Xi^-\pi^+$ in the $\Xi^-\pi^+$ sample, where pion is misidentified as a lepton, is considered. Figure 6.6 shows the $\Xi\pi$ invariant masses for both the right sign and wrong sign random combinations of a real $\Xi^-$ with a fake lepton. The study shows that about 3 events in the right sign excess, 5 right sign events and 2 wrong sign events, are explained with the presence of $\Xi(1530)^0$ in the sample. This contribution could be eliminated by removing all $\Xi^-\pi^+$ events from subsequent analysis that are within $3.0\sigma(\sim 8\ \mathrm{MeV}/c^2\ )$ of $\Xi(1530)^0$. No such cut, however, is applied to remove $\Xi(1530)^0$ throughout this analysis because this would significantly reduce the signal yield.

The final source of backgrounds is the contribution from other charm baryon semileptonic decays to the right sign signal. The decay of $\Xi_c^+ \longrightarrow \Xi^-\pi^+l^+\nu$ is analyzed by looking for an excess of the right sign, $\Xi^-\pi^+l^+$ events over the wrong sign $\Xi^-\pi^+l^-$ events, but no excess is observed in this mode. The resonant decay of $\Xi_c^+ \longrightarrow \Xi(1530)^0l^+\nu$ is examined by looking at an excess of the $\Xi(1530)^0$ signal for the right sign combination, $\Xi(1530)^0l^+$ to the wrong sign combination, $\Xi(1530)^0l^-$. The $\Xi^-\pi^+$ invariant masses for both the right sign and wrong sign $\Xi(1530)^0l^+$ pairs are shown in Figure 6.7. No right sign excess is noticed.

The $\Lambda_c^+$ semileptonic decay mode with $\Xi^-$, $\Lambda_c^+ \longrightarrow \Xi^-K^+l^+\nu$ mode was studied by looking for an excess of the $\Xi^-$ for the right sign combination to the wrong sign combination with a visible mass less than the $\Lambda_c^+$ mass. None of the right sign of $\Xi Kl$ combination passed cuts. Also the $\Omega_c^0 \longrightarrow \Omega^-l^+\nu$ decay was analyzed by looking at the $\Omega$ for the right sign combination, $\Omega^-l^+$ using loose cuts, but no right sign $\Omega l$ pair survived. We assume that the background contributions from these charm semileptonic decay modes are negligible.

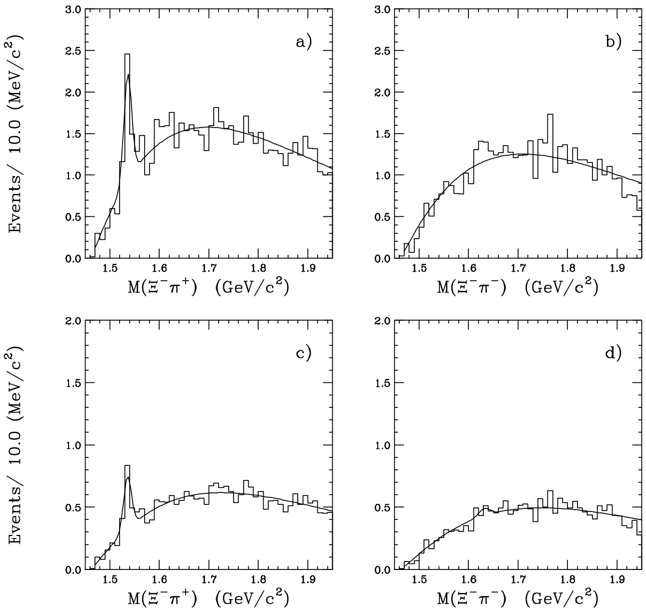


Figure 6.6: The $\Xi^-\pi^+$ invariant mass distributions for a real $\Xi$ with a fake lepton at $L/\sigma > 0.5$: (a) for the right sign and (b) wrong sign in the muon mode, and (c) for the right sign and (d) wrong sign in the electron mode.

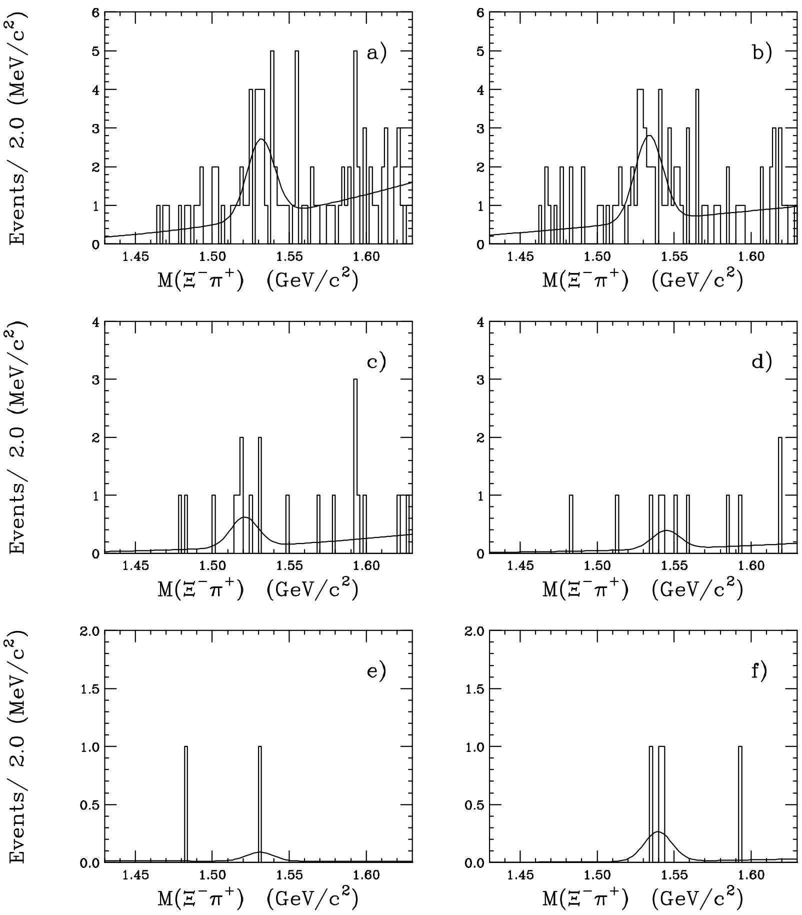


Figure 6.7: The $\Xi^-\pi^+$ invariant mass distributions for $\Xi_c^+ \longrightarrow \Xi(1530)^0 l^+ X$ decay at different $L/\sigma$ requirements: (a) Right Sign and (b) Wrong Sign for $L/\sigma > 0.0$, (c) Right Sign and (d) Wrong Sign for $L/\sigma > 2.0$, and (e) Right Sign and (f) Wrong Sign for $L/\sigma > 4.0$.

The equality of wrong sign pairs estimated from the source of the fake leptons with wrong sign $\Xi l$ pairs indicates that most of the wrong sign $\Xi l$ pairs can be explained by the random combination of a real $\Xi^-$ with a fake lepton, and we use the right sign background of the fake lepton as a quantitative estimate of all sources of misidentified lepton background which contribute to the right sign signal. The $\Xi_c^0 \longrightarrow \Xi^- l^+ X$ semileptonic signal is obtained by subtracting the right sign background contribution from the fitted right sign signal. After this subtraction we obtained $22.6 \pm 11.6$ signal events and $10.8 \pm 7.9$ signal events for the muonic and the electronic mode, respectively at $L/\sigma > 0.5$.

## 6.4 Visible Mass Distribution

The $\Xi l$ invariant masses of both the right and wrong sign events are plotted in Figure 6.8 for the muon mode and in Figure 6.9 for the electron mode after performing the $\Xi^-$ sideband subtraction. The invariant mass of $\Xi^-$ is required to be within $\pm$ 10 MeV/$c^2$ around its world average of 1321.32 MeV/$c^2$ [20]. The sideband of $\Xi^-$ is approximated as a linear shape and chosen $\pm$ 20 MeV/$c^2$ (about $5\sigma$) away from the nominal mass of $\Xi^-$ with 10 MeV/$c^2$ width.

Figure 6.10 and Figure 6.11 show the the $\Xi l$ invariant mass distributions of both the right sign and wrong sign combinations for the muon and the electron mode, respectively after the $\Xi^-$ sideband and background from a fake lepton are subtracted.

The Monte Carlo visible mass distributions of various $\Xi_c^0$ semileptonic decays are shown in Figure 6.12.

## 6.5 Fitting Signal

The data is fitted using a binned maximum likelihood fitting technique for extraction of the amount of the $\Xi^- l^+ X$ signals. The likelihood function is constructed as:

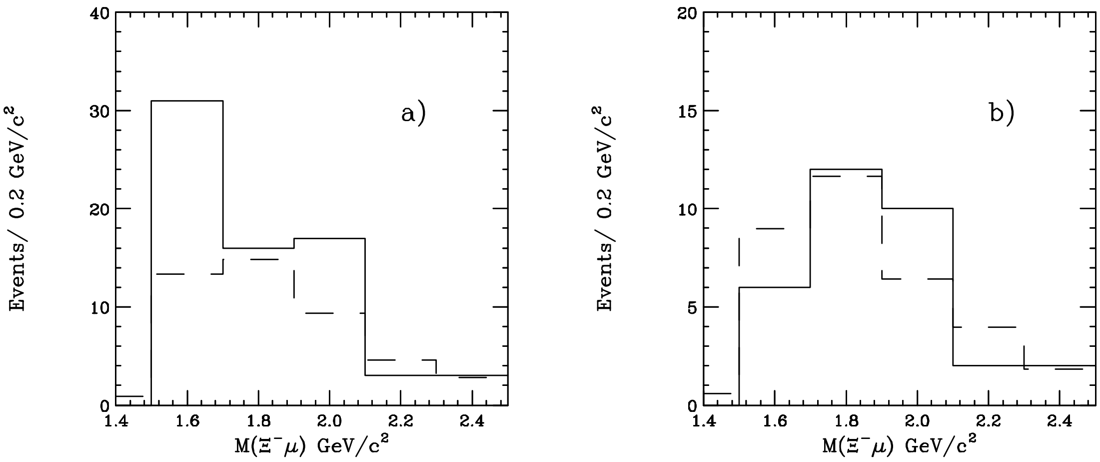


Figure 6.8: The M($\Xi\mu$) distributions after $\Xi^-$ sideband subtraction. The M($\Xi\mu$) distributions, where the muon is a fake are overlaid as a dashed line: a) for the right sign, b) for the wrong sign.

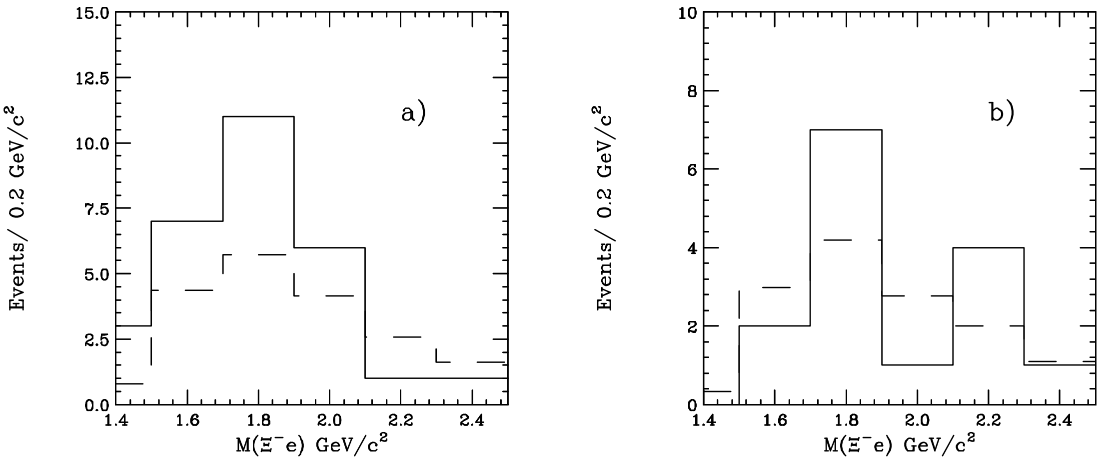


Figure 6.9: The M($\Xi e$) distributions after $\Xi^-$ sideband subtracted. The M($\Xi e$) distributions, where electron is a fake are overlaid as a dashed line: a) for the right sign, b) for the wrong sign.

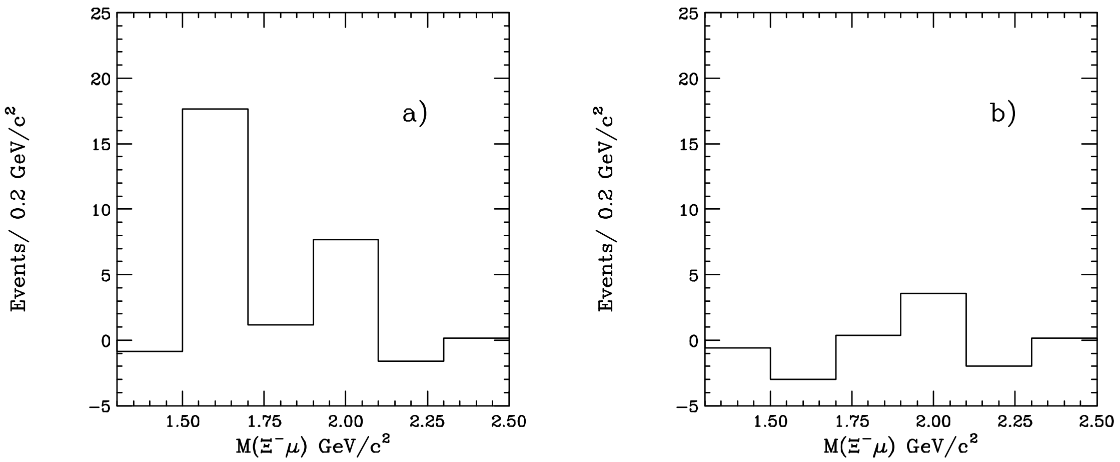


Figure 6.10: The M($\Xi\mu$) distribution after the $\Xi^-$ sideband and the background from a fake muon are subtracted: a) for the right sign, b) for the wrong sign.

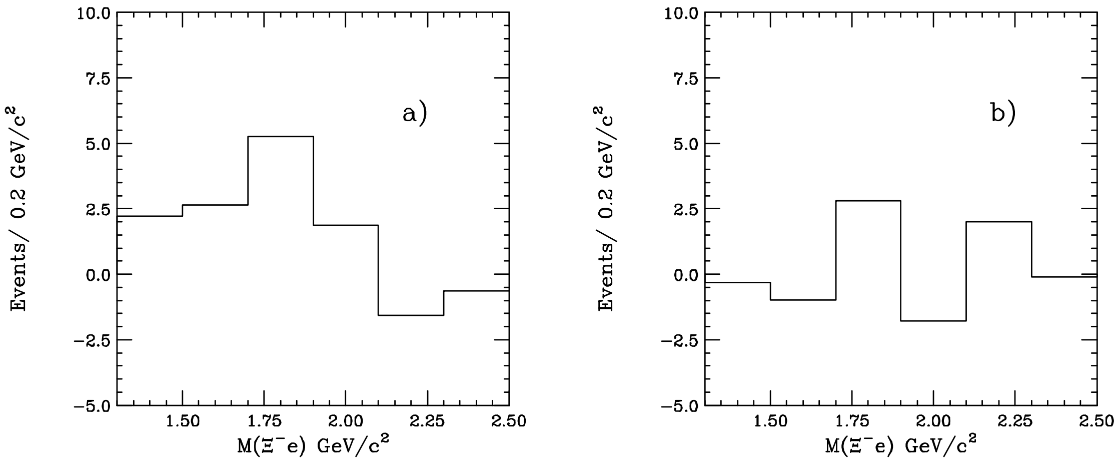


Figure 6.11: The M($\Xi e$) distribution after the $\Xi^-$ sideband and the background from a fake electron are subtracted: a) for the right sign, b) for the wrong sign.

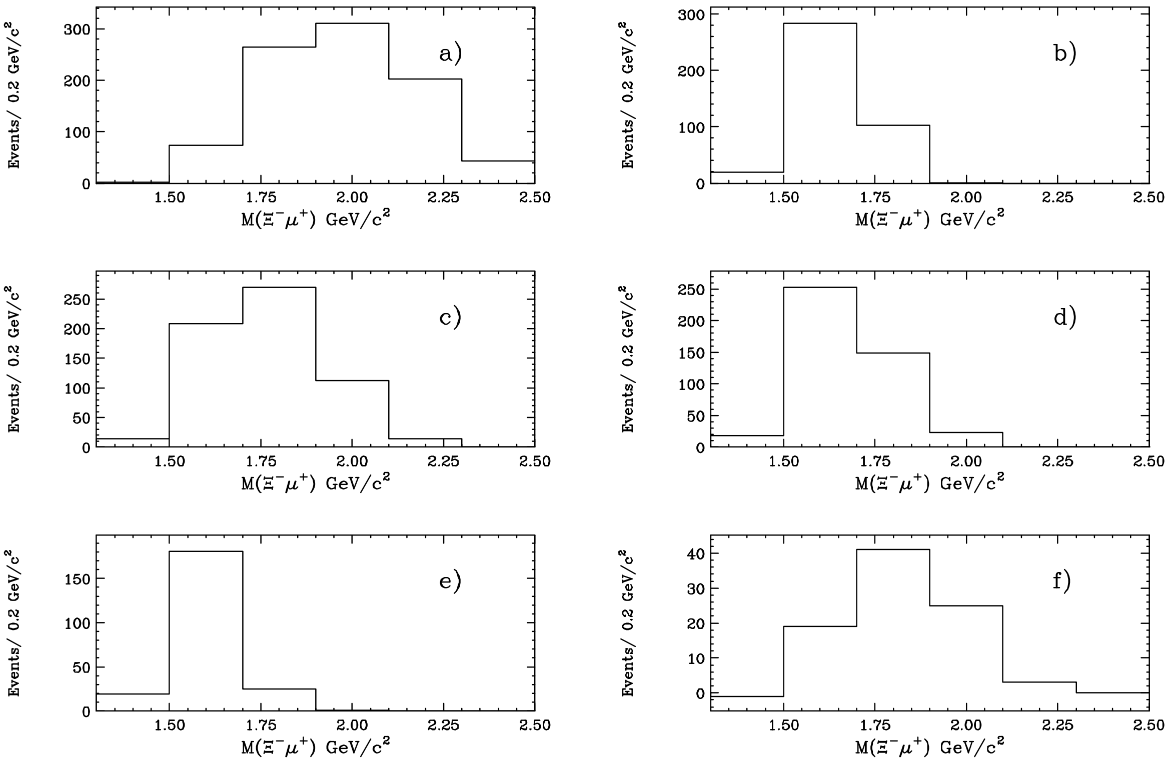


Figure 6.12: The expected M($\Xi\mu$) distributions from the Monte Carlo for different decays: a) $\Xi_c^0 \rightarrow \Xi^-\mu^+\nu$, b) $\Xi_c^0 \rightarrow \Xi^-\eta^0\mu^+\nu$, c) $\Xi_c^0 \rightarrow \Xi^-\pi^0\mu^+\nu$, d) $\Xi_c^0 \rightarrow \Xi^-2\pi^0\mu^+\nu$, e) $\Xi_c^0 \rightarrow \Xi^-3\pi^0\mu^+\nu$, and f) $\Xi_c^0 \rightarrow \Xi^{*-}\mu^+\nu$.

$$\mathcal{L} = \prod_{i=1}^{\#bins} \frac{n_i^{s_i} e^{-n_i}}{s_i!} \tag{6.2}$$

where

$s_i$ = number of right sign events in the $i$th bin of the data histogram
$n_i$ = expected number of events in the $i$th bin of the fit histogram

The likelihood is the product over all bins of the Poisson probabilities of observed $s_i$ entries in bin $i$ when the expected number of entries is $n_i$.

The fit histogram is constructed using our knowledge of the decay process involved; the shape of the $\Xi_c^0 \longrightarrow \Xi^- l^+ \nu$, $\Xi_c^0 \longrightarrow \Xi^-(n)\pi^0 l^+ \nu$ signals from Monte Carlo, and the level of the right sign random combination background described in the previous section:

$$n_i = Y_{\Xi^- l^+ \nu} S_{1i} \ + \ Y_{\Xi^-(n)\pi^0 l^+ \nu} S_{2i} \ + \ M_i \tag{6.3}$$

where

Y denotes the signal yield;
$S_{ji}$ is the fraction of Monte Carlo events in bin $i$ for the $j$ decay mode
(for each fixed $j$; $\Sigma S_{ji} = 1$);
$M_i$ is the number of right sign background events in bin $i$ from lepton misidentification ($\Sigma M_i \neq 1$).

The components of the $\Xi^- l^+ X$ fit are shown in Figure 6.13 for the muon mode, and in Figure 6.14 for the electron mode.

The fit results for each mode are listed in Table 6.5. The values of the $\chi^2$/D.O.F. returned by the fit are 3.39 and 2.57 for the muon mode and the electron mode, respectively.

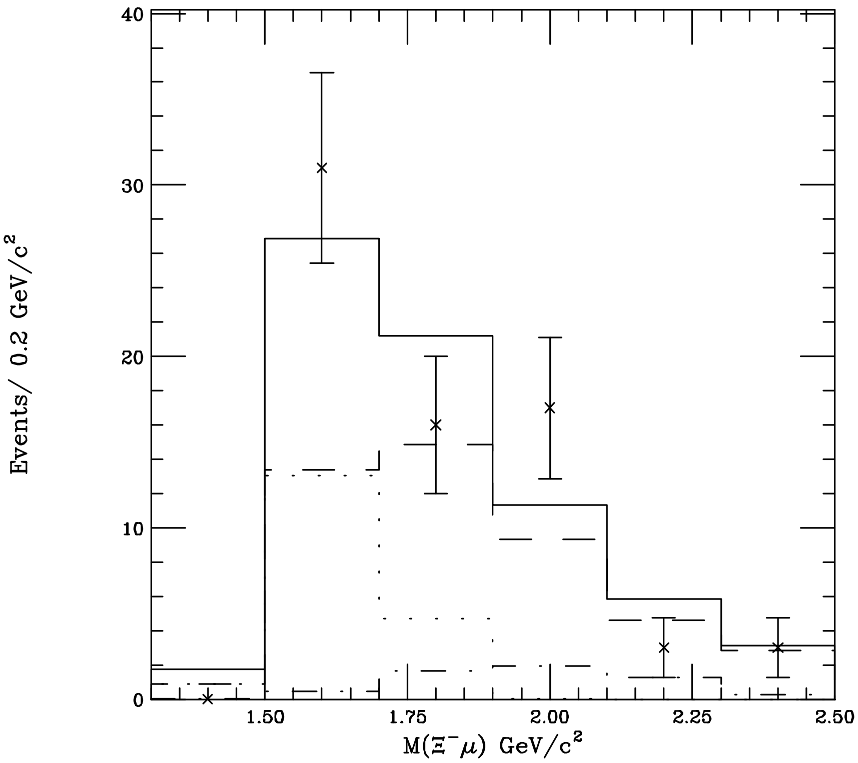


Figure 6.13: The components of the $\Xi^-\mu^+X$ fit. Data points are indicated by crosses, the fit by a solid line. The background from muon misidentification is overlaid as a dashed line, the $\Xi^-\mu^+\nu$ component is indicated by a dot-dashed line, and the $\Xi^-(n)\pi^0\mu^+\nu$ by a dotted line.

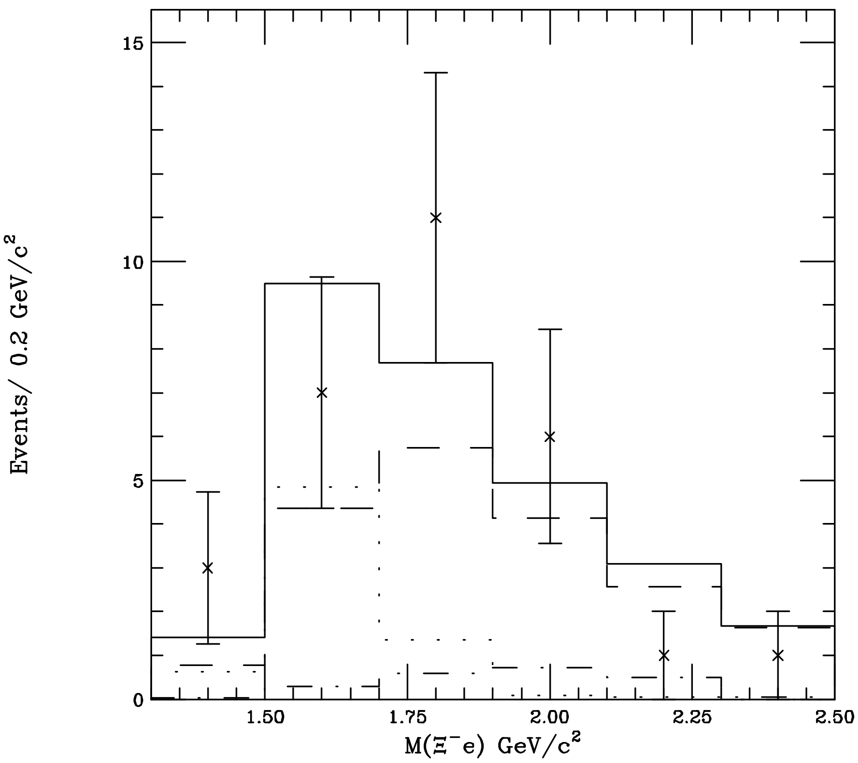


Figure 6.14: The components of the $\Xi^- e^+ X$ fit. Data points are indicated by crosses, the fit by a solid line. The background from electron misidentification is overlaid as a dashed line, the $\Xi^- e^+ \nu$ component is indicated by a dot-dashed line, and the $\Xi^-(n)\pi^0 e^+ \nu$ by a dotted line.

Table 6.5: The fit results for the $\Xi^- \mu^+ X$ mode in Figure 6.13 and for the $\Xi^- e^+ X$ mode in Figure 6.14, where errors are only statistical errors.

| Decay modes | Fit Yield |
|---|---|
| $\Xi_c^0 \longrightarrow \Xi^- \mu^+ \nu$ | $5.6 \pm 6.4$ |
| $\Xi_c^0 \longrightarrow \Xi^- (n)\pi^0 \mu^+ \nu$ | $18.7 \pm 6.6$ |
| $\Xi_c^0 \longrightarrow \Xi^- e^+ \nu$ | $2.2 \pm 4.9$ |
| $\Xi_c^0 \longrightarrow \Xi^- (n)\pi^0 e^+ \nu$ | $6.9 \pm 4.5$ |

## 6.6 $\Xi_c^0 \longrightarrow \Xi^- \pi^+$ Mode

We have selected a candidate $\Xi_c^0 \longrightarrow \Xi^- \pi^+$ sample with the following requirements:

- The $\Xi^-$ is selected with the *standard* $\Xi^-$ cuts described in Section 6.1.
- The invariant mass of the $\Xi^-$ is within $\pm$ 10 MeV/$c^2$ of its world average of 1321.32 MeV/$c^2$ .
- The daughter pion is identified by the Čerenkov counters as being non-heavy and not a definite electron (i.e. ISTATP=0, 2, 3 or 7).
- DVNUCL is used to find the primary vertex, which is required to be in the target region. The confidence level of the primary vertex is greater than 1%.
- Charm decays are required to occur upstream of TR1, and the confidence level of the charm vertex is greater than 0.2.
- The secondary vertex isolation, ISO2 is required to be less than 0.01.

We formed the $\Xi^- \pi^+$ invariant mass distributions using only type-2 $\Xi^-$ as shown in Figure 6.15. The histogram is fitted to the Gaussian signal and the second order

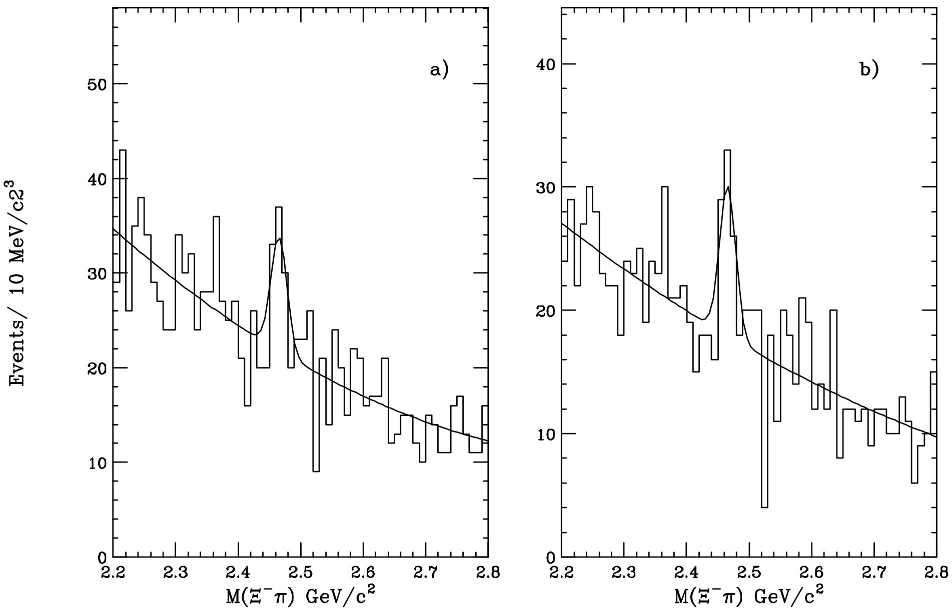


Figure 6.15: Invariant mass distributions of $\Xi^-\pi^+$ combination with the cuts described in the text at different $L/\sigma$ requirements: a) $L/\sigma > 0.25$ and b) $L/\sigma > 0.5$.

polynomial background functions using a binned likelihood method, where we fixed the width of the Gaussian to the value obtained by Monte Carlo. The fit yields the $\Xi_c^0$ mass of $2465.9 \pm 4.2$ MeV/$c^2$ and $39.6 \pm 11.8$ signal events for $L/\sigma > 0.5$.

## 6.7 Branching Ratio Measurements

We have obtained the reconstruction efficiencies for each $\Xi_c^0$ baryon semileptonic decay channels with 1 million generated Monte Carlo events. The $\Xi_c^0 \longrightarrow \Xi^-\pi^+$ reconstruction efficiency is also obtained with 1 million generated Monte Carlo events. The reconstruction efficiencies of each decay mode are summarized in Table 6.6.

The branching ratio of the $\Xi_c^0 \longrightarrow \Xi^- l^+ X$ decay relative to the $\Xi_c^0 \longrightarrow \Xi^-\pi^+$ decay is computed by using yields from the fit and the reconstruction efficiencies of

Table 6.6: Monte Carlo reconstruction efficiencies

| Decay modes | Efficiencies(%) |
|---|---|
| $\Xi_c^0 \longrightarrow \Xi^-\pi^+$ | $2.4386 \pm 0.0499$ |
| $\Xi_c^0 \longrightarrow \Xi^-\mu^+\nu$ | $0.0909 \pm 0.0031$ |
| $\Xi_c^0 \longrightarrow \Xi^-(n)\pi^0\mu^+\nu$ | $0.0423 \pm 0.0021$ |
| $\Xi_c^0 \longrightarrow \Xi^-e^+\nu$ | $0.0537 \pm 0.0024$ |
| $\Xi_c^0 \longrightarrow \Xi^-(n)\pi^0e^+\nu$ | $0.0172 \pm 0.0014$ |

the decay channels:

$$\frac{\Gamma(\Xi_c^0 \longrightarrow \Xi^- l^+ X)}{\Gamma(\Xi_c^0 \longrightarrow \Xi^-\pi^+)} = \frac{N(\Xi^- l^+ X)}{\epsilon(\Xi^- l^+ X)} \times \frac{\epsilon(\Xi^-\pi^+)}{N(\Xi^-\pi^+)} \tag{6.4}$$

The branching ratios for the electron mode and the muon mode are computed separately, then two results are combined with weighted averages. The results are as follows:

$$\frac{\Gamma(\Xi_c^0 \longrightarrow \Xi^-\mu^+ X)}{\Gamma(\Xi_c^0 \longrightarrow \Xi^-\pi^+)} = 4.0 \pm 1.9$$

$$\frac{\Gamma(\Xi_c^0 \longrightarrow \Xi^- e^+ X)}{\Gamma(\Xi_c^0 \longrightarrow \Xi^-\pi^+)} = 2.7 \pm 2.1$$

$$\frac{\Gamma(\Xi_c^0 \longrightarrow \Xi^- l^+ X)}{\Gamma(\Xi_c^0 \longrightarrow \Xi^-\pi^+)} = 3.5 \pm 1.5$$

# Chapter 7

# Systematic Error Studies

In this chapter we now present several studies designed to check a possible systematic bias in our measurement of the relative branching ratio $\frac{\Gamma(\Xi_c^0 \to \Xi^- l^+ X)}{\Gamma(\Xi_c^0 \to \Xi^- \pi^+)}$. Since both the signal mode and the normalization mode are topologically similar and the analysis cuts were performed in a similar method, we anticipate that many of the sources of systematic error should be canceled out or be significantly reduced.

## 7.1 The Techniques

We generally separate the estimation of error in any measurement into two types. The first type of error is the usual statistical error which can be obtained from the fit to a measured distribution. The second type of error we call the systematic error. This usually originates from uncertainties in our data modeling. We have done a careful job of determining the components of our signal and making our measurement, but there may be still some bias that we either overlooked, or can not model ( such as an undiscovered decay that influences our final sample). In practice, we can estimate the systematic error by including the known limitations in the simulation of various detectors, uncertainties in set parameters, such as the level of misidentification, and the level of mismatch between our simulated and real data samples.

We estimate the level of mismatch by considering differences in the fit parameters obtained using different variants of fitting techniques and non-statistical differences in the parameters obtained by fitting disjoint subsamples of the whole data set. The estimate is performed through a combination of the following two methods, which have been used with some success in several E687 analyses [39]:

- We split the data sample into several disjoint subsamples and compare the fit parameters obtained in various splits of the data sample. In a fixed target experiment efficiency corrections (acceptance, Čerenkov particle identification, triggering) are highly momentum dependent, hence a natural split is to divide the sample on the basis of momentum. In the E687, the data collected in 1990 was taken under slightly different triggering conditions and with slightly different equipments than used in the 1991 data. We therefore split the data chronologically as well. Furthermore, we divide our data sample into statistically independent, approximately equal subsamples based on each analysis cut applied in order to assess systematic errors associated with a given cut variable because we have chosen the cut somewhat arbitrarily, based loosely on signal quality and event yield. The problem in estimating systematics by comparing split sample estimators is in deciding how much of the difference in the fit parameters is from statistical fluctuation and how much should be ascribed to systematic error. We use a method for handling this based on the S–factor technique which is used by the PDG [40] to combine data from statistically inconsistent experiments.

- One can also estimate systematic errors by varying reasonable fitting techniques for a complete data set. Fit variants include the use of parameterized as opposed to binned efficiencies, differences in the background subtraction methods, incorporation or neglect of kinematic smearing effects, etc. The problem in estimating systematics by comparing fit parameters between fit variants is to decide how to extract a meaningful systematic error from the spread of estimates obtained with the various fit variants.

### 7.1.1 Split Sample Systematics

If one considers splitting a data sample into $N$ disjoint sets, the standard test for statistical consistency is to construct a confidence level for the hypothesis that $N$ measurements can be fit by a single (weighted average) fit parameter. For $N$ independent samples, the confidence level would be constructed from $\chi^2$ with $N-1$ degrees of freedom of the form:

$$\chi^2 = \sum_i^N \frac{(x_i - < x >)^2}{\sigma_i^2}$$

where

$$< x > = \frac{\sum_i x_i/\sigma_i^2}{\sum_i 1/\sigma_i^2}.$$

We can use this $\chi^2$ to extract an estimate of the systematic error in analogy with the S–factor method. If the dispersion between returned estimators is purely statistical, one would expect $\chi^2 \simeq N-1$. However if $\chi^2 > N-1$, one might attribute the inconsistency to an underestimation of the true split sample errors which reflects an unknown systematic problem. If all subsample errors are scaled up by $\sigma_i\sqrt{\chi^2/(N-1)}$, the new $\chi^2$ per degree of freedom will automatically satisfy our test. In addition, the statistical error for the weighted average of the subsample estimates

$$\overline{\sigma} = \frac{1}{\sqrt{\sum_i^N 1/\sigma_i^2}}$$

will be increased by the same factor and become a "scaled error" ($\tilde{\sigma}$) of

$$\tilde{\sigma} = \overline{\sigma}\sqrt{\chi^2/(N-1)} = \sqrt{\frac{< x^2 > - < x >^2}{N-1}}$$

where we use the weighted averaging brackets $<>$. The scaled error is compared with the statistical error on the full data sample $\sigma$. If the scaled error $\tilde{\sigma}$ is greater than $\sigma$ then the systematic error is given by

$$\sigma_{\mathrm{SYS}} = \sqrt{\tilde{\sigma}^2 - \sigma^2}.$$

If $\tilde{\sigma} < \sigma$ then there is no systematic error associated with the variable used in splitting the full data set into $N$ subsamples.

This systematic error is used to separate true indications of systematic problems from normal statistical fluctuations. Furthermore the error $\tilde{\sigma}$ and $\sigma_{\mathrm{SYS}}$ will tend to be independent of the number of subsamples $N$ and thus essentially independent of the number of systematic sources considered.

### 7.1.2 Fit Variant Systematics

We shall now discuss a method on evaluating systematic errors associated with the fitting procedure in the same manner of the split sample systematics. The fit variant systematic is different from the split sample systematic in the following respects:

- We assume that the fit variants are all *a priori* likely. It means that we should use a straight average, $< x >= \sum_i^N x_i/N$, rather than the weighted average.

- Furthermore, we are not making a combined average of the fit variants where each variant is adding independent information. As a result we should remove a factor of $1/\sqrt{N}$ in the $\tilde{\sigma}$ expression which reflects the fact that we average the $N$ split samples to obtain an error on the combined sample. We assess the actual root mean square (rms) spread in a set of estimators rather than the spread on the mean.

- Lastly there is no need to subtract the statistical variance from $\tilde{\sigma}$, since the fit variations should essentially have fully correlated statistical errors.

Making these modifications we have

$$\sigma_{\text{sys}} = \sqrt{\frac{\sum_i^N x_i^2 - N < x >^2}{N-1}}$$

which is the expression for the sample standard deviation and differs from the population standard deviation by $N \to N-1$. The sample standard deviation should be roughly independent of the number of events in the sample as long as reasonable fit variants actually follow a normal distribution.

Lastly we believe that fit variant systematic, which reflects uncertainty in the fitting technique used, is independent of the split sample systematic, which indicates uncertainty in the model used to represent the data as gauged by the degree of internal inconsistency of the model and the data. For this reason, we add the fit variant systematic error to the split sample systematic error in quadrature to obtain the combined systematic error.

## 7.2 Systematics in the $\Gamma(\Xi_c^0 \to \Xi^- l^+ X)/\Gamma(\Xi_c^0 \to \Xi^- \pi^+)$

We estimate the systematics in the measurement of the branching ratio measurement of $\Gamma(\Xi_c^0 \to \Xi^- l^+ X)/\Gamma(\Xi_c^0 \to \Xi^- \pi^+)$ using the techniques discussed in the preceding section.

We have performed several studies to check any systematic bias in the branching ratio measurements. In order to check that the fitting routine is acceptable and the errors returned by the fitting routine are accurate, we take a fit histogram and fluctuate the population of each bin for all bins with Poisson function. We then fit this new histogram as if it were data. This process of Poisson fluctuating the bin population of our original fit histogram is repeated 10,000 times. The results of Poisson fluctuated fits are shown in Figure 7.1 for the muon mode and in Figure 7.2 for the electron mode. The fluctuated histogram is fitted to the Gaussian signal. The fit results for each mode are listed in Table 7.1.

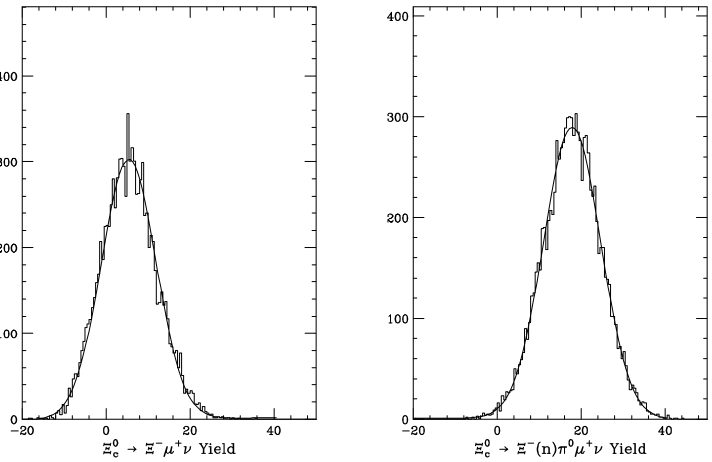


Figure 7.1: The yield returned by the fitting routine for 10,000 Poisson fluctuated histograms for the decay of the $\Xi_c^0 \longrightarrow \Xi^- \mu^+ X$.

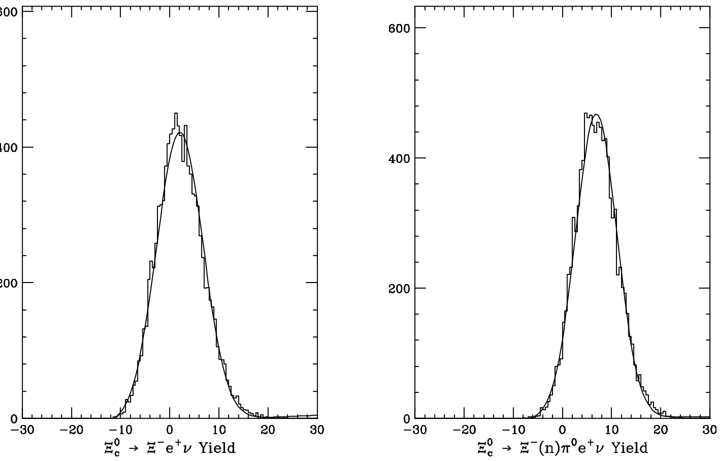


Figure 7.2: The yield returned by the fitting routine for 10,000 Poisson fluctuated histograms for the decay of the $\Xi_c^0 \longrightarrow \Xi^- e^+ X$.

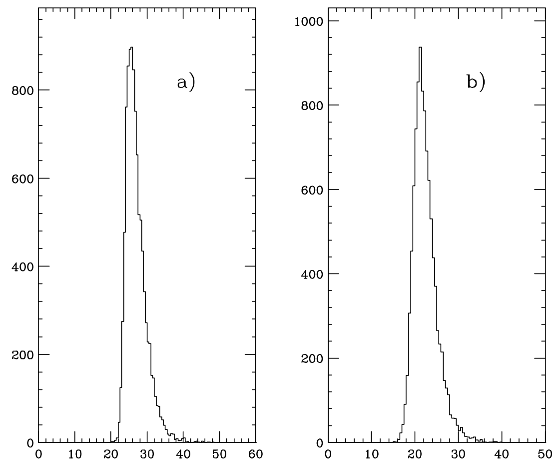


Figure 7.3: The negative log likelihood function returned by the fitting routine for 10,000 Poisson fluctuated histograms: a) for the muon mode, and b) for the electron mode.

The results from the fluctuated spread have the same mean values and errors returned by the data fit. This means that the errors returned by the fit are reasonable. The values of the negative log likelihood function for the simulated data are shown in Figure 7.3 for both the muon and electron modes. The values of the negative log likelihood function returned by the fit are 30.3 for the muon mode and 24.4 for the electron mode. Those values are compared with the distributions. It turns out that our fits to the data are satisfactory.

To study any systematic errors associated with the given cut variables [39], we have divided the sample into four independent subsamples, approximately two equal sizes of subsamples for each mode (muon and electron). The cut criteria used in this study are listed in Table 7.2. For each analysis cut, we calculated the branching ratios for the two independent samples in each mode and combined them using a weighted average. The proper time is calculated by using the visible momentum, the charm decay length, and the given $\Xi_c^0$ mass of 2470.3 MeV/$c^2$ .

It turns out that the variation of the branching ratio measurement with the split

Table 7.1: Comparison of fits and fluctuated histogram trials.

| Decay modes | Fit Yield | Fluctuated Histograms |
|---|---|---|
| $\Xi_c^0 \longrightarrow \Xi^- \mu^+ \nu$ | $5.6 \pm 6.4$ | $5.4 \pm 6.5$ |
| $\Xi_c^0 \longrightarrow \Xi^- (n) \pi^0 \mu^+ \nu$ | $18.7 \pm 6.6$ | $17.9 \pm 6.8$ |
| $\Xi_c^0 \longrightarrow \Xi^- e^+ \nu$ | $2.2 \pm 4.9$ | $2.1 \pm 4.8$ |
| $\Xi_c^0 \longrightarrow \Xi^- (n) \pi^0 e^+ \nu$ | $6.9 \pm 4.5$ | $6.9 \pm 4.2$ |

Table 7.2: Split sample criteria.

| Variable | Cut value |
|---|---|
| Run period | 1990; 1991 |
| CLD | CLD $> 0.45$; CLD $< 0.45$ |
| ISO1 | ISO1 $> 0.20$; ISO1 $< 0.20$ |
| ISO2 | ISO2 $= 0$; ISO2 $\neq 0$ |
| $L/\sigma$ | $L/\sigma > 1.5$; $L/\sigma < 1.5$ |
| $p(\Xi l)$ | $p(\Xi l) < 55.0$ GeV/$c$ ; $p(\Xi l) > 55.0$ GeV/$c$ |
| $p(l)$ | $p(l) < 20.0$ GeV/$c$ ; $p(l) > 20.0$ GeV/$c$ |
| $M(\Xi^-)$ | $M(\Xi^-) > 1.321$ GeV/$c^2$ ; $M(\Xi^-) < 1.321$ GeV/$c^2$ |
| Proper Time | $\tau(\Xi_c^0) > 0.2$ ps; $\tau(\Xi_c^0) < 0.2$ ps |

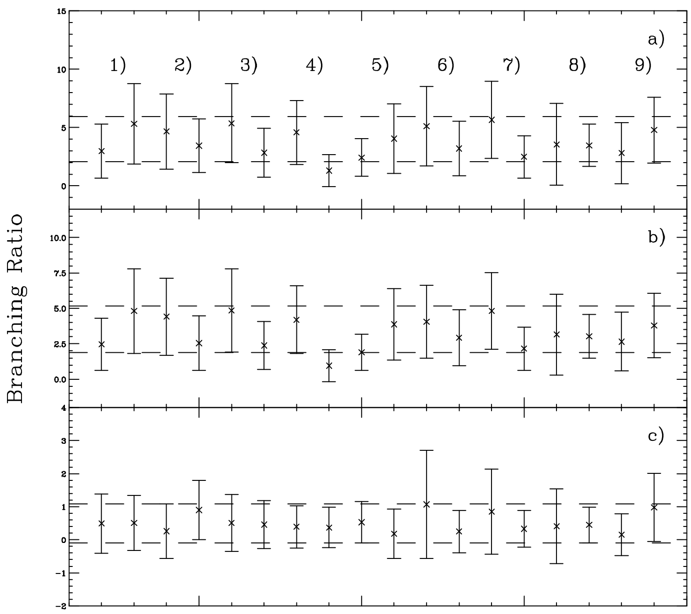


Figure 7.4: Branching ratios for the various split samples: a) for the $\Xi_c^0 \rightarrow \Xi^-\mu^+X$ decay, b) for the $\Xi_c^0 \rightarrow \Xi^-(n)\pi^0\mu^+\nu$ decay, and c) for $\Xi_c^0 \rightarrow \Xi^-\mu^+\nu$ decay; 1) for run periods, 2) for CLD, 3) for ISO1, 4) for ISO2, 5) for the $L/\sigma$, 6) for the $p(\Xi\mu)$, 7) for the $p(\mu)$, 8) for the $M(\Xi^-)$, and 9) for the proper time.

sample is comparable to the statistical error. The branching ratio of each subsample is plotted in Figure 7.4 for the muon mode, in Figure 7.5 for the electron mode, and in Figure 7.6 for the muon and electron combined by using the weighted average.

To investigate possible systematic errors associated with fit variants [39], we have studied the binning effects of the $\Xi l$ invariant mass histograms with 6, 12, and 24 bins. We also have checked the mean value variation in the split sample studies. We conservatively estimate the total systematic error associated with the fit variants to be 16.4 %.

Since we fixed the amount of the backgrounds from hadrons misidentified as leptons when we performed the fit to $\Xi l$, we need to check the systematic bias from our estimate for the level of misidentification background.

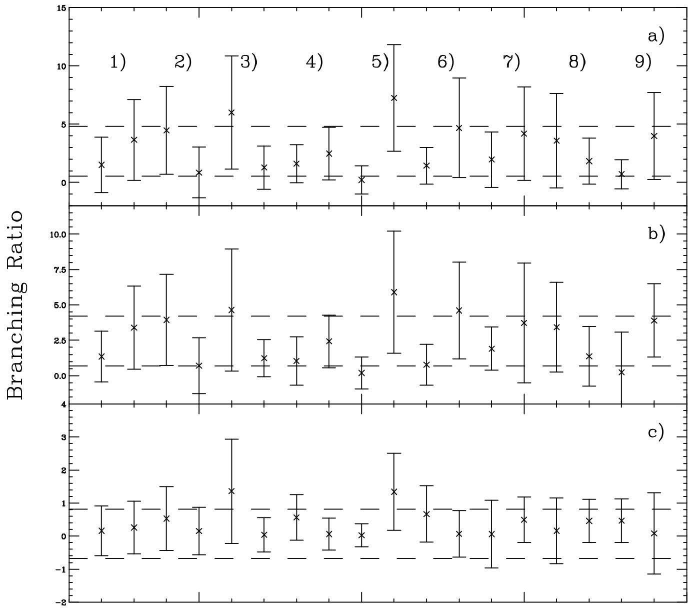


Figure 7.5: Branching ratios for the various split samples: a) for the $\Xi_c^0 \rightarrow \Xi^- e^+ X$ decay, b) for the $\Xi_c^0 \rightarrow \Xi^-(n)\pi^0 e^+\nu$ decay, and c) for $\Xi_c^0 \rightarrow \Xi^- e^+\nu$ decay; 1) for run periods, 2) for CLD, 3) for ISO1, 4) for ISO2, 5) for the $L/\sigma$, 6) for the $p(\Xi e)$, 7) for the $p(e)$, 8) for the $M(\Xi^-)$, and 9) for the proper time.

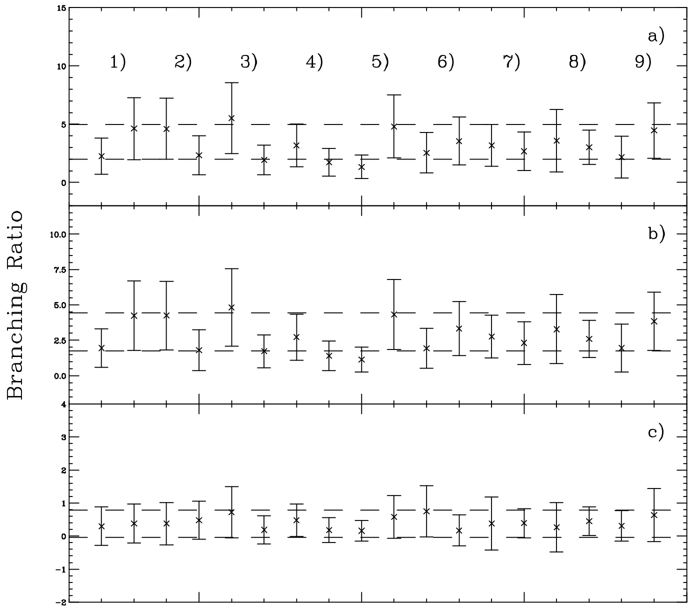


Figure 7.6: Branching ratios for the various split samples: a) for the $\Xi_c^0 \to \Xi^- l^+ X$ decay, b) for the $\Xi_c^0 \to \Xi^-(n)\pi^0 l^+ \nu$ decay, and c) for $\Xi_c^0 \to \Xi^- l^+ \nu$ decay; 1) for run periods, 2) for CLD, 3) for ISO1, 4) for ISO2, 5) for the $L/\sigma$, 6) for the $p(\Xi l)$, 7) for the $p(l)$, 8) for the $M(\Xi^-)$, and 9) for the proper time.

Table 7.3: The comparison of fits and Poisson fluctuated trials of the number of the right sign random combination background.

| Decay Modes | Fit Yield | Fluctuated Histograms |
|---|---|---|
| $\Xi_c^0 \longrightarrow \Xi^- \mu^+ \nu$ | $5.6 \pm 6.4$ | $5.6 \pm 0.8$ (13.5 %) |
| $\Xi_c^0 \longrightarrow \Xi^- (n)\pi^0 \mu^+ \nu$ | $18.7 \pm 6.6$ | $18.7 \pm 0.7$ ( 4.0 %) |
| $\Xi_c^0 \longrightarrow \Xi^- e^+ \nu$ | $2.2 \pm 4.9$ | $2.2 \pm 0.4$ (16.9 %) |
| $\Xi_c^0 \longrightarrow \Xi^- (n)\pi^0 e^+ \nu$ | $6.9 \pm 4.5$ | $7.0 \pm 0.3$ ( 4.3 %) |

The systematic uncertainty from the backgrounds estimated by lepton misidentification is studied with increasing or decreasing the lepton misidentification probability by 1 $\sigma$. The systematic uncertainty on the branching ratio is 5.2 % from the lepton misidentification probabilities. We have also varied by 1 $\sigma$ of the number of background events in each histogram bin, and estimated that this contribution is 5.5 %. In order to check this contribution is acceptable, we again constructed the fit histogram with the number of the right sign random combination background with a level that can Poisson fluctuate. The results from the Gaussian fits to fluctuated histograms are listed in Table 7.3. The results from the fluctuated histograms have the same mean values returned by the fit. This means that it is reasonable to fix the background level when we construct the fit histogram. From the spread of the fluctuated histogram, we estimated that this contribution is 5.2 % which is comparable to the value estimated by the previous method. Combining the two errors added in quadrature, we conservatively estimate the systematic uncertainties associated with lepton misidentification to be 7.5 %.

All the sources of systematic errors for the branching ratio measurements are in Table 7.4. Combining all the sources of systematic errors in quadrature, we conservatively estimate a total systematic uncertainty to be 18.0 %.

Table 7.4: Systematic uncertainties on the branching ratio measurements for $\Xi_c^0$ semileptonic decays.

| Systematic Uncertainties | | | |
|---|---|---|---|
| Source | Muon mode | Electron Mode | Combined ($\mu$ + e) |
| Fit variants | $\pm 14.7\%$ | $\pm 30.5\%$ | $\pm 16.4\%$ |
| Split samples | $\pm 0.0\%$ | $\pm 0.0\%$ | $\pm 0.0\%$ |
| Misidentification level | $\pm 6.4\%$ | $\pm 9.9\%$ | $\pm 7.5\%$ |
| Total systematic error | $\pm 16.0\%$ | $\pm 32.1\%$ | $\pm 18.0\%$ |

Our final results for the branching ratio measurements for the $\Xi_c^0$ semileptonic decay are :

$$\frac{\Gamma(\Xi_c^0 \longrightarrow \Xi^- \mu^+ X)}{\Gamma(\Xi_c^0 \longrightarrow \Xi^- \pi^+)} = 4.0 \pm 1.9(stat.) \pm 0.6(syst.)$$

$$\frac{\Gamma(\Xi_c^0 \longrightarrow \Xi^- e^+ X)}{\Gamma(\Xi_c^0 \longrightarrow \Xi^- \pi^+)} = 2.7 \pm 2.1(stat.) \pm 0.9(syst.)$$

$$\frac{\Gamma(\Xi_c^0 \longrightarrow \Xi^- l^+ X)}{\Gamma(\Xi_c^0 \longrightarrow \Xi^- \pi^+)} = 3.5 \pm 1.5(stat.) \pm 0.6(syst.)$$

# Chapter 8

# Results and Discussion

We have measured the branching ratios of the $\Xi_c^0$ semileptonic decays relative to $\Xi_c^0 \longrightarrow \Xi^- \pi^+$. We have reconstructed both the electron and muon modes of the $\Xi_c^0 \longrightarrow \Xi^- l^+ X$ semileptonic decays. The results are as follows:

$$\frac{\Gamma(\Xi_c^0 \longrightarrow \Xi^- \mu^+ X)}{\Gamma(\Xi_c^0 \longrightarrow \Xi^- \pi^+)} = 4.0 \pm 1.9(stat.) \pm 0.6(syst.)$$

$$\frac{\Gamma(\Xi_c^0 \longrightarrow \Xi^- e^+ X)}{\Gamma(\Xi_c^0 \longrightarrow \Xi^- \pi^+)} = 2.7 \pm 2.1(stat.) \pm 0.9(syst.)$$

$$\frac{\Gamma(\Xi_c^0 \longrightarrow \Xi^- l^+ X)}{\Gamma(\Xi_c^0 \longrightarrow \Xi^- \pi^+)} = 3.5 \pm 1.5(stat.) \pm 0.6(syst.)$$

Our results are consistent within errors with the values, $\frac{\Gamma(\Xi_c^0 \longrightarrow \Xi^- l^+ X)}{\Gamma(\Xi_c^0 \longrightarrow \Xi^- \pi^+)} = 0.96 \pm 0.43 \pm 0.18$, reported by the ARGUS collaboration [30], and $\frac{\Gamma(\Xi_c^0 \longrightarrow \Xi^- e^+ \nu)}{\Gamma(\Xi_c^0 \longrightarrow \Xi^- \pi^+)} = 3.1 \pm 1.0^{+0.3}_{-0.5}$, reported by the CLEO collaboration [31].

Our results indicate that the $\Xi_c^0$ decays semileptonically to modes other than $\Xi^- l^+ \nu$, such as $\Xi^-(n)\pi^0 l^+ \nu$. The large statistical error hampers the detailed study of exclusive $\Xi_c^0$ semileptonic decay modes further.

Fermilab E831(FOCUS) is an upgrade of E687 [44] and the collaboration is now in the middle of data reconstruction. A factor of 30 increases in statistics for both muonic and electronic channels have been predicted for semileptonic charmed meson decays. With the larger statistics we may reconstruct the $\Xi_c^0$ momentum by using two vertex positions, the momenta of the charged daughters, and a given the $\Xi_c^0$ mass. With this technique, we can study hadronic structure as well as attempt to tag the semileptonic decay modes via the decay $\Xi_c^{*+} \longrightarrow \Xi_c^0\pi^+$ [41, 42]. Many of the details needed to complete analyses using the FOCUS data will be the same as those used in E687 due to the similar nature of the two experiments. The results of our analysis then, will prove valuable as a reference for the analysis of the semileptonic $\Xi_c^0$ decays for the FOCUS data.

# Bibliography


[1] Particle Data Group, *The Euro. Phys. Jour.* **C3,** 486(1998)

[2] L. M. Jones and H. W. Wyld, *Phys. Rev.* **D17,** 759(1978)

[3] R. K. Ellis and P. Nason, *Nucl. Phys.* **B312,** 551(1989);
J. Smith and W. L. van Neerven, *Nucl. Phys.* **B374,** 36(1992);
S. Frixone, M. Mangano, P. Nason, and G. Ridolfi, *Nucl. Phys.* **B412,** 225(1992)

[4] N. Cabibbo, *Phys. Rev. Lett.* **10,** 531(1963);
M. Kobayashi and T. Maskawa, *Prog. Theor. Phys.* **49,** 652(1979)

[5] M. Gell-Mann, *Phys. Lett.* **8,** 214(1964)

[6] G. Zweig, *CERN TH-report,* TH-401(1964)

[7] D.J.Bjorken and S.L. Glashow, *Phys. Lett.* **11,** 255(1964)

[8] S.L. Glashow, J. Iliopoulos, and L. Maiani, *Phys. Rev.* **D2,** 1285(1970)

[9] M.K. Gaillard, B.W. Lee, and J. Rosner, *Rev. Mod. Phys.* **47,** 277(1972)

[10] J.J. Aubert, et al., *Phys. Rev. Lett.* **33,** 1404(1974)

[11] J.E. Augustin, et al., *Phys. Rev. Lett.* **33,** 1406(1974)

[12] S.W. Herb, et al., *Phys. rev. Lett.* **39,** 252(1977)

[13] F. Abe, et al., *Phys. Rev. Lett.* **74,** 2626(1995)

[14] S. Abachi, et al., *Phys. Rev. Lett.* **74,** 2632(1995)

[15] C.E. Carlson and P.G.O. Freud, *Phys. Lett.* **B39,** 349(1972)

[16] J.J. Sakurai, *Ann. Rev. Nucl. Part. Sci.* **11,** 1(1960)

[17] L.M.Jones and H.W. Wyld, *Phys. Rev.* **D17,** 759(1978)

[18] Particle Data Group, *The Euro. Phys. Jour.* **C3,** 24(1998)

[19] Particle Data Group, *The Euro. Phys. Jour.* **C3,** 24(1998)

[20] Particle Data Group, *The Euro. Phys. Jour.* **C3,** 57(1998)

[21] Particle Data Group, *The Euro. Phys. Jour.* **C3,** 58(1998)

[22] S. Fleck and J.M. Richard, *Particle World* **1,** 67(1990)

[23] J.M. Richard and P. Taxil, *Phys. Lett.* **B128,** 453(1983)

[24] S. Capstick and N. Isgur, *Phys. Rev.* **D34,** 2809(1986)

[25] W. Kwong, J.L. Rosner, and C. Quigg, *Annu. Rev. Nucl. Part. Sci.* **37,** 325(1987)

[26] G. Brandenbug, et al., *CLEO conf-93-13* (1996)
P.Avery, et al., *Phys. Rev. Lett.* **75,** 4364(1995)
L. Gibbons, et al., *Phys. Rev. Lett.* **77,** 810(1996)

[27] P. L. Frabetti, et al., *Phys. Lett.* **B426,** 403(1998)

[28] S. Fleck and J. M. Richard, *Particle World* **1,** 67(1990)

[29] M.B. Voloshin and M.A. Shifman, *Sov. Phys. JETP* **64(4),** 698(1986);
B. Guberina, R. Rückl, and J. Trampetić, *Z. Pjys.* **C33,** 297(1986)

[30] H. Albrecht, et al., *Phys. Lett.* **B303,** 268(1993)

[31] J.P.Alexander, et al.,, *Phys. Rev. Lett.* **74,** 3113(1995)

[32] M. S. Nehring, *Ph.D. Thesis, University of Colorado at Boulder* 1995(Unpublished)

[33] W. E. Johns, *Ph.D. Thesis, University of Colorado at Boulder* 1995(Unpublished)

[34] L. Cinquini, *Ph.D. Thesis, University of Colorado at Boulder* 1996(Unpublished)

[35] C. J. Dallapiccola, *Ph.D. Thesis, University of Colorado at Boulder* 1993(Unpublished)

[36] P. L. Frabetti, et al., *Nucl. Instru. & Meth.* **A320,** 519(1992)

[37] P. L. Frabetti, et al., *Nucl. Instru. & Meth.* **A538,** 519(1992)

[38] P. L. Frabetti, et al., *Nucl. Instru. & Meth.* **A329,** 62(1993)

[39] P. L. Frabetti, et al., *Techniques for the Resonance Analysis of Three Body D Meson Decays,* to be submitted to *Nucl. Instru. & Meth.*

[40] Particle Data Group, *Phys. Rev.* **D54,** 1(1996)

[41] L. Gibbons, et al., *Phys. Rev. Lett.* **77,** 810(1996)

[42] P. L. Frabetti, et al., *Phys. Lett.* **B426,** 403(1998)

[43] P. L. Frabetti, et al., *E831 internal Memo*

[44] P. L. Frabetti, et al., *Nucl. Instru. & Meth.* **A320,** 519(1992)

[45] T. Sj"ostrand, *Comp. Phys. Commun. 82,* 74(1994)

# Appendix A

# The E687 Collaboration

P. L. Frabetti,[1] H. W. K. Cheung,[2] J. P. Cumalat,[2] C. Dallapiccola,[2] J. F. Ginkel,[2] S. V. Greene,[2] W. E. Johns,[2] M. S. Nehring,[2] E. Vaandering,[2] J. N. Butler,[3] S. Cihangir,[3] I. Gaines,[3] P. H. Garbincius,[3] L. Garren,[3] S. A. Gourlay,[3] D. J. Harding,[3] P. Kasper,[3] A. Kreymer,[3] P. Lebrun,[3] S. Shukla,[3] M. Vittone,[6] S. Bianco,[4] F. L. Fabbri,[4] S. Sarwar,[4] A. Zallo,[4] R. Culbertson,[5] R. W. Gardner,[5] R. Greene,[5] J. Wiss,[5] G. Alimonti,[6] G. Bellini,[6] B. Caccianiga,[6] L. Cinquini,[6] M. Di Corato,[6] M. Giammarchi,[6] P. Inzani,[6] F. Leveraro,[6] S. Malvezzi,[6] D. Menasce,[6] E. Meroni,[6] L. Moroni,[6] D. Pedrini,[6] L. Perasso,[6] A. Sala,[6] S. Sala,[6] D. Torretta,[6] D. Buchholz,[7] D. Claes,[7] B. Gobbi,[7] B. O'Reilly,[7] J. M. Bishop,[8] N. M. Cason,[8] C. J. Kennedy,[8] G. N. Kim,[8] T. F. Lin,[8] D. L. Pušeljić,[8] R. C. Ruchti,[8] W. D. Shephard,[8] J. A. Swiatek,[8] Z. Y. Wu,[8] V. Arena,[9] G. Boca,[9] C. Castoldi,[9] G. Gianini,[9] S. P. Ratti,[9] C. Riccardi,[9] P. Vitulo,[9] A. Lopez,[10] G. P. Grim,[11] V. S. Paolone,[11] P. M. Yager,[11] J. R. Wilson,[12] P. D. Sheldon,[13] F. Davenport,[14] J. F. Filaseta,[15] G. R. Blackett,[16] M. Pisharody,[16] T. Handler,[16] B. G. Cheon,[17] **Y. S. Chung**,[17] J. S. Kang,[17] K. Y. Kim,[17] K. B. Lee,[17] S. S. Myung.[17]

(1) *Dip. di Fisica dell'Università and INFN - Bologna, I-40126 Bologna, Italy*

(2) *University of Colorado, Boulder, CO 80309*

(3) *Fermilab, Batavia, IL 60510*

(4) *Laboratori Nazionali di Frascati dell'INFN, I-00044 Frascati, Italy*
(5) *University of Illinois at Urbana-Champaign, Urbana, IL 61801*
(6) *Dip. di Fisica dell'Università and INFN - Milano, I-20133 Milano, Italy*
(7) *Northwestern University, Evanston, IL 60208*
(8) *University of Notre Dame, Notre Dame, IN 46556*
(9) *Dip. di Fisica Nucleare e Teorica dell'Università and INFN - Pavia, I-27100 Pavia, Italy*
(10) *University of Puerto Rico at Mayaguez, Puerto Rico*
(11) *University of California-Davis, Davis, CA 95616*
(12) *University of South Carolina, Columbia, SC 29208*
(13) *Vanderbilt University, Nashville, TN 37235*
(14) *University of North Carolina-Asheville, Asheville, NC 28804*
(15) *Northern Kentucky University, Highland Heights, KY 41076*
(16) *University of Tennessee, Knoxville, TN 37996*
(17) *Korea University, Seoul 136-701, Korea*